UNIVERSIDAD NACIONAL DE EDUCACIÓN A DISTANCIA

Facultad de Ciencias

MÁSTER EN FÍSICA AVANZADA

TRABAJO FIN DE MÁSTER

The Quantum Cusp Catastrophe in a Generalized Quartic Potential

Miguel Ángel Campanario Marín

septiembre, 2024

UNIVERSIDAD NACIONAL DE EDUCACIÓN A DISTANCIA
Facultad de Ciencias

Master Degree in Advanced Physics

The Quantum Cusp Catastrophe in a Generalized Quartic Potential

MASTER THESIS

Submitted for the degree of Master by:

Miguel Ángel Campanario Marín

Under the supervision of:
Dr. Francisco Pérez Bernal (UHU)

September, 2024

To my parents, for the support, great patience, and for teaching me the value of hard work (even when I wasn't always listening). This achievement is as much yours as it is mine — and no, you can't frame it.

To Ana, for her love, patience, and for believing in me even when I doubted myself. Thank you for reminding me that there's more to life than academic deadlines, and for walking with me on this journey.

TRABAJO FIN DE MÁSTER

The Quantum Cusp Catastrophe in a Generalized Quartic Potential

Miguel Ángel Campanario Marín
Huelva, septiembre 2024

Resumen

Este Trabajo de Fin de Máster estudiará la Catástrofe en Cúspide haciendo uso de un potencial cuártico generalizado, extendiendo el análisis desde sistemas clásicos a sistemas cuánticos. Para ello, el estudio comienzará con una exploración exhaustiva de la Catástrofe en Cúspide Clásica (CCC), donde estudiamos los puntos críticos del sistema, el comportamiento de bifurcaciones a medida que se varían los parámetros de control y la estructura del espacio de fases del potencial. El oscilador cuártico es un oscilador anharmónico aplicable en muchos campos de la física, ya que proporciona un buen marco para explorar fenómenos como bifurcaciones o la ruptura espontánea de la simetría.
Posteriormente, extenderemos el análisis a la Catástrofe en Cúspide Cuántica (QCC, por sus siglas en inglés) resolviendo la ecuación de Schrödinger independiente del tiempo para el oscilador cuártico. Se prestará especial atención al estudio de las Transiciones de Fase Cuántica (QPTs, por sus siglas en inglés), tanto en el estado fundamental como en los estados excitados. La investigación destaca el comportamiento de cantidades clave como la densidad de niveles de energía, la fidelidad cuántica y el índice de participación (PR, por sus siglas en inglés) como indicadores de transiciones de fase cuántica. Estas cantidades proporcionarán información sobre los cambios estructurales que ocurren en las funciones de onda y los estados propios del sistema cerca de los puntos críticos, y demostrarán cómo las transiciones de fase de estado fundamental y excitados (GSQPTs y ESQPTs, por sus siglas en inglés) pueden ser detectadas y caracterizadas. También exploraremos la estructura del espacio de fases cuántico utilizando las funciones de Husimi y Wigner. Además, el estudio contribuirá a una mejor comprensión de cómo pueden manifestarse los fenómenos críticos en sistemas cuánticos, lo cual es de gran relevancia en campos como la computación cuántica y la física de la materia condensada.

MASTER THESIS

The Quantum Cusp Catastrophe in a Generalized Quartic Potential

Miguel Ángel Campanario Marín
Huelva, September 2024

Abstract

The present Master Thesis studies the Cusp Catastrophe within the framework of a generalized quartic potential, extending the analysis from classical to quantum systems. To do this, the study begins with a thorough exploration of the Classical Cusp Catastrophe (CCC), where we investigate the critical points, the bifurcation behavior as the control parameters are varied, and the potential's phase space structure. The quartic oscillator is an anharmonic oscillator applicable in many fields of physics as it provides a simple platform to explore phenomena such as bifurcations or spontaneous symmetry breaking.
We then extend the analysis to the Quantum Cusp Catastrophe (QCC) by solving the time-independent Schrödinger equation for the quartic oscillator. A special focus is placed on studying Quantum Phase Transitions (QPTs), both in the ground and excited states. The investigation highlights the behavior of key quantities such as energy level density, quantum fidelity, and participation ratio as indicators of quantum phase transitions. These quantities provide insight into the structural changes that occur in the system's wavefunctions and eigenstates near critical points, and demonstrate how QPTs and ESQPTs can be detected and characterized. We also explore the quantum phase space structure using Husimi and Wigner functions. Additionally, the study contributes to the broader understanding of how critical phenomena in quantum systems can manifest, which is highly relevant in modern fields like quantum computing and condensed matter physics.

Agradecimientos

«Este Trabajo Fin de Máster no hubiera sido posible sin el apoyo y las oportunidades que he recibido a lo largo de este camino. En primer lugar, quiero agradecer al Servicio Público de Empleo Estatal y al Programa Investigo, que me brindaron la oportunidad de comenzar mi carrera profesional en un entorno tan enriquecedor como la Universidad de Huelva.

A toda la gente del Centro de Estudios Avanzados en Física, Matemáticas y Computación (CEAFMC), gracias por acogerme con los brazos abiertos desde el primer día. Vuestro apoyo y confianza han sido fundamentales para mi desarrollo tanto profesional como académico. Mención especial a Curro, quien no solo me ofreció la oportunidad de formar parte del equipo, sino que también, junto con el CEAFMC, me brindó la oportunidad de continuar mis estudios con el Máster en Física Avanzada de la UNED. Gracias por creer en mí y por brindarme la posibilidad de seguir aprendiendo y creciendo en este campo.

Finalmente, agradezco a todos aquellos que, de una manera u otra, han formado parte de este recorrido. Este logro es un reflejo del esfuerzo compartido y del apoyo incondicional que he recibido.»

Miguel Ángel Campanario Marín
Huelva, 2024

Notation and Acronyms

NOTATION

In this document, several specific symbols and terms are used to describe mathematical and physical concepts efficiently.

a_1, a_2, a_3	:	Parameters controlling the shape of the classical quartic potential.
B_1, B_2, B_3	:	Parameters controlling the shape of the quantum quartic potential.
$\mathcal{H}$	:	Hessian matrix.
$\mathbf{H}(x, P)$	:	Classical Hamiltonian.
$H(q, p)$	:	Classical Hamiltonian using dimensionless coordinate and momentum.
$\hat{H}$	:	Quantum Hamiltonian operator of the system.
$\hat{\mathcal{H}}$	:	Dimensionless quantum Hamiltonian operator.
E	:	Energy of the system (dimensionless).
$V(X)$	:	Potential function.
f_M	:	Morse function.
f_{NM}	:	Non-Morse function.
λ_0	:	Natural length unit of the quartic oscillator.
λ_0'	:	Natural length unit of the harmonic oscillator.
ξ	:	Scaling parameter, usually representing natural length scales.
K	:	Classical limit parameter (dimensionless).
$\nu(E)$	:	Level density at energy E.
$\rho_s(E)$	:	Numerical level density at energy E.
$\mathcal{F}$	:	Quantum Fidelity.
$\mathcal{S}$	:	Quantum Fidelity Susceptibility.
H_F	:	Husimi Function.
W_F	:	Wigner Function.

LIST OF ACRONYMS

The following is an *alphabetically ordered* list of acronyms used throughout the text.

CCC	:	Classic Cusp Catastrophe
ESQPT	:	Excited State Quantum Phase Transition
HF	:	Husimi Function
HO	:	Harmonic Oscillator
IPR	:	Inverse Participation Ratio
QCP	:	Quantum Critical Point
QCC	:	Quantum Cusp Catastrophe
QF	:	Quantum Fidelity
QFI	:	Quantum Fisher Information
QFS	:	Quantum Fidelity Susceptibility
QPT	:	Quantum Phase Transition
WF	:	Wigner Function

Contents

Resumen v

Abstract vii

Agradecimientos ix

Notación y acrónimos xi

List of Figures xv

List of Tables xix

Listings xxi

1. Introduction 1
- 1.1. Objectives . . . 2
- 1.2. Thesis Structure . . . 3

2. The Quartic Potential and the Cusp Catastrophe 5
- 2.1. The Quartic Oscillator . . . 5
- 2.2. Catastrophe Theory . . . 11
- 2.3. Cusp Catastrophe . . . 17
- 2.4. Phase Space . . . 18

3. Quantum Quartic Potential and the Quantum Cusp 21
- 3.1. The Quantum Quartic Oscillator . . . 21
- 3.2. Convergence Analysis . . . 23
- 3.3. Quantum Potential . . . 25
- 3.4. Quantum Phase Space . . . 27
- 3.5. Quantum Cusp . . . 32

4. Ground and Excited State Quantum Phase Transitions 35
- 4.1. Ground State Quantum Phase Transitions . . . 36
- 4.2. Excited State Quantum Phase Transitions . . . 45

5. Conclusions 53

Bibliography 55

A. Non-dimensionalization of the Classical Quartic Hamiltonian 61

B. Excited Level Density for Classical Quartic Oscillator 63

C. Second Quantization Transformation **65**

D. Methodology **69**
D.1. Convergence 69
D.2. Wave Function Calculation 70

E. Comparison with other studies **71**
E.1. Results for Pure Quartic Oscillator 71

F. Codes **75**
F.1. Hamiltonian 75
F.2. Convergence 76
F.3. Wave Functions 78

List of Figures

2.1. Summary of the configuration of the three critical points in the cubic case. . . 9

2.2. Phase diagram of the quartic potential plus quadratic and linear terms. This summarizes the configuration of the three critical points in the cusp catastrophe. 11

2.3. (a) The surface formed by the x values that satisfy $\frac{dV(x)}{dx} = 0$ as a function of parameters a and b. The inflection points (satisfying $\frac{d^2V(x)}{dx^2} = 0$) are drawn in red. (b) The same surface from a top view, showing that the projection of the inflection points onto the a-b plane matches the equation (2.29) that determines the stability of critical points, as shown in Figure 2.2. 17

2.4. Constant energy contours of the phase space for the classical Hamiltonian corresponding to the Cusp Catastrophe for different values of the control parameters a and b. (a) Pure quartic potential $V(x) = x^4$, $a = 0$ and $b = 0$; (b) Symmetric double well potential $V(x) = x^4 - 5x^2$ with $a = -5$ and $b = 0$; and (c) Asymmetric double well potential $V(x) = x^4 - 5x^2 + x$ with $a = -5$ and $b = 1$. Black contour indicates the level in which $E = 0$. 19

3.1. (a) Eigenvalues E_0, E_1, and E_2 as a function of the basis size N calculated for the pure quartic potential ($B_1 = B_2 = B_3 = 0$) with parameters $K = 1$, and $\xi = \sqrt{2}$. (b) Logarithmic scale of the absolute differences between successive eigenvalues for E_0, E_1, and E_2 as a function of the basis size N. 24

3.2. Representation of the pure quartic potential $V(X) = X^4$ and the probability density functions of the first twelve eigenstates. The calculations were performed using $B_1 = 0$, $B_2 = 0$, $K = 40$, $\xi = \sqrt{2}$ and a basis dimension $N = 355$, with a convergence tolerance of 10^{-6} for the eigenvalues. 25

3.3. Representation of the symmetric double-well potential $V(X) = X^4 - 5X^2$ (shown in green) and the probability functions of the first twelve eigenstates (shown in blue). The figure illustrates the (quasi)degeneration of states below the potential barrier as well as the increase in level density at $E = 0$. Calculations were performed using $B_1 = 0$, $B_2 = -5$, $K = 40$, $\xi = \sqrt{2}$ and a basis dimension $N = 355$, with a convergence tolerance of 10^{-6} for the eigenvalues. 26

3.4. Visual representation of the asymmetric double-well potential $V(X) = X^4 - 5X^2 + X$ showing the first twelve eigenstate probability densities in blue. Calculations were performed using $B_1 = 1$, $B_2 = -5$, $K = 40$, $\xi = \sqrt{2}$ and a basis dimension $N = 415$, with a convergence tolerance of 10^{-6} for the eigenvalues. 27

3.5. Wigner and Husimi Functions for the ground state ($n = 0$) of the quartic oscillator for different potential configurations. Calculations were performed using $K = 1$, $\xi = 1$ and the correspondent values of B_1 and B_2 for each potential. 29

3.6. Wigner and Husimi Functions for the ground state ($n = 3$) of the quartic oscillator for different potential configurations. Calculations were performed using $K = 1$, $\xi = 1$ and the correspondent values of B_1 and B_2 for each potential. 30

3.7. Wigner and Husimi Functions for the ground state ($n = 15$) of the quartic oscillator for different potential configurations. Calculations were performed using $K = 1$, $\xi = 1$ and the correspondent values of B_1 and B_2 for each potential. 31

3.8. Phase diagram and potential shapes for the quantum Hamiltonian in the linear case of the cusp catastrophe. The curve delineates the transition between different potential configurations. Points (a) to (i) illustrate the potential forms at various parameter values B_1 and B_2, showing transitions from a single minimum to symmetric and asymmetric double minima. The purple and orange trajectories indicate the paths followed in the parameter space to explore first and second-order quantum phase transitions, respectively. 33

4.1. Energy level for a quartic potential Hamiltonian with a negative quadratic term ($B_2 = -1$) for different values of B_1 from -1 to 1. The calculations were performed using $K = 10000$, $\xi = \sqrt{2}$, and a basis dimension $N = 2000$. 40

4.2. Left: Derivative of the ground state energy with respect to the control parameter B_1. Right: Expected value of the position $\langle X \rangle$ as a function of B_1. Both with $B_2 = -1$ and using $K = 10000$, $\xi = \sqrt{2}$, with a basis dimension $N = 2000$.. . . . 41

4.3. Variation of QF ($\mathcal{F}$) and QFS ($\mathcal{S}$) of the ground state with respect to B_1 with $B_2 = -1$ and $K = 10000$, $\xi = \sqrt{2}$, with a basis dimension $N = 2000$, and a perturbation $\delta B_2 = 0.001$. 41

4.4. Energy spectrum of Hamiltonian (3.18) as a function of the control parameter B_2 with $B_1 = 0$. The calculations were performed using $K = 6000$, $\xi = \sqrt{2}$, and a basis dimension $N = 2000$.This plot illustrates the transformation of the potential from a symmetric double well to a single minimum potential, highlighting the energy behaviors of the ground and excited states across the transition from $B_2 < 0$ to $B_2 \geq 0$. 42

4.5. Left: First derivative of the Hamiltonian evaluated at the critical point X_c with respect to B_2 as a function of B_2, showing the change in slope at $B_2 = 0$. Right: Second derivative of the Hamiltonian (evaluated at the critical point X_c) with respect to B_2, highlighting the discontinuity at $B_2 = 0$. These derivatives are calculated both analytically and numerically using $K = 6000$, $\xi = \sqrt{2}$ with a basis dimension $N = 2000$, providing insights into the characteristics of the second-order phase transition. 43

4.6. Expected value of the position $\langle X \rangle$ as the order parameter, illustrating its abrupt change at the critical point $B_2 = 0$ using $K = 6000$, $\xi = \sqrt{2}$ with a basis dimension $N = 2000$. 44

4.7. Left: QF as a function of B_2, highlighting the minimal overlap near the critical point where the phase transition occurs. Right: QFS, S, as a function of B_2, showing a peak near zero. The calculations were performed using $K = 6000$, $\xi = \sqrt{2}$, a basis dimension $N = 2000$, and with a perturbation $\delta B_2 = 0.001$. . . 45

4.8. Analysis of the pure quartic potential $V(X) = X^4$: (a) Energy difference between consecutive levels, (b) Level density estimated using Eq. (4.7) and calculated exactly via Eq. (4.6), and (c) IPR for different basis dimensions. The calculations were performed using $K = 1000$, $\xi = \sqrt{2}$, and a basis dimension $N = 2500$. . . 46

4.9. Graphical analysis of the symmetric double-well potential $V(X) = X^4 - 5X^2$ (only parity even states are represented): (a) Energy difference ΔE between consecutive levels, identifying a minimum near the state $n = 30$ where the ESQPT occurs. (b) Level density, showing an increase around $E = 0$. (c) Participation ratio for different dimensions of the Hamiltonian matrix, highlighting a minimum in participation at $E = 0$ and an increase for $E > 0$, aiding in identifying the critical point of the ESQPT. The calculations were performed using $K = 2000$, $\xi = \sqrt{2}$, and a basis dimension $N = 3000$. 48
4.10. Quantum phase space analysis for the most localized state ($n = 28$, $E = -0.017$) in the symmetric double-well potential, shown using Husimi (left) and Wigner (right) functions. These visualizations illustrate the state's behavior at the critical point of the ESQPT. The calculations were performed using $K = 2000$, $\xi = \sqrt{2}$, and a basis dimension $N = 2500$. 49
4.11. Graphs showing the energy differences, level density, and participation ratio for the asymmetric double-well potential, highlighting critical behavior near the ESQPT. The calculations were performed using $K = 2000$, $\xi = \sqrt{2}$, and a basis dimension $N = 2500$. 50
4.12. Quantum phase space analysis for the most localized state ($n = 54$, $E = 0.054$) in the asymmetric double-well potential. The left panel displays the Husimi function and the right panel shows the Wigner function, both highlighting the effects of the potential's asymmetry on the quantum phase space at the critical point of the ESQPT. The calculations were performed using $K = 2000$, $\xi = \sqrt{2}$, and a basis dimension $N = 2500$. 51

List of Tables

2.1. Elementary Catastrophes of Thom for $k \leq 5$ and one vanishing eigenvalue ($l = 1$). 13
2.2. Notation Conventions 13

E.1. Even eigenvalues and eigenvectors of the pure quartic oscillator with parameters $K = 1$ and $\xi = \sqrt{2}$. 71
E.2. Odd eigenvalues and eigenvectors of the pure quartic oscillator with $K = 1$ and $\xi = \sqrt{2}$. 72
E.3. Matrix elements of $\langle X \rangle_{n,n'}$ for the pure quartic oscillator with $K = 1$ and $\xi = \sqrt{2}$. 73
E.4. Matrix elements of $\langle X^2 \rangle_{n,n'}$ for the pure quartic oscillator with $K = 1$ and $\xi = \sqrt{2}$. 73

Listings

F.1. Function to calculate the Hamiltonian 75
F.2. Function for convergence of eigenvalues and eigenvectors 76
F.3. Function that calculates the Wave Function of the HO 78
F.4. Function that calculates the Wave Function of the HO recursively 78
F.5. Function that calculates the Wave Function of the Quartic Oscillator 79

CHAPTER 1

Introduction

The present Master's Thesis explores the Quantum Cusp Catastrophe (QCC) within the framework of a generalized quartic potential. Classical Catastrophe Theory, developed by René Thom in the 1960s [54, 60], investigates how small and continuous changes in a system's control parameters can lead to sudden, discontinuous effects on dependent variables. Hence, a catastrophe occurs when a small change in the control parameters of a system leads to a sudden and discontinuous change in its behavior and to the emergence of distinct equilibrium states. The term *cusp* stems from a characteristic shape of the catastrophe surface, resembling a cusp or fold in the parameter space. Thom's theory provides the mathematical tools necessary to understand complex, nonlinear systems and their critical behavior. We are interested in how to translate the catastrophe theory results to the quantum realm and search for the signatures of critical phenomena in quantum systems. We explore how criticality affects quantum states, their energies, the energy level density, and other quantities of interest when the system's control parameters are varied. We perform our analysis using a generalized quartic potential as our model, characterized by an inherently anharmonic nature and of interest in many different branches of science.

Mathematically, the Classical Cusp Catastrophe (CCC) is often described by a simple bifurcation equation, which captures the essential dynamics of the system. The canonical form of the cusp catastrophe equation is

$$V(x;a,b) = x^4 + ax^2 + bx \ ,$$

where x represents the system's state variable, a and b are control parameters, and $V(x;a,b)$ denotes the potential energy landscape of the system [20, 51, 60]. A classical system with a potential as the previous one exhibits a cusp catastrophe surface in the (a,b) parameter space, leading to abrupt transitions between stable equilibrium states as the control parameters vary [20, 51]. The CCC has been extensively studied in various physical systems, ranging from mechanical oscillators to socio-economic models [12, 45, 60].

If we move from the classical to the quantum domain, we deal with the so called Quantum Cusp Catastrophe (QCC), after the seminal work of R. Gilmore in his paper titled *Quantum Cusp* [22] where he investigated the qualitative features of a quantum-mechanical system whose potential in the classical limit undergoes a cusp catastrophe. Gilmore's study examined key aspects such as the energy spectrum, density of states, and operator expectation values, all analyzed as functions of the cusp control parameters. In the present work, we walk over Gilmore's shoulders with the aim of enriching his results establishing a connection between the quantum cusp and *quantum phase transitions*.

Thermal phase transitions are pivotal in understanding how a system's properties change as it transitions from one state of aggregation to another. These transitions are governed by control parameters and, at the critical value of such parameters, a small variation results in

abrupt changes in the system's properties. Similarly, QPTs occur in quantum systems when changes in control parameters, which are part of the Hamiltonian of the system, lead to abrupt changes in the ground state properties. The main difference is that QPTs are zero-temperature phase transitions that take place due to quantum fluctuations, instead of thermal ones. The QPTs can be classified using an extension of Ehrenfest's criteria, determining a phase transition order upon the non-analyticity of ground state energy's derivatives. First-order QPTs involve discontinuities in the first derivative, while continuous transitions involve discontinuities in the second or higher derivative [35].

The exploration of QPTs has grown significantly in recent years, with extensive studies conducted on various physical systems. Moreover, the study of Excited State Quantum Phase Transitions (ESQPTs), which extend the concept of quantum phase transitions from the ground state to excited states, has gained traction [5, 8, 10, 36, 37, 47, 53, 61]. ESQPTs are characterized by singularities or discontinuities in the density of states or other properties at certain critical energies. The significance of ESQPTs lies in their ability to reveal structural changes in the energy spectrum and provide a deeper understanding of quantum dynamics.

The research presented in this thesis is primarily theoretical, supplemented by numerical demonstrations and analyses of phenomena that elude a purely analytical treatment. The generalized quartic potential is a model designed to capture the essence of a system where varying control parameters leads to significant changes in the phase space, such as the transition from a single critical point to multiple critical points or the deformation of potential wells. Although other models, e.g. the Lipkin-Meshkov-Glick model, the Kerr oscillator, Dicke model or the Iteracting Boson Model (IBM), between others [9, 10, 36, 61], can exhibit similar behavior, the choice of a generalized quartic potential is motivated by its simplicity and effectiveness in illustrating the fundamental concepts. However, it is a model that has been used numerous times to model spontaneous symmetry breaking and anharmonic potentials in different branches of science. In addition to this, the infinite dimension of the Hilbert space associated to the model hinders the numerical calculations.

We would like to emphasize that nowadays theoretical research like the present one is becoming increasingly relevant in the context of modern quantum information technologies and quantum simulators. There is an increasing number of quantum analog computers that enable the artificial construction and measurement of systems that behave according to predetermined, often simplified, Hamiltonians [1, 4, 16]. Furthermore, in the realm of adiabatic quantum computing, quantum phase transitions are pivotal. The practical implementation of adiabatic quantum algorithms seeks to design adiabatic paths that avoid quantum phase transitions, as their occurrence can cause the adiabatic process to diverge, rendering the problem-solving approach impractical [4, 42]. Beyond quantum computing, QPTs are also significant in other fields of physics, such as condensed matter physics, where they play a crucial role in understanding phenomena like superconductivity [28] or the quantum Hall effect [30] and in the quest for new and exotic phases of matter. In nuclear physics, QPTs are essential for studying the collective behavior of nucleons within atomic nuclei [9]. The insights gained from studying QPTs in simple models like the one used in this thesis can therefore have broad implications, contributing to the advancement of both theoretical and experimental physics.

1.1. OBJECTIVES

We aim to thoroughly investigate the Quantum Cusp Catastrophe (QCC) within a generalized quartic potential, both from classical and quantum perspectives, providing insights into quantum systems near their critical points. The specific objectives are:

- **Classical model analysis:** Perform a theoretical analysis of the classical model, focusing on critical points, phase diagrams, potential forms, and the canonical form of the cusp

catastrophe.

- **Extension to the quantum domain:** Extend the analysis to the quantum realm by solving the time-independent Schrödinger equation for the quartic oscillator and examining the quantum analog of the classical cusp catastrophe.
- **Quantum phase transitions study:** Investigate ground state and excited state quantum phase transitions (QPTs and ESQPTs) dependence on the Hamiltonian's control parameters and the order and nature of such transitions.
- **QPTs and ESQPTs detection and characterization:** Identify and analyze physical quantities that detect QPTs and ESQPTs, even in finite-sized systems, and explore the relationship between quantum and classical limits, based on system size.

These objectives are designed to enhance the understanding of the QCC and its implications for quantum phase transitions.

1.2. THESIS STRUCTURE

This thesis is organized into several chapters, each focusing on different aspects of the study of the Quantum Cusp Catastrophe in a Generalized Quartic Potential. The structure of the thesis is as follows:

1.2.1. Chapter 2: Quartic Potential Theory and the Cusp Catastrophe

In Chapter 2, we focus on the classical aspects of the quartic potential and the cusp catastrophe, providing a brief overview of the fundamentals of Catastrophe Theory. The chapter is divided into several sections:

- **The Quartic Oscillator**: This section introduces the quartic oscillator, where, starting from the generalized quartic potential, we study the critical points of the oscillator for two cases, with linear or cubic terms apart from the quartic and quadratic ones. We explore the phase diagram and potential structure for the two cases. In both cases, the system exhibit one or two minima, depending on the values of the control parameters.
- **Catastrophe Theory**: In this section we provide a brief overview of Catastrophe Theory, focusing particularly on presenting the canonical form of the Cusp Catastrophe.
- **Cusp Catastrophe**: This section focuses on the cusp catastrophe, where we show the form of this catastrophe in the parameter space and explore the phase space of the classical quartic oscillator. We also introduce some quantities that will be relevant once we study quantum phase transitions, such as the order parameter and level density. Additionally, we use this catastrophe to briefly discuss the phenomenon of spontaneous symmetry breaking.

1.2.2. Chapter 3: Quantum Quartic Potential and the Quantum Cusp

In Chapter 3 we extend the study to the quantum realm, focusing on obtaining a Hamiltonian in second quantization, solving the time-independent Schrödinger equation, defining a convergence analysis, and introducing the quantum cusp catastrophe. The chapter includes the following sections:

- **The Quantum Quartic Oscillator**: We begin by discussing the quantum version of the quartic oscillator, presenting the second quantization formalism to solve the time-independent Schrödinger equation using a one-dimensional Harmonic Oscillator (HO) basis.
- **Convergence Analysis**: This section presents a detailed analysis of the convergence properties of the quantum quartic oscillator, ensuring the reliability of the computed eigenvalues of the Hamiltonian as a function of the truncated Harmonic Oscillator basis.

- **Quantum Potential**: We explore the quantum potential landscape and its influence on the behavior of quantum states, emphasizing the role of anharmonicity and its effects on energy levels.
- **Quantum Phase Space**: This section introduces the concept of quantum phase space, utilizing Wigner and Husimi functions to visualize the distribution of quantum states in phase space.
- **Quantum Cusp**: We investigate the quantum cusp catastrophe, introducing several connections to quantum phase transitions.

1.2.3. Chapter 4: Ground and Excited State Quantum Phase Transitions

In Chapter 4, we focus on quantum phase transitions (QPTs) in the context of the quartic potential. The chapter is structured as follows:

- **Ground State Quantum Phase Transitions**: This section examines the behavior of the ground state of the quantum quartic oscillator, identifying and analyzing first- and second-order QPTs that occur as control parameters are varied.
- **Excited State Quantum Phase Transitions**: We extend the analysis to excited states, exploring how quantum phase transitions manifest in higher energy states and their implications.

The detailed analysis and findings presented in these chapters provide a comprehensive understanding of the Quantum Cusp Catastrophe and its relationship with quantum phase transitions, supported by both theoretical insights and numerical results.

CHAPTER 2

The Quartic Potential and the Cusp Catastrophe

2.1. THE QUARTIC OSCILLATOR

The quartic potential, often referred to as the quartic oscillator, is a fourth-order polynomial potential and, therefore, it has an anharmonic nature. As we show in this chapter, the quartic oscillator exhibits one or two minima, depending on the values assigned to the control parameters. If the potential is a purely quartic one, it has a single minimum that, at first sight, might look alike a harmonic oscillator but with a flatter bottom and a positive anharmonicity (adjacent levels energy gap increases with excitation energy). If the control parameter associated with the quadratic term is negative, the potential features two minima, that can be symmetric or asymmetric depending on the value of the control parameter for the odd power term. This potential, also known as a Mexican hat, Champagne bottle, or double-well potential, represents a versatile toy model that captures essential aspects of various physical systems and constitutes one of the clearest examples of relevant phenomena such as bifurcations or spontaneous symmetry breaking, with applications in various fields [3, 20, 51].

A general one-dimensional fourth-order potential, $V(x)$, can be defined as

$$V(x) = A_4\, x^4 + A_3\, x^3 + A_2\, x^2 + A_1\, x\ , \tag{2.1}$$

where we assume that the fourth-order term is a confining quartic potential, therefore $A_4 > 0$. For the sake of convenience, we study two cases in detail

$$V_i(x) = A_4\, x^4 + A_i\, x^i + A_2\, x^2\ , \tag{2.2}$$

where $i = 1, 3$. The classical Hamiltonian for the $V_i(x)$ potentials (2.2) is

$$\mathbf{H}_i(x, P) = \frac{1}{2m} P^2 + A_4 x^4 + A_i x^i + A_2 x^2\ . \tag{2.3}$$

Expressing this equation in a more convenient form using dimensionless coordinate and momentum (see Appendix A),

$$H_i(q, p) = \frac{1}{2} p^2 + q^4 + a_i q^i + a_2 q^2\ . \tag{2.4}$$

2.1.1. Critical Points and Stability

The Hamiltonian (2.4) exemplifies an *autonomous natural Hamiltonian*[1] with equations of motion given by

$$\dot{q} = \frac{\partial H}{\partial p} = f_q(q,p) = p \ , \tag{2.5}$$

$$\dot{p} = -\frac{\partial H}{\partial q} = f_p(q,p) = -4q^3 - ia_i q^{i-1} - 2a_2 q \ . \tag{2.6}$$

From this pair of equations, the critical or stationary points of Hamiltonian (2.4) can be found as the values q_c, p_c such that $\dot{q} = \dot{p} = 0$.

A common approach to characterize the nature of critical points involves the linearization of the problem in the vicinity of each critical point [39, 52]. This entails a coordinate change to $\delta z = z - z_c$ for $z = (q,p)$, where $z_c = (q_c, p_c)$ are the critical point phase space coordinates. The variational equations then take the form $\dot{\delta z} = L\delta z$, where the constant matrix L is determined as

$$L = J\mathcal{H}_f\left[H(z_c)\right] \ , \tag{2.7}$$

with J being the Poisson matrix given by

$$J = \begin{bmatrix} 0 & I_n \\ -I_n & 0 \end{bmatrix} \ , \tag{2.8}$$

where I_n blocks are n dimensional unity matrices. $\mathcal{H}_f\left[H(z_c)\right]$ is the Hamiltonian Hessian matrix that for the one-dimensional (two-variable) case is

$$\mathcal{H}_f\left[H(q_c,p_c)\right] = \begin{bmatrix} \frac{\partial^2 H(q,p)}{\partial q^2} & \frac{\partial^2 H(q,p)}{\partial p \partial q} \\ \frac{\partial^2 H(q,p)}{\partial p \partial q} & \frac{\partial^2 H(q,p)}{\partial p^2} \end{bmatrix}_{z_c=(q_c,p_c)} \ . \tag{2.9}$$

The classification of critical points depends on the values of the two eigenvalues of the linearization matrix L, denoted as λ_1 and λ_2, which are the roots of the characteristic polynomial $\det(L - \lambda I)$. Hyperbolic equilibrium points have non-zero real parts for both eigenvalues, resulting in distinct types such as nodes and focuses. Specifically, according to [33, 39, 52]:

- If λ_1 and λ_2 are real and have the same sign, the critical point is a *node*. A node is considered stable if both eigenvalues are positive ($\lambda_1 > 0$ and $\lambda_2 > 0$), while it is unstable if both eigenvalues are negative ($\lambda_1 < 0$ and $\lambda_2 < 0$). If the signs of λ_1 and λ_2 are different, the critical point is a saddle point.
- If λ_1 and λ_2 are complex conjugate, denoted as $\lambda_1 = a + ib$ and $\lambda_2 = a - ib$, the critical point is a *focus* point, also known as a *spiral* point. The stability of a focus point depends on the value of a: it is unstable if $a > 0$ and stable if $a < 0$.

On the other hand, if at least one of the eigenvalues is zero or has a zero real part, the equilibrium is considered *non-hyperbolic*, indicating that the system is not structurally stable. Several types of non-hyperbolic equilibrium points exist, with the more relevant ones being [33, 39, 52]:

[1] An autonomous Hamiltonian is non-explicitly time-dependent ($\partial H/\partial t = 0$) while a natural Hamiltonian can be expressed as $H(q,p) = T(q,p) + U(q)$.

- If λ_1 and λ_2 are complex conjugate with a zero real part ($a = 0$), the critical point is a *centre*, characterized by periodic orbits flowing around it.
- If one of the two eigenvalues is zero, the critical point is in a *saddle-node equilibrium*, and the system undergoes a *saddle-node bifurcation*, resulting from the coalescence of a saddle point and a node. This configuration is always unstable.
- If both eigenvalues are zero, the configuration is again unstable and referred to as a *Bogdanov-Takens equilibrium*, associated with the *Bogdanov-Takens bifurcation*.

2.1.1.1. Critical Points in the cubic case ($i = 3$)

As mentioned above, we focus on two cases that share a quartic confining term and a squared term plus either a cubic (a_3) or a linear (a_1) term, as indicated in Equation (2.4).

In the quartic potential with cubic and quadratic terms case, the equations of motion (2.5) and (2.6) yield the following critical points

$$\dot{q} = \frac{\partial H}{\partial p} = f_q(q,p) = p_c = 0\,, \tag{2.10}$$

$$\dot{p} = -\frac{\partial H}{\partial q} = f_p(q,p) = -4q_c^3 - 3a_3q_c^2 - 2a_2q_c = 0\,. \tag{2.11}$$

Therefore, $p_c = 0$ in all cases, and with three different q_c values: $q_c = 0$, and the curves in control parameter space $q_c = \frac{3a_3 \pm \sqrt{9a_3^2 - 32a_2}}{-8}$. Hence, for this case, the three critical points as a function of the control parameters a_2 and a_3 are

$$(1) \quad (q_{c1}, p_c) = (0,0), \tag{2.12}$$

$$(2) \quad (q_{c2}, p_c) = \left(\frac{3a_3 + \sqrt{9a_3^2 - 32a_2}}{-8}, 0\right), \tag{2.13}$$

$$(3) \quad (q_{c3}, p_c) = \left(\frac{3a_3 - \sqrt{9a_3^2 - 32a_2}}{-8}, 0\right). \tag{2.14}$$

Stability of the solutions Once the stationary points are known, we study their stability, which depends on the values of the parameters a_2 and a_3. According to the approach outlined earlier, the simplest method to determine the character of the critical points is by linearization in the vicinities of the critical point. Considering equations (2.7), (2.8), and (2.9), the linearization matrix L is given by

$$L = J\mathcal{H}_f\,[H(z_c)] = \begin{bmatrix} 0 & 1 \\ -(12q_c^2 + 6a_3q_c + 2a_2) & 0 \end{bmatrix}, \tag{2.15}$$

and the eigenvalues of the linearization matrix L are obtained from

$$\begin{vmatrix} -\lambda & 1 \\ -(12q_c^2 + 6a_3q_c + 2a_2) & -\lambda \end{vmatrix} = 0, \tag{2.16}$$

leading to

$$\lambda_1 = -\lambda_2 = \sqrt{-(12q_c^2 + 6a_3q_c + 2a_2)}. \tag{2.17}$$

As expected, eigenvalues λ_1 and λ_2 have opposite signs, and considering that the parameters a_2 and a_3 have real values, the classification of stability for the three critical points found is as follows

- If λ_1 and λ_2 are real and have opposite signs, the critical point is hyperbolic and a saddle point.
- If λ_1 and λ_2 are complex conjugate with a zero real part, the critical point is a centre.
- If both λ_1 and λ_2 are equal to zero, the critical point is a doubly degenerate equilibrium point that in our case will drive the system into a Pitchfork Bifurcation.

For the first critical point, $(q_{c1}, p_{c1}) = (0, 0)$, the eigenvalues are:

$$\lambda_1 = +\sqrt{-2a_2}, \quad \lambda_2 = -\sqrt{-2a_2}. \tag{2.18}$$

According to the classification above:

- If $a_2 < 0$, then $\lambda_1 = -\lambda_2 \in \mathbb{R}$, so $(q_{c1}, p_{c1}) = (0, 0)$ is a saddle point.
- If $a_2 = 0$, then $\lambda_1 = -\lambda_2 = 0$, so the points $(q_{c1}, p_{c1}) = (0, 0)$ is doubly degenerated (and It drives the system into the Pitchfork Bifurcation).
- If $a_2 > 0$, then $\lambda_1 = -\lambda_2$ are pure imaginary values, so $(q_{c1}, p_{c1}) = (0, 0)$ is a stable centre.

Regarding the other two critical points, for the point (q_{c2}, p_{c2}) (eq. (2.13)), we have

$$\lambda_{1,2} = \pm\frac{\sqrt{64a_2 - 18a_3^2 - 6a_3\sqrt{-32a_2 + 9a_3^2}}}{4}, \tag{2.19}$$

while for (q_{c3}, p_{c3}) (eq. (2.14))

$$\lambda_{1,2} = \pm\frac{\sqrt{64a_2 - 18a_3^2 + 6a_3\sqrt{-32a_2 + 9a_3^2}}}{4}. \tag{2.20}$$

The stability classification of the latter two points is more complex, but it still follows the criteria mentioned earlier: both are either stable centers, saddle points, or they are doubly degenerated in the case of a pitchfork bifurcation taking place between the two configurations. Additionally, it is noteworthy that q and p are real numbers; therefore, the critical points (q_{c2}, p_{c2}) and (q_{c3}, p_{c3}) only exist in Region II of Figure 2.1, defined for values of a_2 and a_3 fulfilling

$$a_2 \leq \frac{9a_3^2}{32}.$$

In summary, the nature of the three critical points can be summarized in the following figure, which illustrates the parameter space and where we have highlighted regions with according to the number of critical points, marked their boundaries, and included schematic potential functions (Hamiltonian evaluated for $p = 0$) associated with particular values of the parameters.

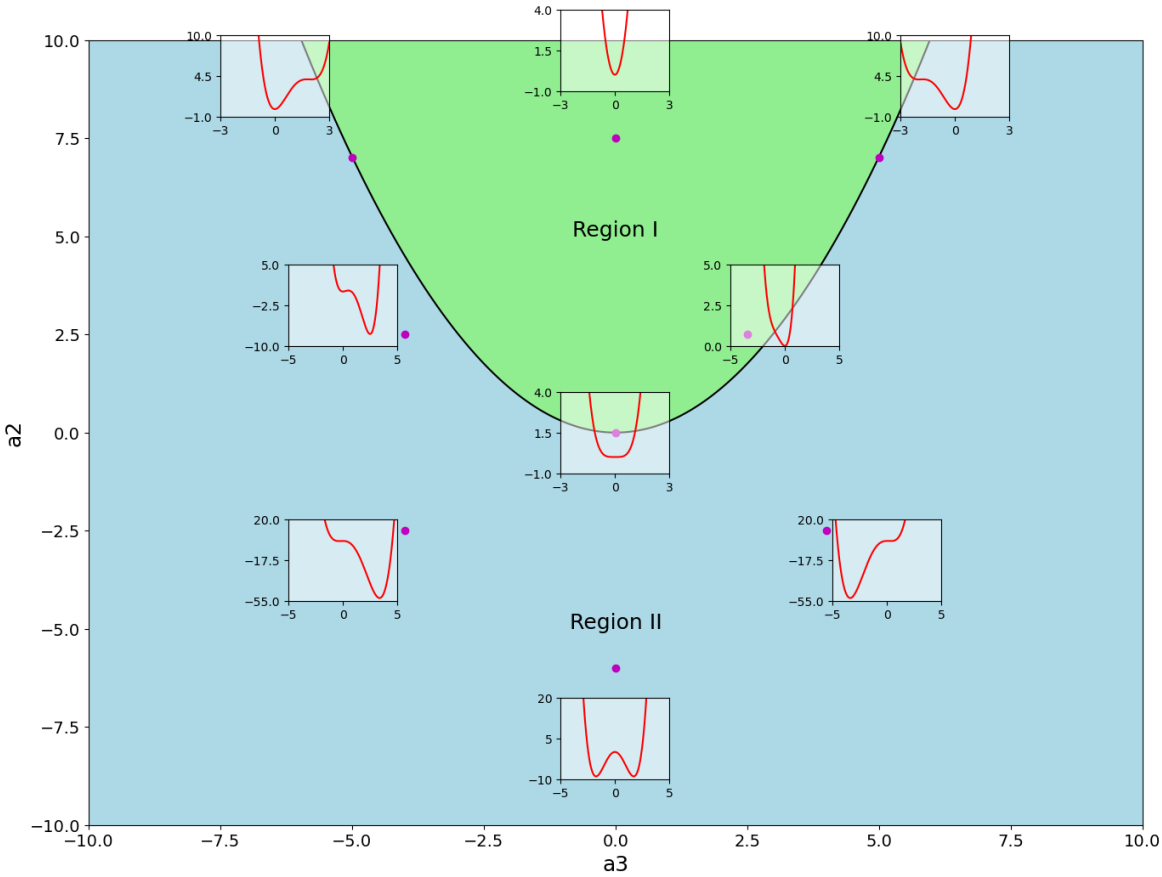

Figure 2.1: Summary of the configuration of the three critical points in the cubic case.

Therefore, the number of relative extrema in the potential $V(x)$ is determined by the values of the parameters a_2 and a_3. As depicted in Figure 2.1, we observe that in the a_2 and a_3 parameter space

- Within region I, there is only one minimum in the potential that is a centre in phase space.
- In region II, we have two minima (two stable centers in phase space) and one maximum in the potential that is a saddle point in phase space.

This analysis provides insight into the quartic potential phase space configuration based on the values of the cubic and quadratic parameters. The pitchfork bifurcation and the presence of multiple minima and a maximum demonstrates the versatility and richness of the potential landscape.

2.1.1.2. Critical Points in the linear case ($i = 1$)

Now, we consider the case where the odd non-zero term is linear (a_1). In this case, we have a quartic potential plus quadratic and linear terms, the equations of motion (2.5) and (2.6) lead to the following critical points:

$$\dot{q} = \frac{\partial H}{\partial p} = f_q(q,p) = p_c = 0 \,, \tag{2.21}$$

$$\dot{p} = -\frac{\partial H}{\partial q} = f_p(q,p) = -4q_c^3 - 2a_2 q_c - a_1 = 0 \,. \tag{2.22}$$

As in the previous case, we have in all cases $p_c = 0$ and a cubic equation with three solutions for q_c. Let $D = 8a_2^3 + 27a_1^2$, $A = \sqrt[3]{-\frac{27}{8}a_1 + \frac{1}{8}\sqrt{27D}}$, and $B = -\frac{3a_2}{2A}$. Then, the solutions for q_c are given by Cardano equations [44]

$$q_{c1} = \frac{1}{3}(A + B), \tag{2.23}$$

$$q_{c2} = \frac{1}{3}(\rho A + \rho^2 B), \tag{2.24}$$

$$q_{c3} = \frac{1}{3}(\rho^2 A + \rho B), \tag{2.25}$$

where $\rho = e^{\frac{2\pi i}{3}} = -\frac{1}{2} + \frac{i\sqrt{3}}{2}$.

Stability of the solutions Next, let's analyze the stability of each critical point, which depends on the values of the parameters a_1 and a_2. Considering equations (2.7), (2.8), and (2.9), the linearization matrix L is given by:

$$L = J\mathcal{H}_f\left[H(z_c)\right] = \begin{bmatrix} 0 & 1 \\ -(12q_c^2 + 2a_2) & 0 \end{bmatrix} \tag{2.26}$$

where the eigenvalues of L are obtained from:

$$\begin{vmatrix} -\lambda & 1 \\ -(12q_c^2 + 2a_2) & -\lambda \end{vmatrix} = 0, \tag{2.27}$$

leading to:

$$\lambda_1 = +\sqrt{-(12q_c^2 + 2a_2)}, \quad \lambda_2 = -\sqrt{-(12q_c^2 + 2a_2)}. \tag{2.28}$$

Similarly to the previous case, due to the signs of the eigenvalues λ_1 and λ_2, and considering that the parameters a_1 and a_2 are real, the stability classification of these critical points follows the criteria mentioned above: they can either be stable centres, saddle points, or they are doubly degenerated.

In this specific case, the curve in the parameter space of a_1 and a_2 which delimits the classification of the critical points and the shape of the potential, is given by:

$$27a_1^2 + 8a_2^3 = 0 \tag{2.29}$$

This equation arises from setting the discriminant D equal to zero; the equation $D = 8a_2^3 + 27a_1^2 = 0$ determines the stability of our critical points.

- When $D > 0$, we have a single critical point that behaves as a stable centre.
- When $D = 0$, we the critical points are doubly degenerated.
- When $D < 0$, we have three critical points: two stable centres and a saddle point.

The different potential shapes obtained in the linear case are included in Figure 2.2.

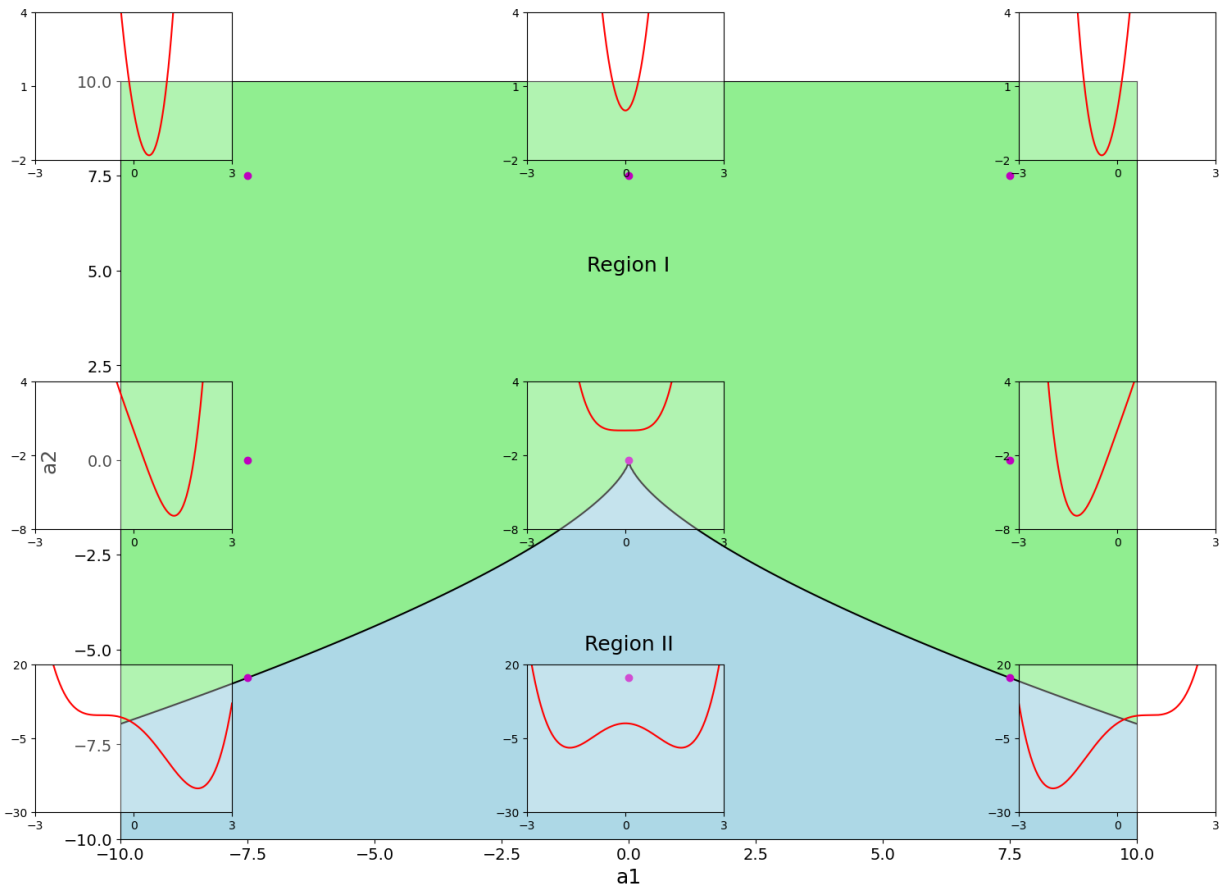

Figure 2.2: Phase diagram of the quartic potential plus quadratic and linear terms. This summarizes the configuration of the three critical points in the cusp catastrophe.

We would like to emphasize that the obtained potential shapes and phase diagram configurations are equivalent in the the linear and cubic cases: there is either one or three critical points, which behave as centers or saddle points and may be doubly or triply degenerate depending on the region of the parameter space they are in. This can be understood making use of the Catastrophe Theory canonical form of the Cusp Catastrophe: $A_3 = x^4 + ax^2 + bx$. Catastrophe Theory is a branch of Mathematics, with plenty of applications in different areas, that provides a universal framework for studying dynamical systems and whence they undergo abrupt changes under small changes in their control parameters. As we will see in next section, both the linear and cubic cases belong to the same elementary catastrophe, the *Cusp Catastrophe*. In order to make this clear, we will briefly explore Catastrophe Theory to understand why the linear case is the canonical form of the Cusp Catastrophe.

2.2. CATASTROPHE THEORY

Catastrophe Theory, developed by René Thom in the 1960s [54, 60], is a branch of mathematics that studies how small and continuous changes in control parameters are associated with sudden and discontinuous effects on dependent variables. Such discontinuities or jump-like changes are also known as phase-transitions or catastrophes. Thom aimed to apply ideas from differential topology and topological dynamics to natural phenomena exhibiting *catastrophic* changes (sudden and dramatic discontinuities). In this section, we outlined the main principles of Catastrophe Theory and demonstrate the derivation of the canonical form equation of catastrophes in general and, in particular, we focus on the Cusp Catastrophe, $A_3 = x^4 + ax^2 + bx$ [20, 22, 51, 60]. This section is mostly based on the seminal reference *Catastrophe Theory for Scientists and Engineers* by Prof. Robert Gilmore [20].

2.2.1. Elementary Catastrophes

We limit our approach to a simple yet physically relevant setting in which to consider Thom's ideas: a gradient dynamical system [51]

$$\frac{dx}{dt} = -\nabla_x V(x;c), \tag{2.30}$$

where $V(x;c)$ is a potential function incorporating control variables c that affect the state of the system. $V(x;c)$ yields a scalar for each state x and a vector of control variables c. Of particular interest are the equilibrium equations $\nabla_x V(x;c) = 0$ of dynamical and gradient systems. This equation may have no solutions (e.g. $V(x) = x$), one solution (e.g. $V(x) = x^2$), or more than one solution (e.g. $V(x;c) = x^4 + cx^2$, with one solution for $c \geq 0$ and three for $c < 0$). Using CT, many useful and powerful statements can be inferred about the possible equilibria of gradient systems and their dependence on the control parameters c. Elementary Catastrophe Theory studies the dependence of stationary points x_c of $V(x;c)$ on the control parameters c.

The first step to understand Catastrophe Theory is the definition of Morse critical points.

Morse Critical Points

The Morse Lemma states that the physical system is in equilibrium (stable or unstable) at a particular point in the state space where $\nabla V = 0$ [20]. As we know, the stability properties of the equilibrium are determined from the eigenvalues of the Hessian matrix $\mathcal{H}_f = \partial^2 V/\partial x_i \partial x_j$. The critical points at which the Hessian matrix determinant is nonzero, $\det \mathcal{H}_f \neq 0$, are called *isolated*, *non-degenerate*, or *Morse* critical points. In this case, the Morse theorem guarantees the existence of a smooth change of variables (in general nonlinear) such that the potential can be expressed locally as a quadratic form

$$V_{\text{Morse}}(x) \doteq \sum_{i=1}^{n} \lambda_i y_i^2 \ , \tag{2.31}$$

where λ_i are the eigenvalues of the stability matrix $\mathcal{H}_f$ evaluated at the equilibrium. The symbol $\doteq$ is introduced to emphasize that a smooth change of variables was performed.

Non-Morse Critical Points

The critical points of $V(x_1, x_2, \ldots, x_n)$ at which $\det \mathcal{H}_f = 0$ are called *non-isolated*, *degenerate*, or *non-Morse* critical points.

If the potential depends on k control parameters $c_1, \ldots, c_k$, the stability matrix $\mathcal{H}_f$ and its eigenvalues $\lambda_1, \lambda_2, \ldots$ also depend on these control parameters. One or more of the eigenvalues $\lambda_i(c)$ may be zero for certain values of the control parameters. Whenever this happens, $\det \mathcal{H}_f = 0$, the conditions required for the validity of the Morse Lemma ($\nabla V = 0, \det \mathcal{H}_f \neq 0$) are no longer satisfied, and the canonical form for a potential at an equilibrium (2.31) is no longer valid. However, it is still possible to find a canonical form for the potential at a non-Morse critical point. If l eigenvalues $\lambda_1(c), \ldots, \lambda_l(c)$ vanish at $c = c_0$, then the Thom's Splitting Lemma [20] may be used to split the potential into a non-Morse and a Morse parts:

$$V(x,c) \doteq f_{NM}(y_1(x;c), \ldots, y_l(x;c), c) + \sum_{j=l+1}^{n} \lambda_j(c) y_i^2(x) \tag{2.32}$$

The l non-Morse coordinates $y_1, \ldots, y_l$, associated with the l vanishing eigenvalues $\lambda_1(c), \ldots, \lambda_l(c)$, are smooth functions of both the n state variables $x_1, \ldots, x_n$ and the k

control parameters $c_1, \ldots, c_k$. The Morse coordinates $y_{l+1}, \ldots, y_n$, associated with the non-vanishing eigenvalues $\lambda_{l+1}(c), \ldots, \lambda_n(c)$, are smooth functions only of the original state variables $x_1, \ldots, x_n$. At (x_0, c_0), the stability matrix $\partial^2 V/\partial y_i \partial y_j$ (for $1 \leq i, j \leq l$) vanishes (all matrix elements are 0), while the $(n-l) \times (n-l)$ stability matrix of the Morse coordinates is non-singular. Under suitable conditions ($k \leq 5$ and if no special or symmetry conditions are present in the family of potentials $V(x, c)$), Thom's theorem guarantees the existence of a smooth changes of variables so that the potential can be written in a canonical form

$$V(x, c) = CG(l) + \sum_{j=l+1}^{n} \lambda_j x_j^2 \tag{2.33}$$

The function $CG(l)$ is called a catastrophe germ. Table 2.1 lists all the canonical catastrophe germs for $k \leq 5$ and only one ($l = 1$) vanishing eigenvalue.

Table 2.1: Elementary Catastrophes of Thom for $k \leq 5$ and one vanishing eigenvalue ($l = 1$).

Name	Nomenclature	k	Germ	Perturbation
Fold	A_2	1	x^3	ax
Cusp	A_3	2	x^4	$bx + ax^2$
Swallowtail	A_4	3	x^5	$cx + bx^2 + ax^3$
Butterfly	A_5	4	x^6	$dx + cx^2 + bx^3 + ax^4$
-	A_6	5	x^7	$ex + dx^2 + cx^3 + bx^4 + ax^5$

In summary, the local character of a potential is described by a sequence of theorems of functional analysis with an increasing intimacy with topology. When $\nabla V = 0$ and $\det \mathcal{H}_f \neq 0$, the Morse Lemma can be used to transform the V potential into the canonical form (2.31). When $\nabla V = 0$ and $\det \mathcal{H}_f = 0$, the Morse Lemma is not valid. But if $V(x, \lambda)$, $x \in \mathbb{R}^n$ and $\lambda \in \mathbb{R}^k$ is a typical k-parameter family of potentials, the theorem of Thom can be used to cast V into the canonical form (2.33).

For the sake of clarity, the terms *critical point* and *equilibrium* or *stationary* point have different meanings in the literature of mathematics and physics, as indicated in Table 2.2. As we can tell, what we were denoting as *critical points* when we study of the stability of the Hamiltonian, are the non-Morse critical points. Therefore, these are the points we will mostly focus on in this outline of Catastrophe Theory.

Table 2.2: Notation Conventions

Property	Mathematics	Physics
$\nabla V \neq 0$	Non-critical point	Nonequilibrium point
$\nabla V = 0, \det \mathcal{H}_f \neq 0$	Critical point (Morse)	Equilibrium point
$\nabla V = 0, \det \mathcal{H}_f = 0$	Non-Morse critical point (degenerate)	Critical point

2.2.2. Germ functions

In Catastrophe Theory, the term *germ* refers to the simplest forms of functions that retain the essential qualitative features of the system near their critical points. Canonical forms are crucial for understanding the behavior of dynamical systems under small perturbations and transformations. In the present section we focus on the changes of variables needed to obtain canonical forms, and we specifically address the case with one vanishing eigenvalue, ($l = 1$).

Change of variables

To analyze physical processes in $\mathbb{R}^n$, we often set up a coordinate system $(x_1, x_2, \ldots, x_n)$. Any coordinate system can be transformed into another coordinate system $(x'_1, x'_2, \ldots, x'_n)$ through

a series of transformations. Such general transformations can be expressed in a Taylor series expansion:

$$x_i' = A_i + \sum_j A_{ij}x_j + \sum_{j,k} A_{ijk}x_jx_k + \sum_{j,k,l} A_{ijkl}x_jx_kx_l + \dots \ , \tag{2.34}$$

where A_i, A_{ij}, A_{ijk}, and A_{ijkl} are coefficients of the transformation at different orders.

To simplify the potential function near a critical point, we employ a sequence of transformations, typically starting with an inhomogeneous linear transformation to displace the origin:

$$x_i' = x_i + A_i \ , \tag{2.35}$$

followed by an homogeneous linear transformation to rotate and stretch the coordinate axes

$$x_i'' = \sum_j A_{ij}x_j' \ , \tag{2.36}$$

where the matrix A_{ij} is nonsingular, i.e. $\det|A_{ij}| \neq 0$.

The final step is an *axis-preserving* nonlinear transformation that maintains the coordinate axes at the origin

$$x_i''' = x_i'' + \sum_{j,k} A_{ijk}x_j''x_k'' + \sum_{j,k,l} A_{ijkl}x_j''x_k''x_l'' + \dots \ . \tag{2.37}$$

Application to the $l = 1$ case: one vanishing eigenvalue

Consider a k-parameter family of functions where there is only one non-Morse variable, x with a critical value $x_c = 0$. Near the critical point, the non-Morse function can be expanded in a Taylor series

$$f_{NM}(x;c) = t_0 + t_1x + t_2x^2 + t_3x^3 + t_4x^4 + \dots \ . \tag{2.38}$$

Since $x_c = 0$ is a critical point, the constant term t_0 and the linear term t_1 are zero. The function $f_{NM}(x;c)$ must have a stationary point at $x_c = 0$, so $\frac{\partial f_{NM}}{\partial x}$, must vanish at $x = 0$. Therefore, the linear term t_1 must be zero to ensure that $f_{NM}(x;c)$ has a flat tangent at the critical point. Additionally, t_0, representing the value of the function at the critical point, can be set to zero without loss of generality, as we are primarily interested in the behavior of the function around the critical point, not its absolute value. Thus, the remaining terms in the Taylor expansion are

$$f_{NM}(x;c) = t_2(c)x^2 + t_3(c)x^3 + t_4(c)x^4 + \dots, \tag{2.39}$$

where $t_2(c) = \lambda(c)$, and $t_3(c), t_4(c), \dots$ are functions of the control parameters c_α.

We choose control parameters $c \in \mathbb{R}^k$ such that $t_2 = t_3 = \dots = t_{k+1} = 0$ at $c = c_0$. At this point, the first nonzero term in the Taylor series is t_{k+2}

$$f_{NM}(x;c_0) = t_{k+2}x^{k+2} + \text{higher terms.} \tag{2.40}$$

To show that all higher terms can be removed by a smooth change of variables, we consider the function

$$f(x) = t_nx^n + t_{n+1}x^{n+1} + \dots \ , \tag{2.41}$$

and the transformation

$$x' = A_1x + A_2x^2 + A_3x^3 + \dots \ . \tag{2.42}$$

Our aim is to demonstrate that $f(x)$ is qualitatively the same as $\pm x^n$ by setting $f'(x') = \pm(x')^n$ and equating it to $f(x)$:

$$\pm(A_1x + A_2x^2 + A_3x^3 + \dots)^n = t_nx^n + t_{n+1}x^{n+1} + \dots \ . \tag{2.43}$$

By comparing the coefficients, we get:

$$
\begin{aligned}
x^n &: \quad \pm A_1^n && = t_n, && (2.44)\\
x^{n+1} &: \quad \pm n A_1^{n-1} A_2 && = t_{n+1}, && (2.45)\\
x^{n+2} &: \quad \pm \left(n A_1^{n-2} A_3 + \binom{n}{2} A_1^{n-2} A_2^2 \right) && = t_{n+2}, && (2.46)\\
&\vdots
\end{aligned}
$$

If n is even, the sign on the left-hand side of (2.44) is chosen based on whether t_n is positive or negative. If n is odd, this sign can always be positive. Once A_1 is determined from (2.44), A_2 can be uniquely determined from (2.45), which is linear in this unknown. This process continues for higher terms, leading to the determination of all A_j from the subsequent equations.

The transformation $x' = x'(x)$ defined by (2.42) allows the function $f_{NM}[x(x')]$ to be written as:

$$f_{NM}(x') = \pm (x')^n. \tag{2.47}$$

In the case of a system having k control parameters and only one vanishing eigenvalue, the leading term in the Taylor series expansion of $f_{NM}(x;c)$ is typically not beyond than $\pm x^{k+2}$, and the non-Morse function can be transformed into the canonical form $\pm x^{k+2}$ at the degenerate critical point.

2.2.3. Perturbation of $\pm x^n$

In Catastrophe Theory, perturbations of potential functions near critical points play a crucial role in understanding how small changes in control parameters can affect the qualitative behavior of a system. Perturbations are required to describe all the qualitative changes that a perturbation can produce in the neighborhood of a non-Morse critical point, so they allow us to study the stability and bifurcations of equilibrium points, providing insights into the robustness of the observed phenomena.

We start with the most general perturbation function $p(x;c)$ near a critical point, which can be expressed as:

$$p(x;c) = p(0;c) + p_i x_i + p_{ij} x_i x_j + \dots \tag{2.48}$$

where $p(0;c)$ is a constant term (which can be set equal to 0), p_i are the coefficients of the linear terms, and p_{ij} are the coefficients of the quadratic terms. These coefficients depend on the control parameters c.

The goal is to understand how these perturbations affect the canonical form of the potential. For a function $f(x;c)$ with a non-Morse critical point at x_0, the perturbed function can be written as

$$F = f + p = f_{\mathrm{NM}}(x_1, \dots, x_l) + \sum_{i=l+1}^{n} \lambda_i x_i^2 + p(x_1, \dots, x_n)\,. \tag{2.49}$$

To find the canonical form of the perturbed function, it is convenient to first introduce a homogeneous linear transformation (eq. (2.36)) to diagonalize the quadratic terms [20]. This leads to

$$F' = p_i x_i' + \sum_{i=l+1}^{n} \lambda_i x_i'^2 + f'_{\mathrm{NM}}(x_1', \dots, x_l') + \text{higher-order terms} \tag{2.50}$$

where the new coordinates x_i' are obtained by diagonalizing the quadratic form. For $i = 1, \ldots, l$, the coefficients λ_i' are small, and for $i = l+1, \ldots, n$, the coefficients λ_i' are significant.

Next, we apply an axis-preserving nonlinear transformation (eq. (2.37)) to remove as many higher-order terms as possible. By focusing on the higher-order terms, we can transform the perturbed function into a simpler form. The transformation preserves the coordinate axes at the origin and simplifies the function. For instance, we want to remove terms of degree greater than two in the "good" variables $x_{l+1}, \ldots, x_n$.

This leads us to the canonical form for the perturbed non-Morse function:

$$F = F_{\mathrm{NM}} + F_{\mathrm{M}} \tag{2.51}$$

where

$$F_{\mathrm{NM}} = f_{\mathrm{NM}}(x_1', \ldots, x_l') + p(x_1', \ldots, x_l') \tag{2.52}$$

$$F_{\mathrm{M}} = \sum_{i=l+1}^{n} \lambda_i x_i'^2 + p(x_{l+1}', \ldots, x_n') \tag{2.53}$$

Perturbation of a Morse function F_{M} at a Morse critical point does not affect the qualitative properties of the function in the neighborhood of the Morse critical points. For non-Morse functions, the canonical form will be derived next.

For a single variable x, the most general perturbation of $\pm x^n$ can be expressed as:

$$F(x) = p(0; c) + p_1 x + p_2 x^2 + \ldots + p_{n-1} x^{n-1} + (\pm 1 + p_n) x^n + p_{n+1} x^{n+1} + \ldots \tag{2.54}$$

Using the continuity argument and smooth variable changes, we simplify the function by transforming away higher-degree terms, preserving the canonical form. With the transformations (2.37) and (2.36), it leads to:

$$F''(x'') = p_1 x'' + p_2 x''^2 + \ldots + p_{n-1} x''^{n-1} \pm x''^n \tag{2.55}$$

Finally, an inhomogeneous linear transformation (2.35) is introduced to eliminate one of the powers of x, this is $x'' \longrightarrow x''' = x'' - s$, which leads to

$$F'''(x''') = p_1''(s + x''') + p_2''(s^2 + 2s x''' + x'''^2) + \ldots$$

$$+ p_{n-1}''(s^{n-1} + \ldots + x'''^{n-1}) \pm (s^n + \ldots + n s x'''^{n-1} + x'''^n) \tag{2.56}$$

The $(n-1)$st power can be eliminated because its coefficient $p_{n-1}'' \pm ns$ is the simplest. This coefficient can always be set equal to 0 by setting $s = \mp p_{n-1}''/n$. Then, we can write it as:

$$F'''(x''') = p_1 x''' + p_2 x'''^2 + \ldots + p_{n-2} x'''^{n-2} \pm x'''^n \tag{2.57}$$

Then, we have shown that a general k-parameter family of non-Morse functions with one vanishing eigenvalue can be reduced to its canonical form:

$$F_{NM} \doteq \pm x^{k+2} + \sum_{i=1}^{k} a_i x^i. \tag{2.58}$$

2.3. CUSP CATASTROPHE

As we have seen from the previous analysis, the canonical form of the Cusp Catastrophe corresponds to the quartic potential plus quadratic and linear terms case, whose critical points and stability have been already studied. In CT notation, this is denoted as $A_3 = x^4 + ax^2 + bx$.

The Cusp Catastrophe is one of the simplest, most pervasive, and most studied elementary catastrophes. It is characterized by the fact that the equilibrium points of the system can exhibit a sudden jump as the control parameters are varied, leading to a pitchfork bifurcation in the system's behavior. This is depicted in the surface plots of the non-Morse critical points shown in Figures 2.3a and 2.3b.

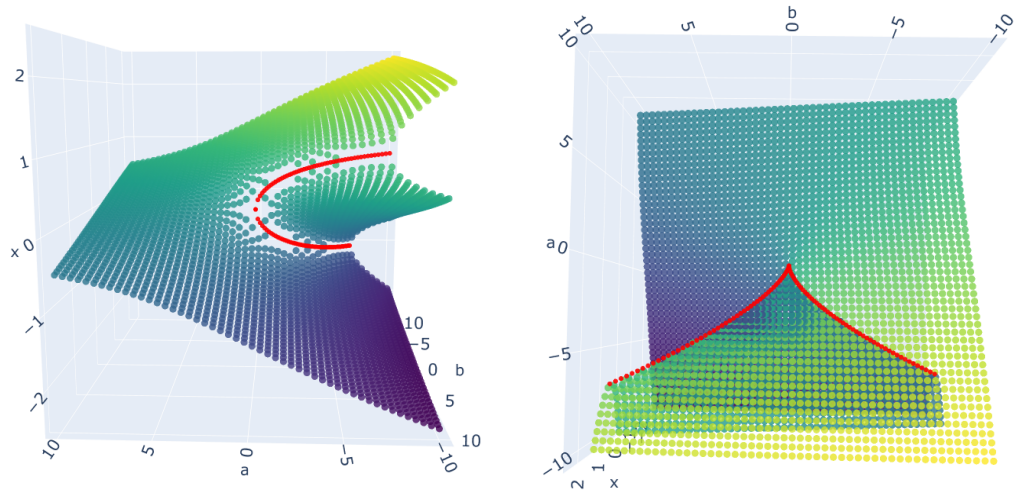

(a) **(b)**

Figure 2.3: (a) The surface formed by the x values that satisfy $\frac{dV(x)}{dx} = 0$ as a function of parameters a and b. The inflection points (satisfying $\frac{d^2V(x)}{dx^2} = 0$) are drawn in red. (b) The same surface from a top view, showing that the projection of the inflection points onto the a-b plane matches the equation (2.29) that determines the stability of critical points, as shown in Figure 2.2.

The behavior of the potential function and its critical points can be better understood by examining the inflection points, where $\frac{d^2V}{dx^2} = 0$. The red curves in Figures 2.3a and 2.3b highlight these inflection points. In the top view provided in Figure 2.3b, the projection of these inflection points onto the a-b plane corresponds to the stability boundary described by the equation (2.29). As we already noticed, this curve is the frontier between regions in the parameter space where the critical points of the potential function exhibit different stability characteristics (only one critical point acting as a stable centre for point outside of the first region, and three critical points inside of the second region 2.2).

2.3.1. Spontaneous Symmetry Breaking

Spontaneous symmetry breaking occurs when a system that is symmetric under a group of transformations finds its equilibrium in a state that has a lower symmetry. In the context of Cusp Catastrophe, this can be illustrated by considering the transition from a single- to a double-well potential.

Imagine a particle resting in the equilibrium position of our potential. When $b = 0$ and $a \geq 0$, the potential $V(x) = x^4 + ax^2$ has a single symmetric well, and the particle is in equilibrium at the origin, ($x = 0$). In this state, the system is symmetric because the potential is invariant under the transformation $x \longrightarrow -x$. However, as the parameter a varies and becomes

negative, the potential shape changes. Specifically, when $a < 0$, the potential $V(x) = x^4 + ax^2$ develops two symmetric wells equidistant from the origin. Despite the potential remaining symmetric, the presence of a symmetric double well enforces an asymmetric outcome, because classically the particle must eventually settle down in one of the wells. In this scenario, the particle final equilibrium state is at one of the two minima at $x = \pm\sqrt{|a|/2}$. This breaks the original symmetry of the potential in an *spontaneous* way because the particle, due to fluctuations or minute changes in the initial conditions, chooses one well over the other. The symmetry of the potential does not dictate which minimum the particle will settle in, leading to the final asymmetric outcome.

As we proceed to explain below, the resulting states after the spontaneous symmetry breaking process can be described using an *order parameter*, which is zero when the system is in the symmetric phase (single well) and non-zero in the broken symmetry phase (double well).

Order parameter

An order parameter is a measure that indicates the degree of order across boundaries in a phase transition. An example of an order parameter is the local magnetization in a ferromagnetic system (like in the Ising Model). For the Cusp Catastrophe, we can choose the position x of the minimum of the potential as our order parameter O. In the symmetric phase where $a \geq 0$ and $b = 0$, the order parameter $O = \langle x \rangle$ is zero because the particle rests at the origin.

As the parameter a becomes negative, the potential forms a double well, and the order parameter becomes non-zero, reflecting the new equilibrium positions $x = \pm\sqrt{|a|/2}$.

$$\langle x \rangle = \begin{cases} 0 & \text{if the system is in the symmetric phase,} \\ \pm\sqrt{|a|/2} & \text{if the system is in the broken-symmetry phase.} \end{cases} \tag{2.59}$$

This transition from a single- to a double-well potential exemplifies how small changes in a control parameter, in this case the parameter a, can lead to significant and abrupt changes in the state of the system, that undergoes spontaneous symmetry breaking. The order parameter effectively captures this transition, indicating the presence of two distinct phases.

2.4. PHASE SPACE

To conclude this chapter, where we have explored the classical dynamics of the quartic oscillator, we depict the phase space constant energy contours for the classical Hamiltonian corresponding to the Cusp Catastrophe (linear $i = 1$ case) for different values of the control parameters a and b (fig 2.4). The energy contours allow us to observe the critical points studied in this chapter, and later they will also be useful for a comparison with the quantum approach results. Additionally, these plots allow us to introduce a quantity that will be useful in the study of the so called Excited State Quantum Phase Transitions (ESQPTs), namely the level density.

2.4.1. Level Density

The level density (also called excited level density) for a one dimensional Hamiltonian system is defined as [8, 26, 27]

$$\nu(E) = \frac{1}{2\pi} \int_{-\infty}^{\infty} dp \int_{-\infty}^{\infty} dx \delta(E - H(p, x)), \tag{2.60}$$

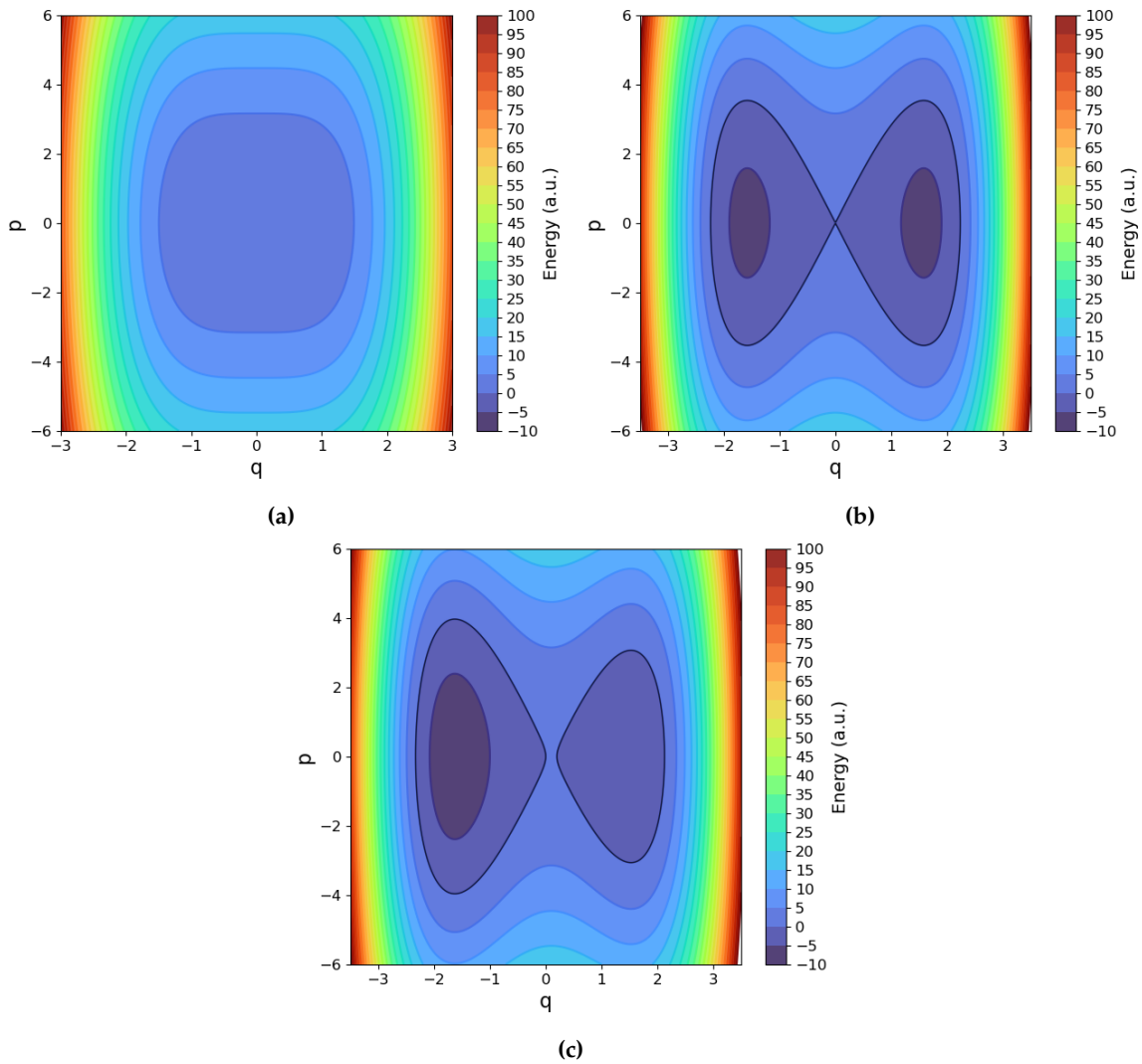

Figure 2.4: Constant energy contours of the phase space for the classical Hamiltonian corresponding to the Cusp Catastrophe for different values of the control parameters a and b. (a) Pure quartic potential $V(x) = x^4$, $a = 0$ and $b = 0$; (b) Symmetric double well potential $V(x) = x^4 - 5x^2$ with $a = -5$ and $b = 0$; and (c) Asymmetric double well potential $V(x) = x^4 - 5x^2 + x$ with $a = -5$ and $b = 1$. Black contour indicates the level in which $E = 0$.

where $H(p, x)$ stands for the classical Hamiltonian (eq. (2.4)) of the system, and $\nu(E)$ is the classical phase-space volume available at energy E (which is essentially the level density). In this equation, one can take into account the composition property of the Dirac delta function, $\delta(g(x)) = \sum_i \delta(x - x_i)/|g'(x_i)|$, where the points x_i are the roots of the equation $g(x) = 0$. In the particular case of the quartic oscillator studied in this work, the level density can be obtained as (See appendix B)

$$\nu(E) \propto \int_{-\infty}^{\infty} \frac{dx}{\sqrt{E - x^4 - ax^2 - bx}} \tag{2.61}$$

This integral can be numerically solved for the values x such that $E \geq x^4 + ax^2 + bx$. Therefore, we can obtain an analytical expression of the level density as a function of the control parameter values. This will be used to classify ESQPTs in the forthcoming chapters.

CHAPTER 3

Quantum Quartic Potential and the Quantum Cusp

3.1. THE QUANTUM QUARTIC OSCILLATOR

As already stated, the classical one-dimensional fourth-order potential, $V(x)$, is defined as

$$V(x) = A_4 x^4 + A_3 x^3 + A_2 x^2 + A_1 x \ , \tag{3.1}$$

where $A_1 > 0$. The shape of the quartic potential can be analyzed for different values of the parameters A_1, A_2, A_3, and A_4. In the simpler case with no odd order terms, $A_1 = A_3 = 0$, there are two symmetrical minima at $x_\pm = \pm x_m$ if $A_2 < 0$, and there is only one minimum if $A_2 \geq 0$, located at the origin.

The quantum Hamiltonian operator for this system is

$$\hat{H} = \frac{p^2}{2M} + V(x) = -\frac{\hbar^2}{2M}\frac{d^2}{dx^2} + \left(A_4\, x^4 + A_3\, x^3 + A_2\, x^2 + A_1\, x\right) \ , \tag{3.2}$$

with the usual commutation relation between coordinate and momentum, $[x, p] = i\hbar$, and where we assume that the system mass can be expressed as $M = Km$. The m factor is the unit mass in the units of interest for the system and K is a dimensionless parameter introduced in the kinetic term to allow for a clean recovery of the classical limit of the system for large K values.

Using dimensionless coordinates and momenta, X and P, defined as [11]

$$X = \frac{x}{\lambda_0} = \left(\frac{8mA_4}{\hbar^2}\right)^{\frac{1}{6}} x \quad \text{and} \quad P = \left(\frac{\lambda_0}{\hbar}\right) p = \left(\frac{1}{8mA_4\hbar^4}\right)^{\frac{1}{6}} p \ ,$$

where $\lambda_0 = \left(\frac{\hbar^2}{8mA_4}\right)^{\frac{1}{6}}$, Hamiltonian (3.2) can be rewritten as

$$\hat{\mathcal{H}} \equiv \frac{\hat{H}}{\epsilon_0} = \frac{4P^2}{K} + X^4 + B_3\, X^3 + B_2\, X^2 + B_1\, X \ , \tag{3.3}$$

where the Hamiltonian has been normalized by the energy scale of the problem, $\epsilon_0 = \left(\frac{A_4\hbar^4}{64m^2}\right)^{\frac{1}{3}}$, and the potential parameters have been redefined as $B_3 = A_3\left(\frac{8m}{A_4^5\hbar^2}\right)^{\frac{1}{6}}$, $B_2 = 2A_2\left(\frac{m}{A_4^2\hbar^2}\right)^{\frac{1}{3}}$, and $B_1 = 2A_1\left(\frac{2m}{A_4\hbar^{2/3}}\right)^{\frac{1}{2}}$.

3.1.1. Second Quantization Formalism and Hamiltonian Transformation

Our aim is to use a Harmonic oscillator basis to expand the solutions of the quartic Hamiltonian and obtain its associated spectrum. In order to solve the time-independent Schrödinger equation using a Harmonic Oscillator (HO) basis, it is convenient to work within the second quantization formalism, introducing harmonic creation and annihilation operators, $a^\dagger$ and a. Second quantization is a powerful formalism used in quantum mechanics to describe systems with an arbitrary number of particles. It is particularly useful when dealing with systems of identical particles, such as atoms or molecules. In second quantization, ladder or creation and annihilation operators, $a^\dagger$ and a, are introduced to represent the addition and removal of particles from quantum states. These operators act on the so called Fock space[1] whose basis components describe the occupation of quantum states by particles. By employing second quantization, we can express the Hamiltonian of the system in terms of such ladder operators, facilitating the study of complex many-body systems.

The 1D Harmonic Oscillator Hamiltonian is given by [13]

$$\hat{H}_{HO} = \frac{p^2}{2m} + V_{HO}(x) = -\frac{\hbar^2}{2m}\frac{d^2}{dx^2} + \frac{1}{2}m\omega^2 x^2 \,. \tag{3.4}$$

The complete treatment of the Hamiltonian using the second quantization formalism is detailed in Appendix C.

The natural energy unit for the HO is $\hbar\omega$ and the natural length unit is $\lambda_0' = \left(\frac{\hbar}{m\omega}\right)^{\frac{1}{2}}$. Defining the unitless coordinate $y = x/\lambda_0'$, we transform the HO Hamiltonian to the form

$$\hat{\mathcal{H}}_{HO} = \frac{\hat{H}_{HO}}{\hbar\omega} = -\frac{d^2}{2dy^2} + \frac{1}{2}y^2 \,. \tag{3.5}$$

The introduction of the creation and annihilation operators defined as $a^\dagger = \frac{1}{\sqrt{2}}\left(y - \frac{d}{dy}\right)$ and $a = \frac{1}{\sqrt{2}}\left(y + \frac{d}{dy}\right)$, transforms the HO Hamiltonian to second quantization to

$$\hat{\mathcal{H}}_{HO} = \frac{\hat{H}_{HO}}{\hbar\omega} = \hat{n} + \frac{1}{2} \tag{3.6}$$

The time-independent Schrödinger equation for a general quartic potential can be solved using a truncated N-dimensional HO basis. To transform the Hamiltonian (3.3) to second quantization, it is worth noticing that two different sets of unitless coordinates were introduced:

$$X = \frac{x}{\lambda_0} \quad \text{and} \quad y = \frac{x}{\lambda_0'}.$$

Therefore, these two different coordinates can be related, leading to

$$X = \xi y, \quad \text{with} \quad \xi = \frac{\lambda_0'}{\lambda_0}. \tag{3.7}$$

Hamiltonian (3.3), once rewritten in second quantization can be expressed as (see Appendix C)

[1] A Hilbert space spanned by Fock states, that are the possible quantum states of a system with a variable number of particles. Each Fock state corresponds to a specific arrangement of particles occupying different energy levels. For instance, in the case of the harmonic oscillator, Fock states describe the occupation of energy levels by particles, where each state is characterized by the number of particles occupying each energy level. These states play an important role in the second quantization formalism, providing a basis for expressing the quantum states of the system in terms of creation and annihilation operators.

$$
\begin{aligned}
\hat{\mathcal{H}} =& E_0 + \left(\frac{4}{K\xi^2} + 3\xi^4 + B_2\xi^2\right)\hat{n} + \frac{3\xi^4}{2}a^{\dagger 2}a^2 \\
&+ \left(\frac{B_1\xi}{\sqrt{2}} + \frac{3B_3\xi^3}{2\sqrt{2}}\right)(a^\dagger + a) + \frac{B_3\xi^3}{2\sqrt{2}}(3a^{\dagger 2}a + 3a^\dagger a^2) \\
&+ \left(\frac{-4K^{-1}\xi^{-2} + 3\xi^4 + B_2\xi^2}{2}\right)(a^{\dagger 2} + a^2) + \xi^4(a^\dagger a^3 + a^{\dagger 3}a) \\
&+ \frac{B_3\xi^3}{2\sqrt{2}}(a^{\dagger 3} + a^3) \\
&+ \frac{\xi^4}{4}(a^{\dagger 4} + a^4)\,,
\end{aligned} \tag{3.8}
$$

where the zero-point energy is $E_0 = \frac{2}{K\xi^2} + \frac{3\xi^4}{4} + \frac{B_2\xi^2}{2}$.

This expression of the Hamiltonian allows us to build its associated matrix in Fock space, whose non-zero elements are

$$\langle n|\hat{\mathcal{H}}|n\rangle = \left(\frac{4}{K\xi^2} + 3\xi^4 + B_2\xi^2\right)n + \frac{3\xi^4}{2}n(n-1) + \frac{2}{K\xi^2} + \frac{3\xi^4}{4} + \frac{B_2\xi^2}{2} \tag{3.9}$$

$$\langle n|\hat{\mathcal{H}}|n-1\rangle = \left(\frac{B_1\xi}{\sqrt{2}} + \frac{3B_3\xi^3}{2\sqrt{2}}n\right)\sqrt{n} \tag{3.10}$$

$$\langle n|\hat{\mathcal{H}}|n-2\rangle = \left(\frac{-4K^{-1}\xi^{-2} + B_2\xi^2 + \xi^4(2n-1)}{2}\right)\sqrt{n(n-1)} \tag{3.11}$$

$$\langle n|\hat{\mathcal{H}}|n-3\rangle = \frac{B_3\xi^3}{2\sqrt{2}}\sqrt{n(n-1)(n-2)} \tag{3.12}$$

$$\langle n|\hat{\mathcal{H}}|n-4\rangle = \frac{\xi^4}{4}\sqrt{n(n-1)(n-2)(n-3)}\,. \tag{3.13}$$

The eigenvalues and eigenfunctions of the quartic oscillator in second quantization, as well as the coordinate space wave functions of the eigenstates, $\Psi(X)$, are obtained by diagonalization of the Hamiltonian matrix, truncated at a given Fock space dimension, and expressing the results in terms of the Fock basis (see Appendix D.2)

$$\hat{\mathcal{H}}\Psi(X) = \epsilon\Psi(X), \quad \Psi(X) = \sum_{i=1}^{N} c_i\psi_i(X), \tag{3.14}$$

where N is the dimension of the truncated Harmonic Oscillator basis, $\{|n\rangle\}$, with $n = 0, \ldots, N-1$. *A priori*, the matrix representation of the Hamiltonian should have infinite dimension; however, to perform the calculations, it is necessary to define a dimension, N, that is finite. So, the following question arises: how do the eigenvalues and eigenstates converge as a function of the dimension of the truncated space, N? To address this problem, in the following section we will study the convergence of the eigenvalues as a function of N.

3.2. CONVERGENCE ANALYSIS

To ensure the reliability of the computed eigenvalues of the Hamiltonian, it is crucial to analyze their convergence as a function of the basis size N. In this section, we present a detailed convergence analysis for the first three eigenvalues E_0, E_1, and E_2 of the Hamiltonian matrix (eq. 3.9-3.13) for varying values of N.

The Hamiltonian matrix was constructed for N ranging from 5 to 65 in steps of 10. The parameters used in the construction were $B_1 = 0$, $B_2 = 0$, $B_3 = 0$ (i.e. the pure quartic potential), $K = 1$, and $\xi = \sqrt{2}$. These specific parameter values are chosen to enable a direct comparison with the results published by Chan and Stelman in their work *Some energy levels and matrix elements of the quartic oscillator* [11]. The computed eigenvalues for each N are shown in Figure 3.1a.

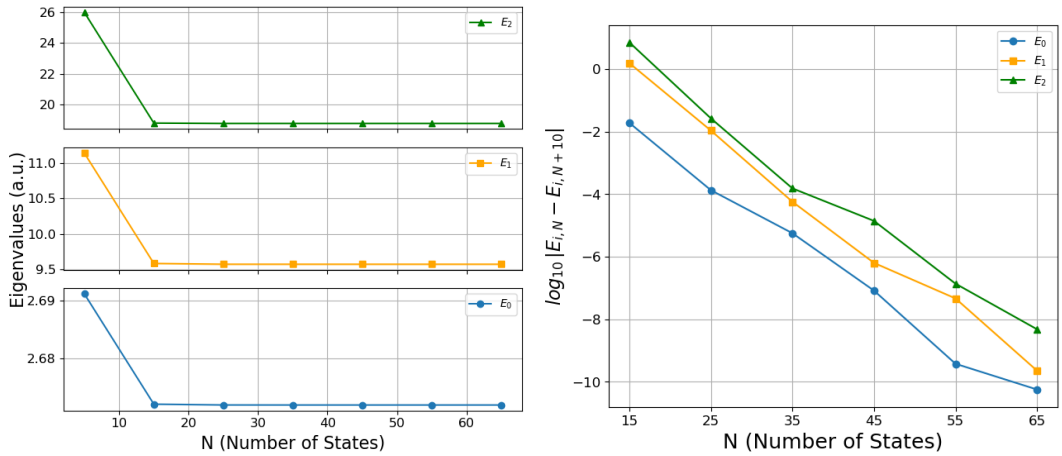

(a) **(b)**

Figure 3.1: (a) Eigenvalues E_0, E_1, and E_2 as a function of the basis size N calculated for the pure quartic potential ($B_1 = B_2 = B_3 = 0$) with parameters $K = 1$, and $\xi = \sqrt{2}$. (b) Logarithmic scale of the absolute differences between successive eigenvalues for E_0, E_1, and E_2 as a function of the basis size N.

From Figure 3.1a, we observe that the eigenvalues E_0, E_1, and E_2 converge to their true values with increasing basis dimension values. This stabilization suggests a way to estimate the dimension N value required to achieve accurate eigenvalue calculations.

To further quantify the convergence, we computed the differences between successive eigenvalues for increasing N. These differences were then plotted in a logarithmic scale, as shown in Figure 3.1b. This figure clearly shows a decreasing trend in the differences between successive eigenvalues on a logarithmic scale. This trend confirms that the eigenvalues E_0, E_1, and E_2 converge as the basis size N increases. Furthermore, in this figure, we can see that to achieve a precision of the three eigenvalues on the order of 10^{-6}, we need at least a dimension $N \approx 55$. In principle, this precision will be what we seek in our study as it is sufficient for our purposes. As we can see, we have found convergence in the eigenvalues, which leads us to the following question: does convergence in the eigenvalues also imply convergence in the eigenvectors? This question will be addressed in the next chapter in the section on ESQTPs (sec. 4.2).

Python codes have been prepared to carry out these calculations. On the one hand, we developed a code to calculate the matrix F.1. Diagonalization is carried out using `NumPy` library functions [29]. On the other hand, we developed a second code that can analyze the convergence of the eigenvalues and increase the dimension N until reaching a desired tolerance F.2. The different codes developed are shown in Appendix F, where a detailed listing of the numerical codes developed for this research is included. These codes are essential for reproducing the results presented in this thesis. Appendix D addresses the computational methodology used for the convergence analysis and the wave functions of the system and presents the specific computational techniques employed to ensure the accuracy and convergence of the eigenvalues, as well as the methods used to compute the obtained wave functions in coordinate space. This appendix includes a thorough explanation of the

convergence criteria and the iterative processes used to achieve the desired precision in the numerical simulations.

3.3. QUANTUM POTENTIAL

Making use of the developed computer codes, we have computed the eigenvalues, eigenvectors, and the the probability density of the states in coordinate space for three different configurations of the quantum potential.

3.3.1. Pure Quartic Potential

In this potential, the values of B_1, B_2, and B_3 are kept at 0, resulting in the potential $V(X) = X^4$ (potential a from Figure 3.8). This case is relevant because it allows us to compare the results obtained in our calculations with those published in [11] for a pure quartic potential with $K = 1$ and $\xi = \sqrt{2}$, achieving perfect agreement for eigenvalues and eigenvectors as well as for the matrix elements of X and X^2 (see Appendix E).

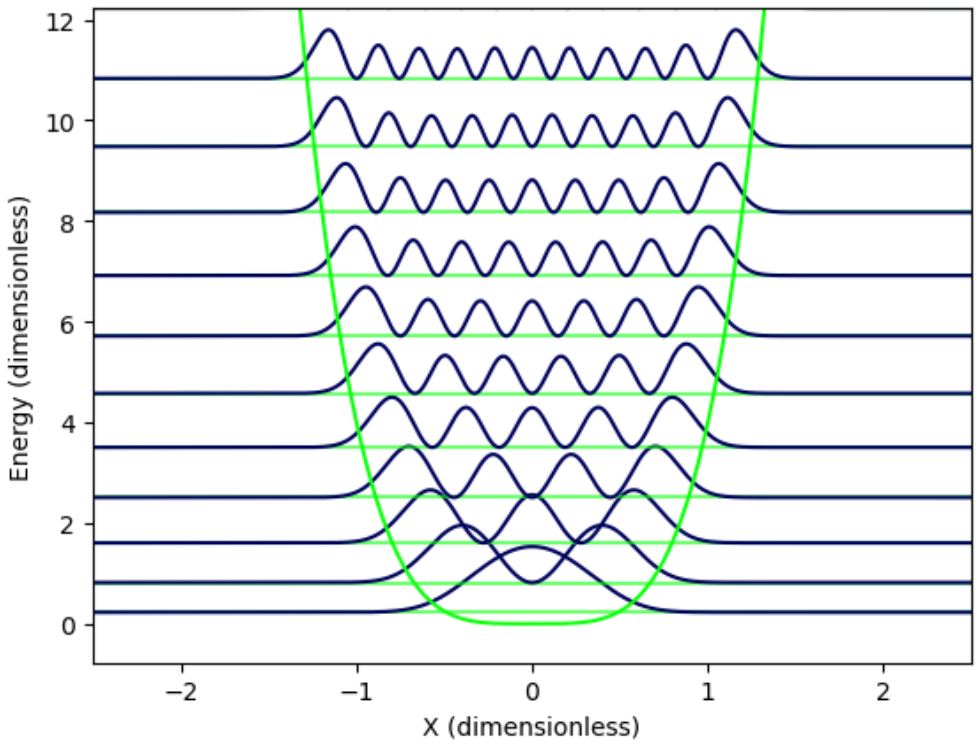

Figure 3.2: Representation of the pure quartic potential $V(X) = X^4$ and the probability density functions of the first twelve eigenstates. The calculations were performed using $B_1 = 0$, $B_2 = 0$, $K = 40$, $\xi = \sqrt{2}$ and a basis dimension $N = 355$, with a convergence tolerance of 10^{-6} for the eigenvalues.

The shape of the pure quartic potential is similar to that of the harmonic oscillator, with a significantly flatter bottom. Figure 3.2 shows the potential curve and the probability density functions for the first twelve eigenstates. The eigenvalues of these states have converged using a tolerance threshold of 10^{-6}. To facilitate the visualization, we used $K = 40$, requiring a dimension $N = 355$ to reach the desired tolerance. Additionally, it can be observed from this graph that the distance between adjacent energy levels grows as the energy increases, indicating that the anharmonicity of this potential is positive.

3.3.2. Symmetric double-well potential

The potential is $V(X) = X^4 - 5X^2$, with $B_1 = 0$. Figure 3.3 displays this potential (shown in green) as a symmetric double-well separated by a potential barrier at $X = 0$. Again, we have represented the probability densities of the eigenstates (shown in blue) for the first twelve eigenstates, with $K = 40$, requiring $N = 355$ to reach a tolerance of 10^{-6}. As can be observed, below the potential barrier ($E < 0$), the states are doubly degenerate[2]. As we approach the barrier maximum, due to a larger quantum tunneling, the degeneration breaks down, states cannot be associated with one of the two wells, and an increase in the level density at $E = 0$ is observed (see Figure 3.3).

The increase in level density at $E = 0$ is a hallmark of the quantum behavior of this system. As the states delocalize between the wells, the wave functions spread over both potential minima, increasing the probability density in regions where the classical potential would suggest minimal presence. This quantum effect results in a higher density of states around $E = 0$, which corresponds to the top of the potential barrier where classical trajectories would not be expected to linger. The breaking of degeneracy is a direct consequence of the coupling between the wells induced by tunneling, and this phenomenon is captured by the convergence of the eigenstates toward this critical energy.

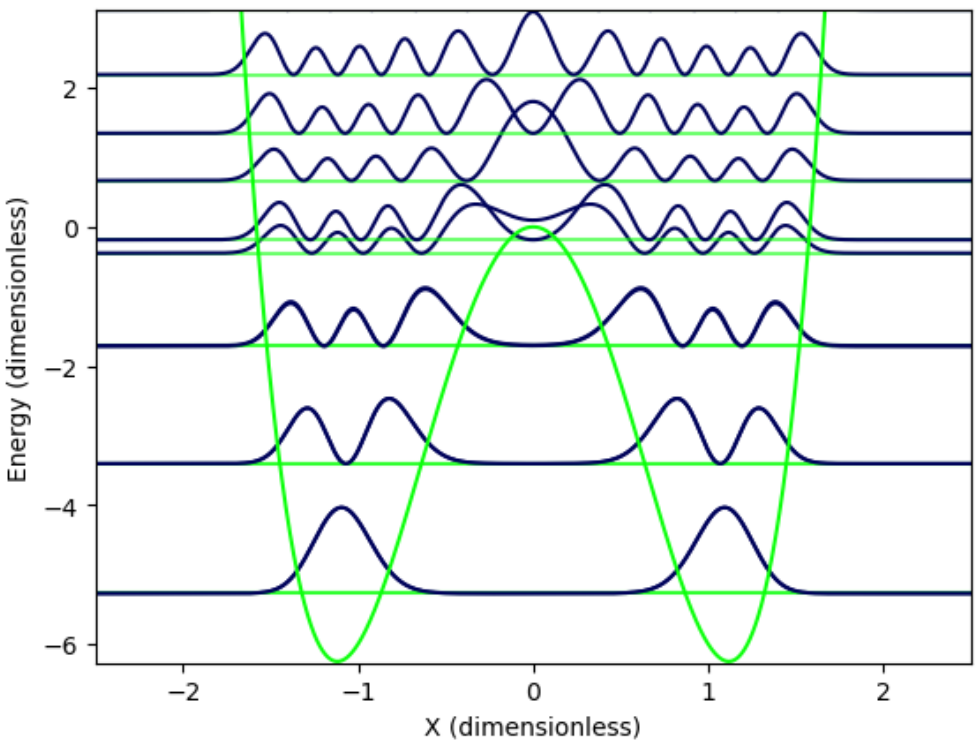

Figure 3.3: Representation of the symmetric double-well potential $V(X) = X^4 - 5X^2$ (shown in green) and the probability functions of the first twelve eigenstates (shown in blue). The figure illustrates the (quasi)degeneration of states below the potential barrier as well as the increase in level density at $E = 0$. Calculations were performed using $B_1 = 0$, $B_2 = -5$, $K = 40$, $\xi = \sqrt{2}$ and a basis dimension $N = 355$, with a convergence tolerance of 10^{-6} for the eigenvalues.

[2]In one-dimensional potentials, true degeneracy does not occur according to the *no-go* theorem, which states that for non-trivial 1D systems, degeneracy can only occur if there is an additional symmetry [15]. What we observe here is a quasidegeneracy, where energy levels are very close but not exactly the same.

3.3.3. Asymmetric Double-Well Potential

The potential used to analyze this case is $V(X) = X^4 - 5X^2 + X$, presented in Figure 3.4. In this potential, the quadratic term maintains the double-well structure, but the inclusion of the linear term introduces an asymmetry in the wells, making one deeper than the other. In this case, representing the first 12 states for $K = 40$ and a tolerance of 10^{-6}, a dimension $N = 415$ was necessary to achieve convergence in the eigenvalues. As seen in this figure, there are no degenerate states in this case.

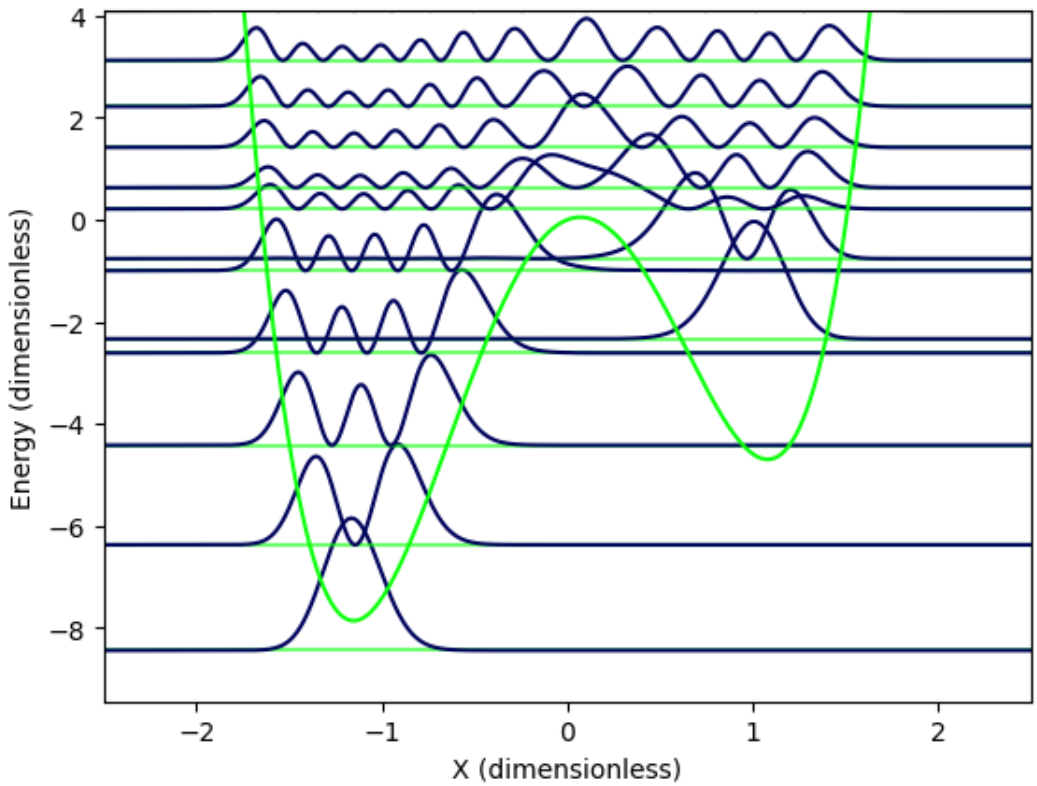

Figure 3.4: Visual representation of the asymmetric double-well potential $V(X) = X^4 - 5X^2 + X$ showing the first twelve eigenstate probability densities in blue. Calculations were performed using $B_1 = 1$, $B_2 = -5$, $K = 40$, $\xi = \sqrt{2}$ and a basis dimension $N = 415$, with a convergence tolerance of 10^{-6} for the eigenvalues.

3.4. QUANTUM PHASE SPACE

In this section we delve into the concepts of the Wigner Function (WF) and the Husimi Function (HF), and their correspondence with classical phase space. Both these quantum distribution functions are invaluable tools for studying the quantum-classical correspondence and the semiclassical aspects of quantum mechanics. The Wigner function associated with a pure state $\Psi(x)$ is defined as [7, 43, 58]

$$W_F(x,p) = \int \frac{dq}{2\pi\hbar} \exp\left(\frac{i}{\hbar}pq\right) \Psi^*\left(x + \frac{q}{2}\right) \Psi\left(x - \frac{q}{2}\right), \tag{3.15}$$

where the integration is performed over all q. Although the Wigner function cannot be interpreted as a conventional probability distribution (as it can take negative values), it provides the correct marginal distributions

$$\int dp\, W_F(x,p) = |\Psi(x)|^2, \quad \int dx\, W_F(x,p) = |\tilde{\Psi}(p)|^2, \tag{3.16}$$

where $\Psi(x)$ and $\tilde{\Psi}(p)$ are the wavefunction in the position and momentum representation, respectively. The Wigner function thus encapsulates both the spatial and momentum representations, providing a unified description of the quantum state in phase space. The WF is particularly suited for the calculation of expectation values of operators in the Weyl ordering [7]. The Husimi function, on the other hand, can be seen as a Gaussian smoothing of the WF, or alternatively, in terms of the projection of the wavefunction onto Gaussian (coherent) states [43]

$$H_F(x,p) = \frac{1}{b\sqrt{2\pi}} \left| \int \frac{dq}{\sqrt{2\pi\hbar}} \Psi(q) \exp\left(-\frac{(x-q)^2}{4b^2} + i\frac{pq}{\hbar} \right) \right|^2 . \tag{3.17}$$

The b parameter, associated with the width of the Gaussian, is not arbitrary in principle; it is related to the size of the coherent state or the standard deviation of the Gaussian, which depends on the physical system in question. In our case, since we nondimensionalized the Hamiltonian, we set $b = 1$. Unlike the WF, the HF is always positive, making it more akin to a classical probability distributions[3], although it does not provide the marginal distributions as the WF does.

The Wigner function can be negative in certain regions of phase space, which is one of the most striking non-classical features of quantum states, as opposed to classical physics where probabilities are always positive [19].

The present calculations for both the WF and the HF were performed for the ground state ($n = 0$). The HF is closer to the classical phase space, as it is remarkably well localized. The WF also provides good results in localizing the minima and maxima. Figure 3.5 display the Wigner and Husimi functions for the ground state ($n = 0$) of the quartic oscillator for different potential configurations. The first set of figures shows the pure quartic potential ($V(X) = X^4$), the second set shows the symmetric double-well potential ($V(X) = X^4 - 5X^2$), and the third set shows the asymmetric double-well potential ($V(X) = X^4 - 5X^2 + X$).

These visualizations highlight the differences between the quantum phase space representations and their classical counterparts, emphasizing the utility of the Husimi function for representing classical-like distributions and the Wigner function for capturing quantum mechanical nuances. We can compare these figures with those for the classical phase space (fig. 2.4), seeing a clear resemblance in the configuration of maxima and minima. Just like in the previous section, we were able to compare our results with those of [43], obtaining an excellent correspondence in the results. For this comparison, we used parameters $K = 1$ and $\xi = 1$, and selected B_1 and B_2 corresponding to the pure quartic potential ($V(X) = X^4$), the symmetric double-well potential ($V(X) = X^4 - 5X^2$), and additionally, we included the asymmetric double-well potential ($V(X) = X^4 - 5X^2 + X$). Figure 3.5 shows the Wigner and Husimi functions for the ground state ($n = 0$), while Figures 3.6 and 3.7 display the Wigner and Husimi functions for the exited states $n = 3$ and $n = 15$, respectively.

[3]The Husimi function is considered a quasidistribution because the coherent state basis is overcomplete, meaning it includes more vectors than are necessary to span the subspace of the Hilbert space. This overcompleteness implies that the basis does not form an orthonormal set. This overcompleteness is why the Husimi function, although always positive, does not qualify as a true probability distribution.

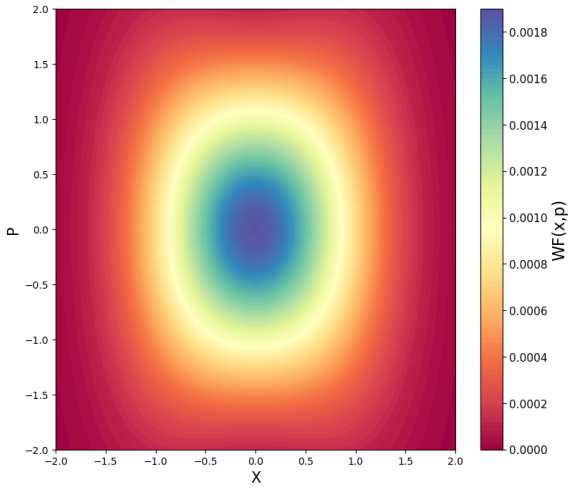

(a) WF for Pure Quartic Potential

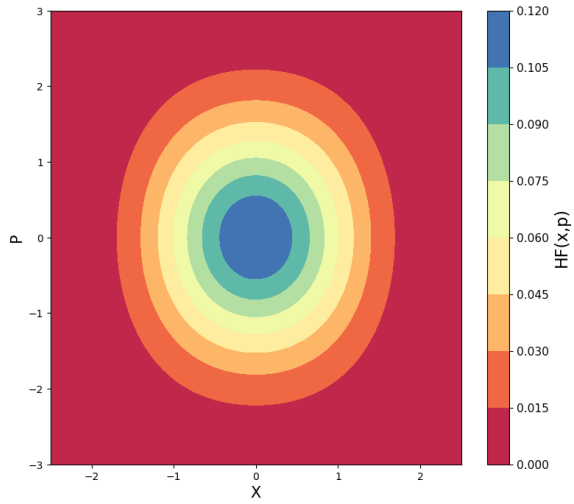

(b) HF for Pure Quartic Potential

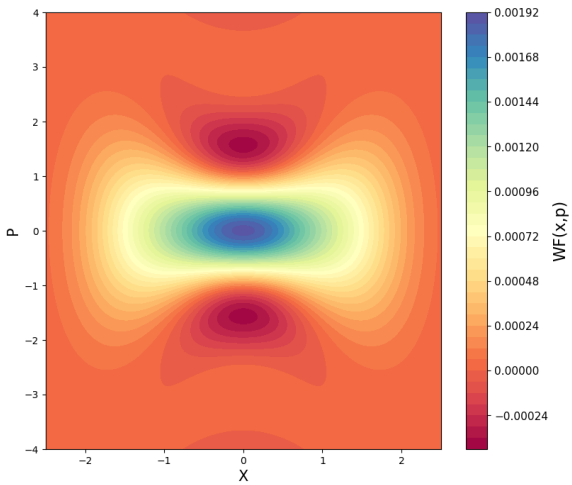

(c) WF for Symmetric Double-Well Potential

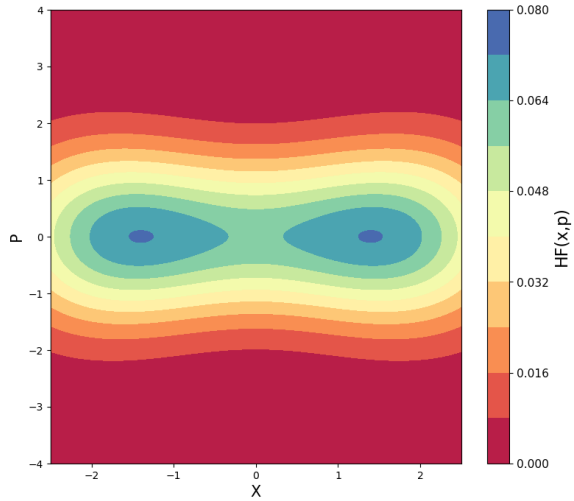

(d) HF for Symmetric Double-Well Potential

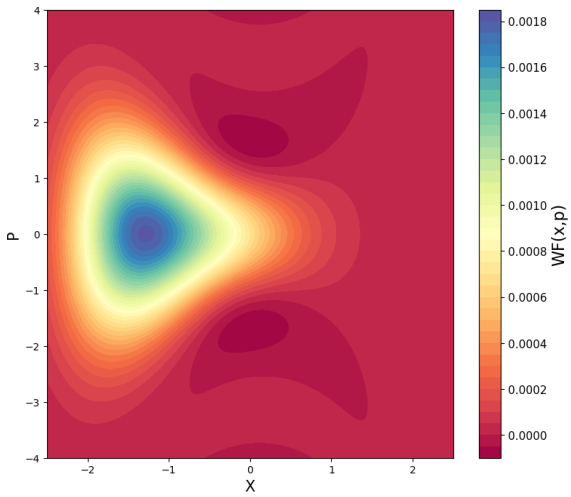

(e) WF for Asymmetric Double-Well Potential

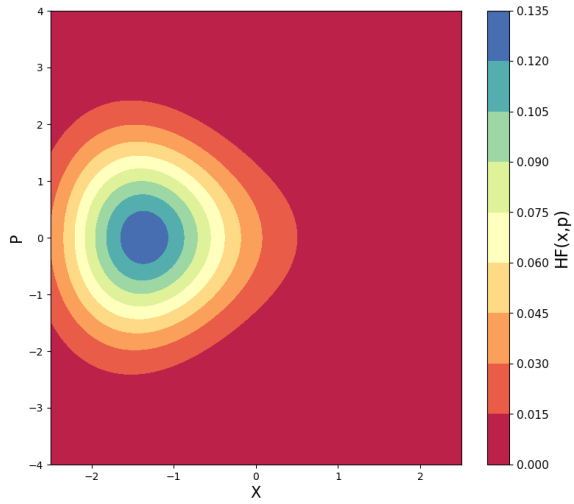

(f) HF for Asymmetric Double-Well Potential

Figure 3.5: Wigner and Husimi Functions for the ground state ($n = 0$) of the quartic oscillator for different potential configurations. Calculations were performed using $K = 1$, $\xi = 1$ and the correspondent values of B_1 and B_2 for each potential.

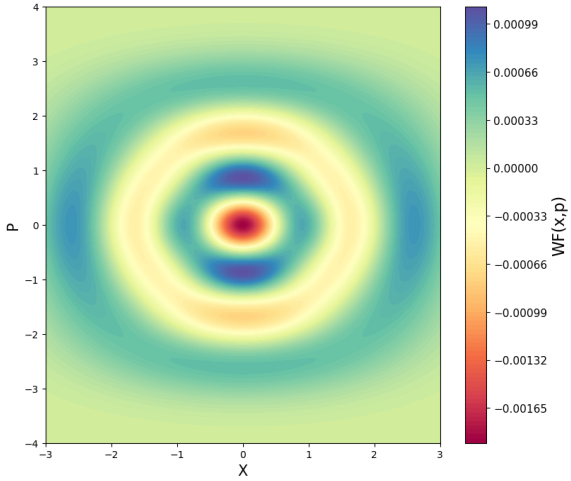

(a) WF for Pure Quartic Potential

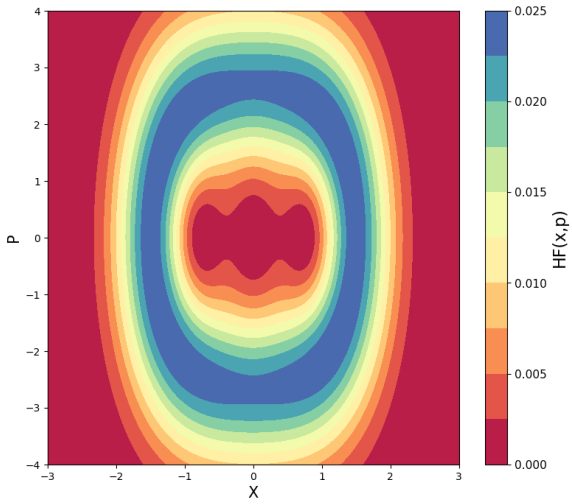

(b) HF for Pure Quartic Potential

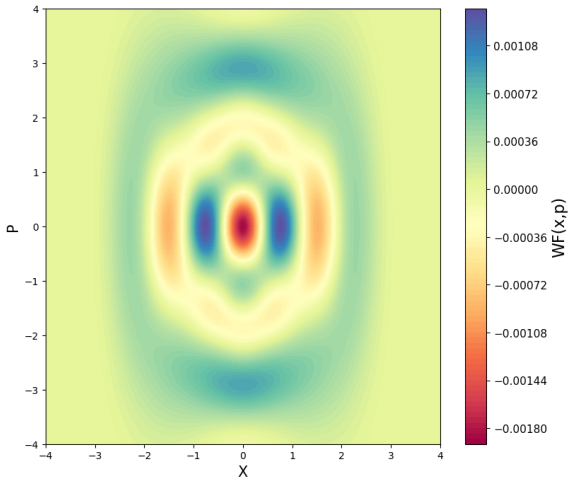

(c) WF for Symmetric Double-Well Potential

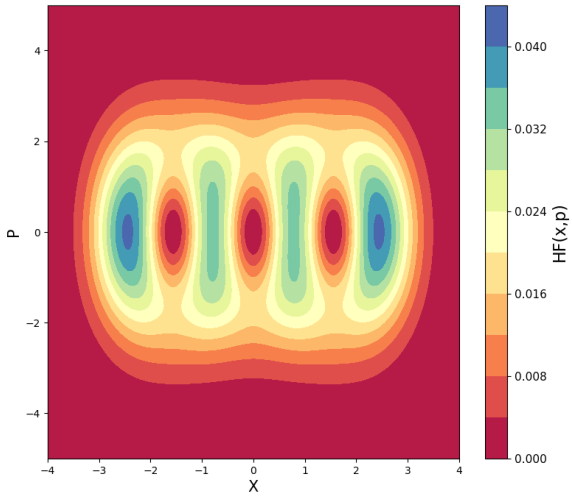

(d) HF for Symmetric Double-Well Potential

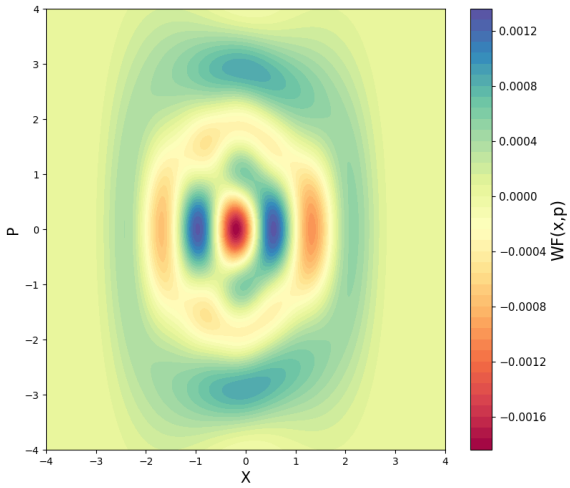

(e) WF for Asymmetric Double-Well Potential

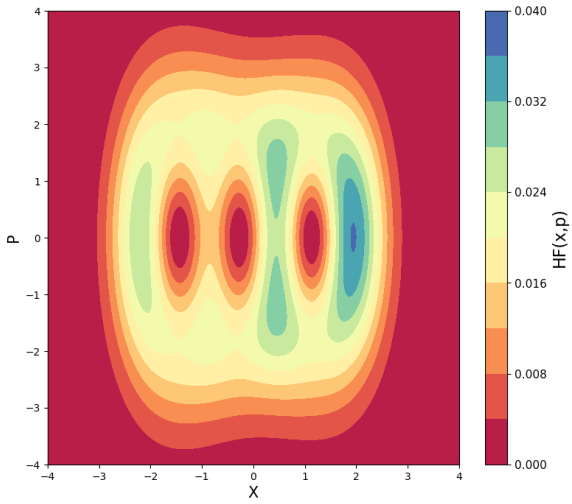

(f) HF for Asymmetric Double-Well Potential

Figure 3.6: Wigner and Husimi Functions for the ground state ($n = 3$) of the quartic oscillator for different potential configurations. Calculations were performed using $K = 1$, $\xi = 1$ and the correspondent values of B_1 and B_2 for each potential.

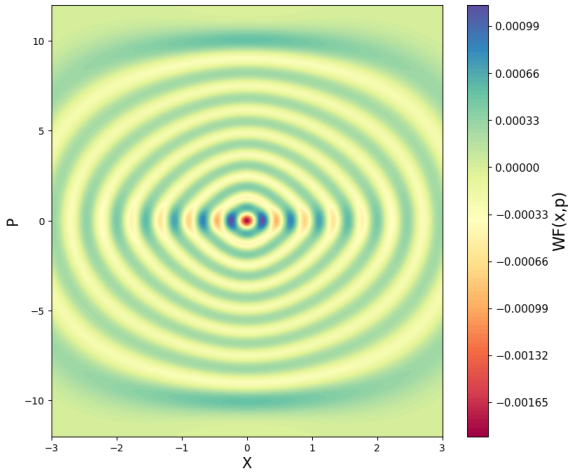

(a) WF for Pure Quartic Potential

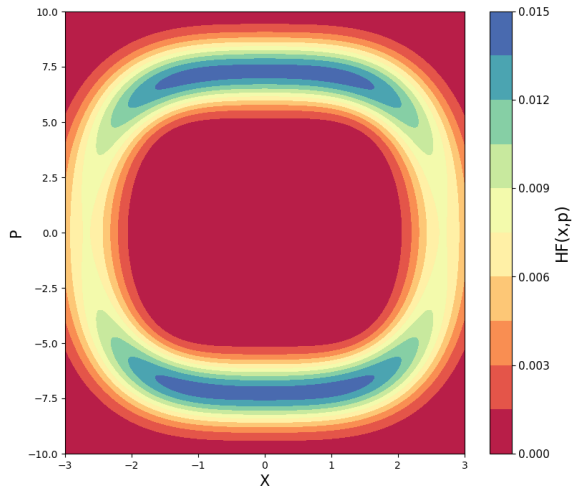

(b) HF for Pure Quartic Potential

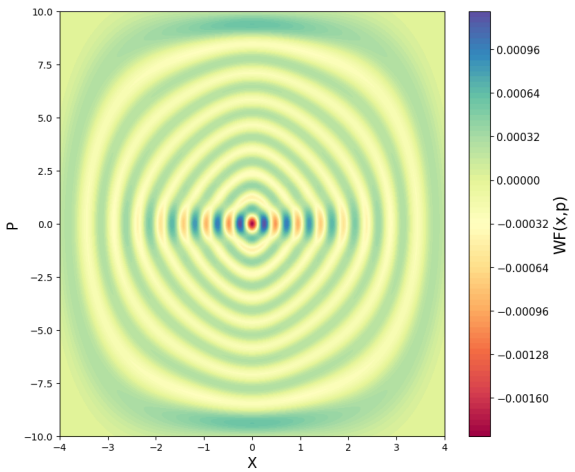

(c) WF for Symmetric Double-Well Potential

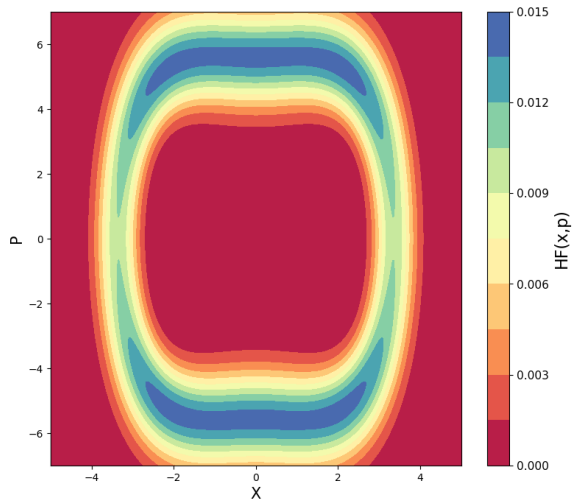

(d) HF for Symmetric Double-Well Potential

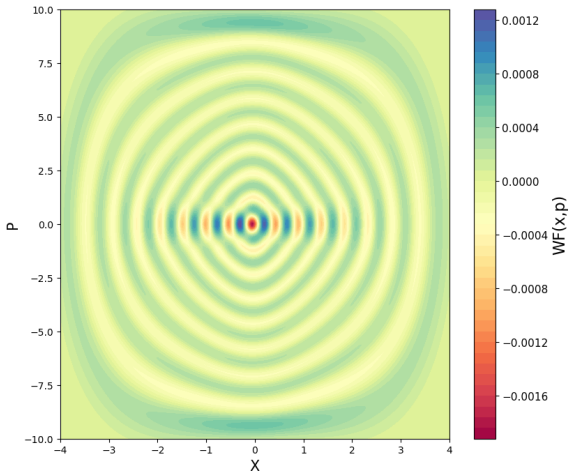

(e) WF for Asymmetric Double-Well Potential

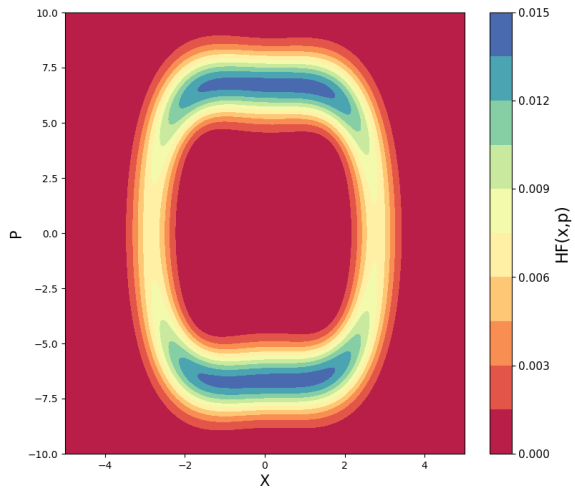

(f) HF for Asymmetric Double-Well Potential

Figure 3.7: Wigner and Husimi Functions for the ground state ($n = 15$) of the quartic oscillator for different potential configurations. Calculations were performed using $K = 1$, $\xi = 1$ and the correspondent values of B_1 and B_2 for each potential.

3.5. QUANTUM CUSP

In Chapter 2, we studied the Hamiltonian of the quartic oscillator classically and saw how the stability of the critical points for both the linear and cubic cases were equivalent. Additionally, we explored Catastrophe Theory, demonstrating that, through a series of transformations, one can transition from a general form of the quartic potential to the canonical form of the cusp catastrophe without losing generality in the behavior of the function's critical points. For this reason, when dealing with the quantum Hamiltonian detailed in Equation 3.3, we can focus on the linear case ($B_3 = 0$), which corresponds to the canonical form of the cusp catastrophe potential:

$$\hat{\mathcal{H}} \equiv \frac{\hat{H}}{\epsilon_0} = \frac{4P^2}{K} + X^4 + B_2X^2 + B_1X \ , \tag{3.18}$$

One of the pioneering works to extend the results of the Cusp Catastrophe into the quantum formalism was R. Gilmore in his 1986 paper, *Quantum Cusp* [22]. He investigated the qualitative features of a quantum-mechanical system whose potential in the classical limit undergoes a cusp catastrophe. The study encompasses several key aspects: the eigenvalue spectrum, density of states, wavefunction localization and delocalization, probability distribution, operator expectation values, and matrix elements, all analyzed as functions of the cusp control parameter values. Through this analysis, Gilmore determined the canonical features that precede and accompany the transition from the single-mode to the double-mode regime through the pitchfork bifurcation. The study exhibits the clear relationships between the qualitative properties of the quantum cusp and the canonical properties of the classical cusp catastrophe. However, this study did not establish a direct connection between the presented results and quantum phase transitions. In fact, the Quantum Cusp represents the most common type of catastrophe in one dimension that generates both first-order and second-order phase transitions [8].

As previously mentioned, the behavior of this Hamiltonian is illustrated in the phase diagram and potential shapes shown in Figure 3.8. The curve in this figure (3.8), which defines the different phases of the cusp catastrophe, allows us to depict the possible shapes the potential can take based on the values of control parameters B_1 and B_2. At points on the curve $27B_1^2 + 8B_2^3 = 0$ (the same as 2.29), and above them, the potential exhibits a single minimum. Below this curve, two minima appear which can be symmetric when $B_1 = 0$ or asymmetric with $B_1 \neq 0$.

The points labelled from (a) to (i) in the figure indicate different shapes of the potential as a function of the parameters B_1 and B_2, represented in the panels to the right of Figure 3.8. Point (a) corresponds to a pure quartic potential, with a single flat-bottomed minimum. Point (d) stands for a potential that also has a single minimum, but which is closer to a harmonic oscillator potential. Point (g) features a potential with two symmetric minima. Points (b) and (c), which lie on the curve, exhibit a single minimum with a saddle point at $X = 0$, oriented differently depending on whether B_1 is positive or negative. Points (e) and (f), located above the curve, also display a single minimum. Finally, points (h) and (i), located under the curve, have an associated potential with asymmetric double minima.

Additionally, two trajectories are drawn in Figure 3.8, one in purple and the other in orange. These trajectories represent two pathways on the B_1 and B_2 parameter space, used to study first and second-order phase transitions, respectively. In the next chapter, we will study these two phase transitions in detail and how their precursors can be identified in the quantum system.

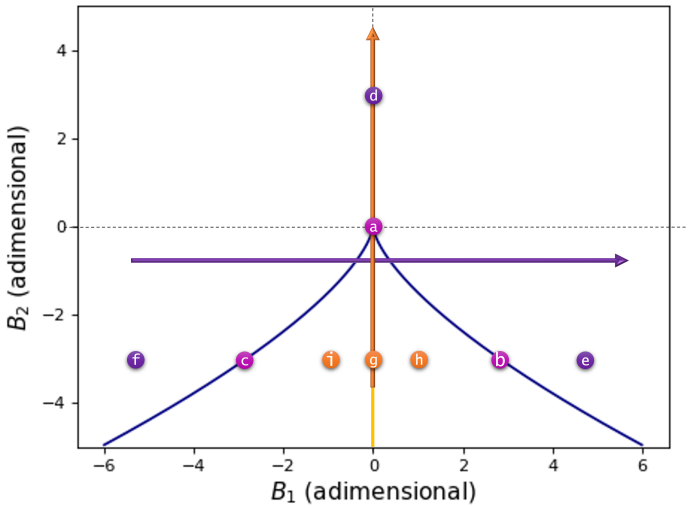

(I)

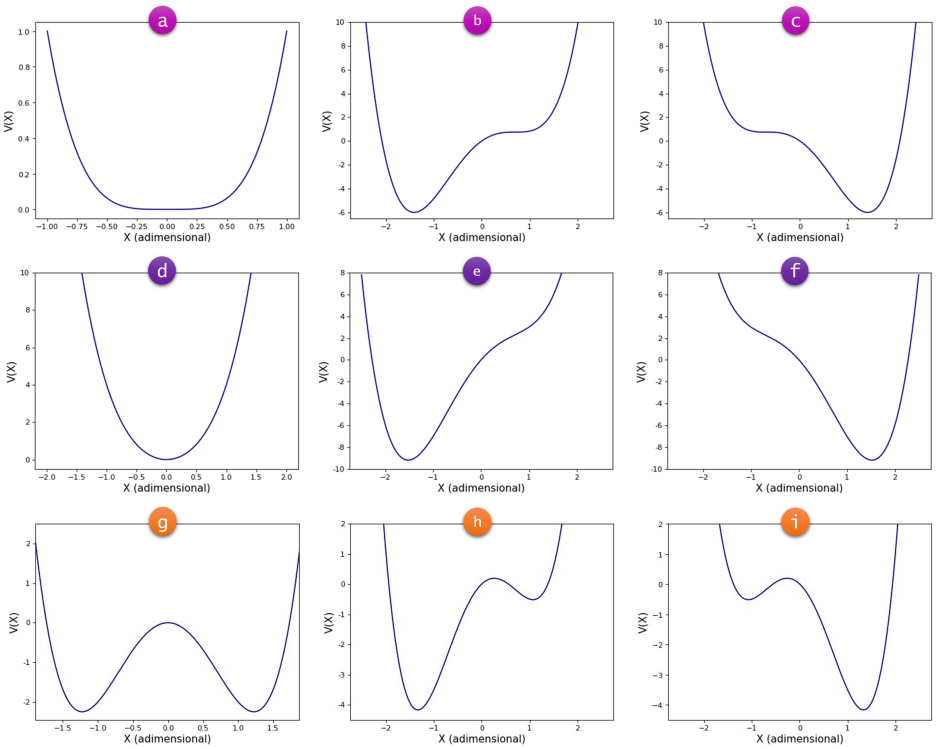

(II)

Figure 3.8: Phase diagram and potential shapes for the quantum Hamiltonian in the linear case of the cusp catastrophe. The curve delineates the transition between different potential configurations. Points (a) to (i) illustrate the potential forms at various parameter values B_1 and B_2, showing transitions from a single minimum to symmetric and asymmetric double minima. The purple and orange trajectories indicate the paths followed in the parameter space to explore first and second-order quantum phase transitions, respectively.

CHAPTER 4

Ground and Excited State Quantum Phase Transitions

Phase transitions are fundamental phenomena in physics, usually associated with abrupt changes in the macroscopic properties of a system as external parameters, such as temperature, pressure, or magnetic field, are varied. These transitions have been intensively studied in classical systems, where they are typically characterized by the occurrence of sudden changes in physical properties like magnetization, density, heat capacity, or structural order.

Phase transitions can be categorized using *Ehrenfest's classification* [35], which is based on the continuity of the free energy derivatives with respect to some thermodynamic parameter. According to this classification, phase transitions are divided into first-order and continuous phase transitions:

- *First-order phase transitions* involve a discontinuity in the first derivative of the free energy with respect to some thermodynamic variable (such as temperature or pressure). A classic example of a first-order phase transition is the melting of ice or the boiling of water. At the boiling point of water, the fluid undergoes a phase transition from liquid to gas, a process accompanied by the absorption of latent heat. This transition is characterized by a discontinuity in the first derivative of the free energy with respect to temperature, reflecting abrupt changes in entropy and volume as the system changes phases [35].
- On the other hand, second order or*continuous phase transitions*, are characterized by the continuity of the first derivative but a discontinuity in the second or higher order derivative of the free energy [35]. A well-known example of a second-order continuous phase transition is the ferromagnetic to paramagnetic transition at the Curie point [38]. At this temperature, the magnetization of a ferromagnetic material changes continuously to zero, but the magnetic susceptibility, which is the second derivative of the free energy with respect to the magnetic field, diverges. In the present work we will use either continuous or second-order phase transitions to address these cases.

As we discussed in Section 2.3.1, regarding spontaneous symmetry breaking, the concept of an **order parameter** is central to the understanding of phase transitions. The order parameter is a quantity that distinguishes between different phases. In the symmetric phase, the order parameter is typically zero, whereas in the broken-symmetry phase, it takes non-zero values. For instance, in the ferromagnetic transition, the magnetization is a custom order parameter, being zero in the high-temperature paramagnetic phase and non-zero in the low-temperature ferromagnetic phase.

Classical or thermodynamical phase transitions are marked by qualitative changes in the state of a system due to variations in external conditions. Understanding these classical transitions lays the groundwork for exploring more complex phenomena such as quantum

phase transitions. This leads us to the following question: how are quantum phase transitions identified and, more importantly, how do they occur? Here, quantum fluctuations play a crucial role, replacing thermal fluctuations.

4.1. GROUND STATE QUANTUM PHASE TRANSITIONS

Quantum phase transitions (QPTs) occur at absolute zero temperature, when quantum fluctuations, rather than thermal ones, drive the transition. Unlike classical phase transitions, which are induced by changes in temperature, pressure, or other thermodynamic parameters, QPTs are driven by changes in Hamiltonian control parameters that make the system ground state undergo abrupt changes of the system due to the variation of a , such as magnetic field, chemical pressure, or chemical composition [6]. The concept of Ground State Quantum Phase Transitions (GSQPT) is crucial in this context, as it specifically refers to the changes in the system's ground state. The study of GSQPTs was significantly advanced by the seminal works of Robert Gilmore and collaborators, who extended the understanding of phase transitions to differents quantum systems [18, 21, 23]. The GSQPTs are often referred as simply QPTs.

At zero temperature, quantum fluctuations dominate the behavior of a system. These fluctuations arise from the Heisenberg uncertainty principle [6], which ensures that certain pairs of physical properties, such as position and momentum, cannot both be precisely determined simultaneously. In the context of QPTs, these fluctuations can drive the system from one phase to another as the control parameter is varied. So, a GSQPT is marked by a change in the nature of the quantum ground state as a function of the control parameter.

A defining characteristic of Quantum Phase Transitions (QPTs) is the concept of criticality, where the system exhibits scale-invariant behavior at the quantum critical point (QCP). At this point, particularly during a second-order transition, the critical fluctuations are scale-invariant and extend throughout the entire system, leading to divergent correlation lengths and times [55, 57]. This behavior is essential for understanding the universality class of the QPT, which is determined by the symmetry of the order parameter and the dimensionality of the system. Universality implies that distinct systems with the same symmetry properties and dimensionality will display identical critical behavior in the vicinity of the QCP, regardless of the microscopic details of the systems [14, 25, 46, 50].

4.1.1. Characterization of Quantum Phase Transitions

To characterize a QPT, one typically looks at the energy spectrum of the system. A first-order quantum phase transition is identified by a discontinuity in first order derivative of the ground state energy or a discontinuity in the expectation value of an observable chosen as order parameter. Meanwhile, a second-order transition is characterized by a discontinuity in the second-order derivative of the ground state energy or in the first-order derivative of the order parameter. It is important to emphasize the discontinuities are only achieved in the large system size limit (also known as classical limit) but still clear precursors of the QPT can be found in mesoscopic systems and finite-size scaling laws derived [32].

Besides, as for classical phase transitions, QPTs can be characterized by an order parameter, which changes from zero in one phase to a non-zero value in another phase. The order parameter provides a measure of the degree of order in the system. As we mentioned in Section 2.3.1, in the quartic oscillator case, the chosen order parameter is the position expectation value

In addition to these, here, we will describe some other magnitudes that have proven useful in identifying precursors of ground state (and excited state) phase transitions.

Quantum Fidelity and Susceptibility

Quantum fidelity, between two states, a quantity of major importance in quantum computing and quantum information, is calculated as the modulus of the overlap between the states [25]. In the context of QPTs, fidelity is computed between the ground state of a system and the ground state of the same system whose control parameter(s) has(have) been slightly modified. For an in-depth review of the role of quantum fidelity in QPTs, see the comprehensive article by Gu [25], which discusses the connection between quantum fidelity, its susceptibility, and critical phenomena in various quantum systems. Assuming a single control parameter, quantum fidelity is defined as

$$\mathcal{F}(\xi, \xi + \delta\xi) = |\langle\psi_0(\xi)|\psi_0(\xi + \delta\xi)\rangle| \,, \tag{4.1}$$

where $\psi_0(\xi)$ is ground state of a system with a control parameter ξ and $\psi_0(\xi + \delta\xi)$ is the ground state for a control parameter $\xi + \delta\xi$, where $\delta\xi << \xi$. When the eigenvectors are normalized, as in our case, quantum fidelity between identical eigenvectors is unity, and it decreases as the difference between the eigenvectors used for its calculation increases. Thus, for a small value of $\delta\xi$, as the value of ξ increases, the fidelity remains close to unity until reaching the critical value of the control parameter, where even small control parameter variations produces significant changes in the system's ground state.

When there is a ground-state level crossing (i.e. a GSQPT), a sudden drop of the fidelity occurs. The overlap between two ground states at ξ and $\xi + \delta\xi$ can be defined as [25]

$$f(\xi, \xi + \delta\xi) = \langle\psi_0(\xi)|\psi_0(\xi + \delta\xi)\rangle.$$

By performing a series expansion, the overlap becomes

$$f(\xi, \xi + \delta\xi) = 1 + \delta\xi \left\langle \psi_0(\xi) \middle| \frac{\partial}{\partial\xi}\psi_0(\xi) \right\rangle + \frac{(\delta\xi)^2}{2} \left\langle \psi_0(\xi) \middle| \frac{\partial^2}{\partial\xi^2}\psi_0(\xi) \right\rangle + \cdots .$$

The fidelity, as the absolute value of the overlap, then becomes

$$|f(\xi, \xi + \delta\xi)|^2 = 1 + \delta\xi \left(\left\langle \psi_0 \middle| \frac{\partial}{\partial\xi}\psi_0 \right\rangle + \left\langle \frac{\partial}{\partial\xi}\psi_0 \middle| \psi_0 \right\rangle \right) + (\delta\xi)^2 \left(\left\langle \frac{\partial}{\partial\xi}\psi_0 \middle| \psi_0 \right\rangle \left\langle \psi_0 \middle| \frac{\partial}{\partial\xi}\psi_0 \right\rangle \right)$$
$$+ \frac{1}{2} \left\langle \psi_0 \middle| \frac{\partial^2}{\partial\xi^2}\psi_0 \right\rangle + \frac{1}{2} \left\langle \frac{\partial^2}{\partial\xi^2}\psi_0 \middle| \psi_0 \right\rangle + \cdots .$$

The linear correction must be zero for two reasons. First, due to the normalization condition

$$\left\langle \psi_0 \middle| \frac{\partial}{\partial\xi}\psi_0 \right\rangle + \left\langle \frac{\partial}{\partial\xi}\psi_0 \middle| \psi_0 \right\rangle = \frac{\partial}{\partial\xi}\langle\psi_0|\psi_0\rangle = 0.$$

Second, $|f|$ must be smaller than unity, meaning the leading term must be an even function of $\delta\xi$. Therefore,

$$\mathcal{F}(\xi, \xi + \delta\xi) = 1 - \frac{(\delta\xi)^2}{2}\mathcal{S}(\xi) + \cdots \,,$$

where $\mathcal{S}(\xi)$ denotes the quantum fidelity *susceptibility* (QFS) of the state. Thus, one way to obtain the susceptibility is

$$\mathcal{S}(\xi) = \lim_{\delta\xi \to 0} \frac{2(1 - \mathcal{F}(\xi, \xi + \delta xi))}{\delta\xi^2} \tag{4.2}$$

The QFS is the second-order term in the series expansion of the fidelity as a function of $\delta\xi$. The susceptibility is maximum at critical points and it has also been extensively used to identify QPTs.

We can also express the QFS in its *perturbative form* [25]. To understand this, let us consider the fidelity near a second-order quantum phase transition, where the ground state of the Hamiltonian is non-degenerate for a finite system. When the control parameter $\xi + \delta\xi$ is close to ξ, the ground-state wavefunction can be expanded to first order as

$$|\psi_0(\xi + \delta\xi)\rangle = |\psi_0(\xi)\rangle + \delta\xi \sum_{n\neq 0} \frac{H_I^{n0}(\xi)|\psi_n(\xi)\rangle}{E_0(\xi) - E_n(\xi)},$$

where

$$H_I^{n0} = \langle\psi_n(\xi)|H_I|\psi_0(\xi)\rangle$$

is the matrix element of the driving Hamiltonian H_I between the ground state and the excited states. Normalizing the wavefunction $|\psi_0(\xi + \delta\xi)\rangle$, the fidelity can be expanded to leading order as

$$\mathcal{F}(\xi, \xi + \delta\xi) = 1 - \delta\xi^2 \sum_{n\neq 0} \frac{|\langle\psi_n(\xi)|H_I|\psi_0(\xi)\rangle|^2}{[E_n(\xi) - E_0(\xi)]^2} + \cdots .$$

Here, the most significant contribution comes from the second-order term in the expansion, which describes the response of the fidelity to a small change in ξ.Then, this can be rewritten as the perturbation form of the QFS [25]

$$\mathcal{S}(\xi) = \sum_{n\neq 0} \frac{|\langle\psi_n(\xi)|H_I|\psi_0(\xi)\rangle|^2}{[E_n(\xi) - E_0(\xi)]^2}. \tag{4.3}$$

The QFS in this perturbative form highlights how the system's susceptibility to parameter changes is governed by the energy gap and the coupling between the ground state and the excited states. QFS is a more effective tool tan fidelity in detecting QPTs [40, 59].

In relation to the QFS, it is important to connect this concept with the *Quantum Fisher Information* (QFI), which is highly relevant in the field of Quantum Metrology [24, 40, 62]. QFI measures the sensitivity of a quantum state to changes in a parameter and is directly related to the accuracy with which this parameter can be estimated. Both QFS and QFI quantify how a quantum state changes with respect to small variations in the parameter ξ, but while QFS is concerned with the overlap between slightly different states, QFI directly quantifies the information that can be extracted about the parameter from quantum measurements [24, 40].

The relationship between QFS and QFI can be expressed as follows: for a pure quantum state $|\psi(\xi)\rangle$ [40, 49], the QFI is four times the QFS [40]

$$F_Q(\xi) = 4\,\mathcal{S}(\xi). \tag{4.4}$$

This means that, in the context of QPTs, the regions where QFS peaks (indicating significant changes in the state due to parameter variations) are also the regions where QFI is maximized. Quantum Metrology exploits this to enhance measurement precision, especially near critical points where the sensitivity, as captured by the QFI, reaches its maximum [40, 24]. Thus, the study of QFS not only deepens our understanding of QPTs but also provides valuable insights into the metrological properties of quantum systems.

Inverse Participation Ratio (IPR)

Upon diagonalizing the Hamiltonian matrix (3.13), one obtains the corresponding eigenvalues and eigenvectors in the Fock basis. These eigenvectors can be used to calculate the *Participation Ratio* (PR) [17], also referred to as the inverse participation ratio [34], which provides insight into the degree of localization of an eigenstate of the Hamiltonian in a given basis, i.e., how spread out the eigenvector is among the basis elements. A low PR value indicates a more

localized state, whereas high PR values indicate a state that mixes many basis components. The PR of a quantum state is calculated as [31, 47]

$$\mathrm{PR} = \frac{1}{\sum_i |c_i|^4}\,, \tag{4.5}$$

where c_i are the components of the state in a given basis. If the states are the quantum quartic oscillator eigenstates, being normalized, the sum $\sum_i |c_i|^2 = 1$. Thus, for a state maximally localized, with a single component different from zero, the IPR value is 1. A completely delocalized state, where all basis elements contribute equally, has a maximum IPR value, IPR = D, where D is the dimension of the basis.

This magnitude has proven to be valuable in identifying quantum phase transitions, providing insight into the localization properties of eigenstates and their behavior near critical points [2, 37, 47]. Recently, it has been demonstrated that the study of IPR characterizes excited state phase transitions [2, 37, 47], as for bases that fulfill certain characteristics, the IPR shows how eigenstates near the critical energy are particularly localized. Besides the IPR, another measure of an eigenstate's localization is the Shannon entropy of its probability distribution [31]

$$H_S = -\sum_n |\psi_n|^2 \ln |\psi_n|^2\,.$$

The Shannon entropy, H_S, quantifies the uncertainty or the information content associated with the probability distribution [48] of the quantum state [31, 41]. It vanishes ($H_S = 0$) when the probability density is concentrated at a single site, indicating a fully localized state [31]. Conversely, it attains its maximal value ($H_S = \ln N$) for delocalized states, where the probability is uniformly spread across all basis components [31].

As we can observe, the IPR and Shannon Information Entropy are closely related; both provide insight into the degree of localization of a quantum state. However, in our study, we will focus solely on the calculation and analysis of the IPR, given its direct applicability and simplicity in identifying localization phenomena in the eigenstates of the quartic oscillator.

Level Density

The *level density* is a fundamental quantity in the study of quantum systems, providing insight into the distribution of energy levels within the system's spectrum. The nature of level distribution in a system spectrum is a common tool to ascertain whether a quantum system is chaotic or integrable; in the context of the present work, as we will explain below, can be used to detect and classify Excited State Quantum Phase Transitions (ESQPTs).

Recall that, as defined in 2.4.1, level density measures the classical phase-space volume at energy E. However, as we aim to use this quantity to study the ESQPTs in our quantum system (eq. (3.3)), our classicality parameter K becomes crucial. This parameter was introduced in the kinetic term to allow recovery of the classical limit of the system for $K \to \infty$. For the classical limit of Hamiltonian of the Quantum Cusp (eq. (3.3)) that we want to study, the level density is given by

$$\nu(E) = \frac{\pi}{\sqrt{K}} \int_{-\infty}^{\infty} \frac{dX}{\sqrt{E - X^4 - B_2 X^2 - B_1 X}}. \tag{4.6}$$

Alternatively, level density can be calculated from the Hamiltonian spectrum. First, the eigenvalues corresponding to the studied Hamiltonian in each case are obtained using a diagonalization routine. From these values, a number N of energy levels, $\{E_j\}_{j=1}^{N}$, is

considered, and n equidistant values are selected within this interval, $\{\epsilon_i\}_{i=1}^{n}$. The energy level density will be calculated as

$$\rho_s(\epsilon_i) = \frac{2s+1}{E_{j+s} - E_{j-s}} \,, \tag{4.7}$$

where s is an integer number of neighboring E_j values around each ϵ_i. In this way, we obtain the density of states in each region of the energy spectrum and changes in this density or its derivative at energies of critical points can be analyzed.

4.1.2. First-Order Quantum Phase Transition

As mentioned at the end of the previous chapter, we aim to study phase transitions for the Quantum Cusp Hamiltonian in eq. (3.18). To achieve this goal, we examine the system's spectrum behavior for different values of the parameters B_1 and B_2, along the trajectories depicted in the parameter space (Figure 3.8). By following these trajectories, we will identify precursors of both first- and second-order QPTs.

Following the purple line in Figure 3.8, the parameter B_2 is held constant at $B_2 = -1$, while the parameter B_1 is varied. In Figure 4.1, we illustrate the dynamics of the energy levels (correlation energy diagram) in this case, where a first-order phase transition occurs as B_1, the control parameter in this case, is varied with a critical value at $B_1 = 0$. The variation of the linear term coefficient B_1 shifts the potential barrier between the wells when $B_2 < 0$ and make the wells asymmetric. Along this trajectory, the potential changes from being first an asymmetric function with a single minimum to having two asymmetric minima. When $B_1 = 0$, the potential displays two symmetric minima. From this point, the potential again transforms into an asymmetric function, with a configuration which is a reflection across the ordinate axes of the previously described one, initially with two minima and ultimately with a single asymmetric minimum.

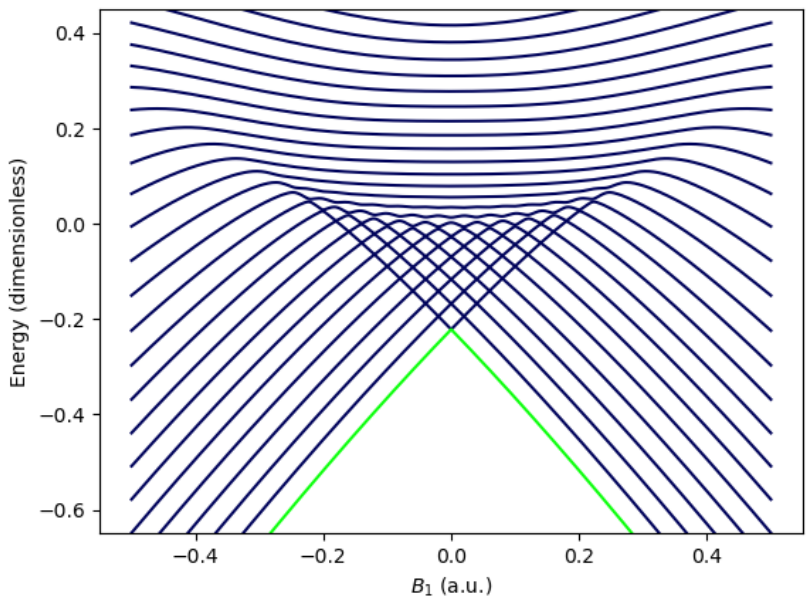

Figure 4.1: Energy level for a quartic potential Hamiltonian with a negative quadratic term ($B_2 = -1$) for different values of B_1 from -1 to 1. The calculations were performed using $K = 10000$, $\xi = \sqrt{2}$, and a basis dimension $N = 2000$.

When the potential has symmetric minima, at $B_1 = 0$, it is the typical configuration of minima coexistence that characterizes first order phase transitions. As can be seen in figure

4.1, the ground state energy changes its slope abruptly, forming a peak that forebodes a discontinuity in its first derivative, as expected for first-order phase transitions. Again, it is important to emphasize that this is due to the fact that at the critical control parameter value $B_1 = 0$ two equivalent minima coexist. When the system straddles across this point, depending on the direction, the minimum shifts from the right to the left of the origin, or vice versa.

As we mentioned earlier, if the aforementioned trajectory indicates a first-order phase transition, the first derivative of the energy with respect to the control parameter, B_1 should be discontinuous. To make this point clear, we plot the first derivative of the ground state energy with respect to B_1, dE_{gs}/dB_1, calculated numerically (Figure 4.2). The expected value of the position, $\langle X \rangle$ (Figure 4.2, right), can be considered as an order parameter for this transition, as it also exhibits an abrupt change and it is nonanalytic at the critical point ($B_1 = 0$) for the ground state.

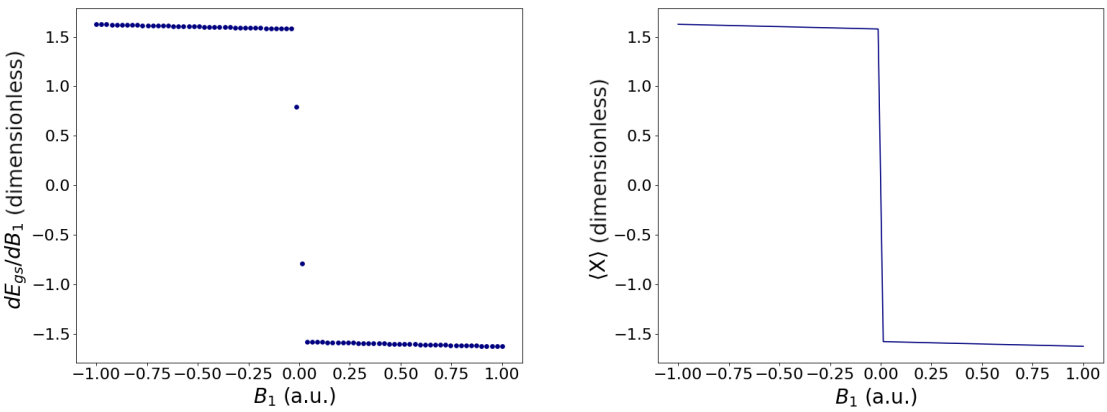

Figure 4.2: Left: Derivative of the ground state energy with respect to the control parameter B_1. Right: Expected value of the position $\langle X \rangle$ as a function of B_1. Both with $B_2 = -1$ and using $K = 10000$, $\xi = \sqrt{2}$, with a basis dimension $N = 2000$..

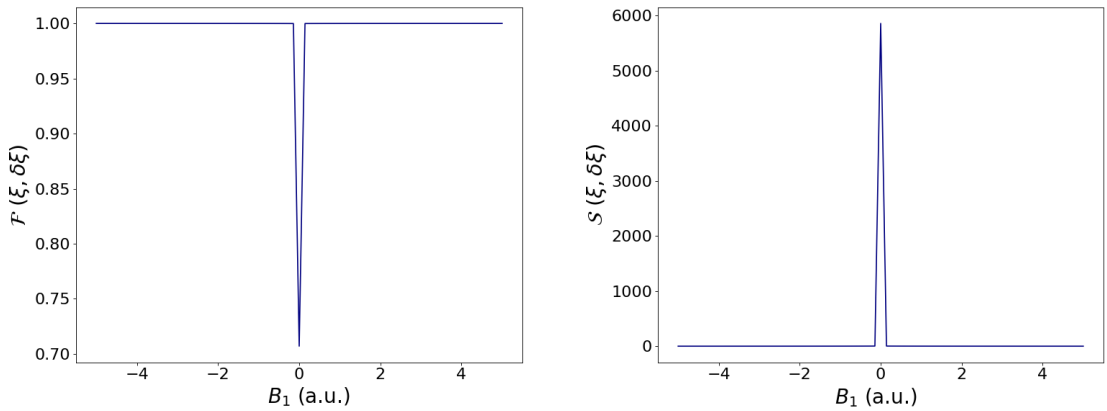

Figure 4.3: Variation of QF ($\mathcal{F}$) and QFS ($\mathcal{S}$) of the ground state with respect to B_1 with $B_2 = -1$ and $K = 10000$, $\xi = \sqrt{2}$, with a basis dimension $N = 2000$, and a perturbation $\delta B_2 = 0.001$.

Regarding quantum fidelity ($\mathcal{F}$) and QFS ($\mathcal{S}$), discussed earlier, the first-order phase transition becomes apparent when representing the variation of both quantities against the parameter B_1 (Figure 4.3). For values of $B_1 \neq 0$, the overlap between the eigenvectors of the

ground state for different, yet close, values of B_1 is nearly equal to 1. At the critical control parameter value, $B_1 = 0$, $\mathcal{F}$ shows a narrow minimum and the $\mathcal{S}$ a spike, highlighting the abrupt change undergone by both quantities.

4.1.3. Second-Order Quantum Phase Transition

The second-order phase transition occurs when the second derivative of the ground state energy of the system shows a discontinuity at a critical control parameter value. In our case, such transition takes place when we vary control parameter B_2 for $B_1 = 0$, following the path marked with an the orange line in Figure 3.8 at the critical point $B_2 = 0$. As B_2 is varied from negative to positive values, the potential transforms from a symmetric double well to a potential with a single minimum (See figure 3.8). In this particular case, where we vary B_2 with $B_1 = 0$, the Hamiltonian possesses parity symmetry, meaning it is invariant under the transformation $X \longrightarrow -X$. This parity symmetry results in the Hamiltonian being block-diagonalized into two subspaces corresponding to even and odd parity states. This symmetry has significant implications for the behavior of the system near the critical point, as the transitions in the eigenstates of the system will respect this parity symmetry. Figure 4.4 is the correlation energy diagram for Hamiltonian (3.18) for $B_1 = 0$, as a function of B_2.

When $B_2 > 0$, the potential is a symmetric double well and the energy of the ground state is negative and degenerate, whereas if $B_2 \geq 0$, the potential has a single minimum and the ground state energy is positive. It is observed that when $B_2 < 0$, not only the ground state, but also even and odd excited states are degenerate for energies below the barrier ($E = 0$). This degeneracy is broken once the energy of the system straddles the barrier energy, due to tunneling effects. Once the energy is positive, there is no possible degeneracy.

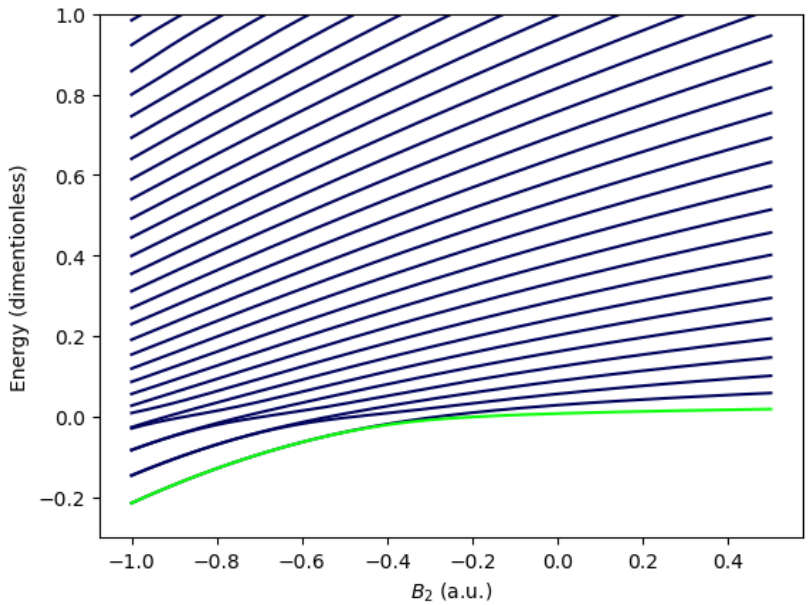

Figure 4.4: Energy spectrum of Hamiltonian (3.18) as a function of the control parameter B_2 with $B_1 = 0$. The calculations were performed using $K = 6000$, $\xi = \sqrt{2}$, and a basis dimension $N = 2000$.This plot illustrates the transformation of the potential from a symmetric double well to a single minimum potential, highlighting the energy behaviors of the ground and excited states across the transition from $B_2 < 0$ to $B_2 \geq 0$.

In the context of the parity-conserving quartic potential, with $B_1 = 0$, we examine the behavior of the second derivative of the potential with respect to B_2. We compare this second derivative, computed both analytically and numerically from the energies of the eigenstates.

Starting the analytical computation, we first set the first derivative of the potential with respect to X to zero:

$$0 = \frac{dV(X)}{dX} = 4X^3 + 2B_2X, \tag{4.8}$$

which allows us to solve for X at the critical points of the potential, yielding $X_c = \pm\sqrt{-B_2/2}$ and $X_c = 0$. When $B_2 \geq 0$, there is a minimum at $X_c = 0$. Conversely, when $B_2 < 0$, this minimum transforms into a maximum, and two minima emerge at $X = \pm\sqrt{-B_2/2}$.

Therefore, the order parameter, that in this case corresponds with the expectation value of the position, is:

$$\langle X \rangle = \begin{cases} 0 & \text{if } B_2 \geq 0, \\ \pm\sqrt{|B_2|/2} & \text{if } B_2 < 0 \end{cases} \tag{4.9}$$

After determining X_c, we substitute these critical points back into the potential function to compute its first and second derivatives with respect to B_2:

$$V'(B_2) = \begin{cases} 0 & \text{if } B_2 \geq 0 \\ -B_2/2 & \text{if } B_2 < 0 \end{cases} \tag{4.10}$$

$$V''(B_2) = \begin{cases} 0 & \text{if } B_2 \geq 0 \\ -1/2 & \text{if } B_2 < 0 \end{cases} \tag{4.11}$$

These equations demonstrate a discontinuity at $B_2 = 0$ for the second derivative.

Figure 4.5 displays the first (left) and second (right) derivatives of the energy of the ground state with respect to B_2, both calculated numerically from the energy spectrum of a system with with $B_1 = 0$ using $K = 6000$ and $\xi = \sqrt{2}$ and analytically in the classical limit. The first derivative has a clear abrupt change in slope at $B_2 = 0$, leading to the observed discontinuity in the second derivative at the critical point.

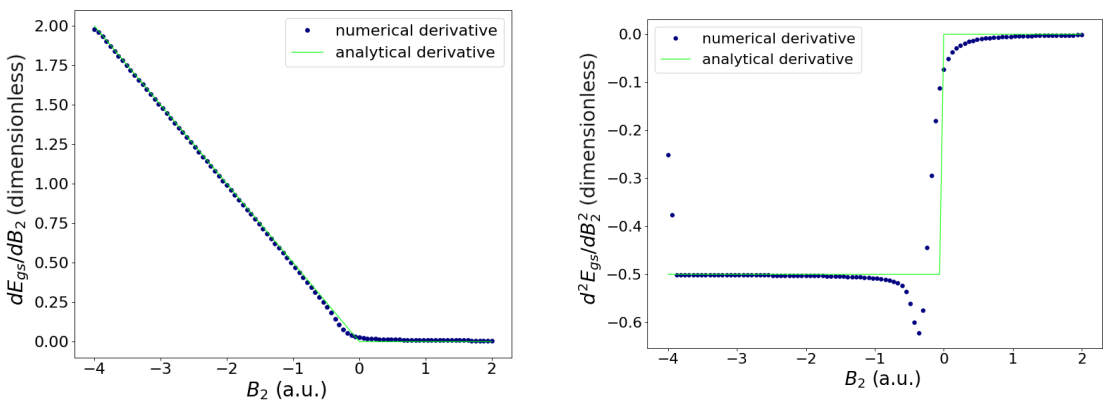

Figure 4.5: Left: First derivative of the Hamiltonian evaluated at the critical point X_c with respect to B_2 as a function of B_2, showing the change in slope at $B_2 = 0$. Right: Second derivative of the Hamiltonian (evaluated at the critical point X_c) with respect to B_2, highlighting the discontinuity at $B_2 = 0$. These derivatives are calculated both analytically and numerically using $K = 6000$, $\xi = \sqrt{2}$ with a basis dimension $N = 2000$, providing insights into the characteristics of the second-order phase transition.

In a second-order QPT, the expected value of the position, $\langle X \rangle$, can be chosen as an order parameter and it is expected to have a nonanalytic first-order derivative (See figure 4.6). This parameter exhibits an abrupt change at the critical point of the QPT, $B_2 = 0$. To calculate it, we used the expression $\langle X \rangle = \langle \psi_0 | X | \psi_0 \rangle$, where ψ_0 is the ground state wave function. Additionally, a small perturbation δB_1 was introduced in the Hamiltonian. This perturbation slightly deepens one of the potential wells, allowing the wave function to become localized in that well. This technique was necessary to independently calculate each of the curves displayed in the graph, ensuring that $\langle X \rangle$ could be computed in a controlled manner across different values of B_2. It is observed that for $B_2 < 0$, the states may be localized in one well or the other of the potential, serving as a clear example of a pitchfork bifurcation in the system as it transitions through the critical point, explained as a spontaneous symmetry breaking process (mentioned in sec. 2.3.1).

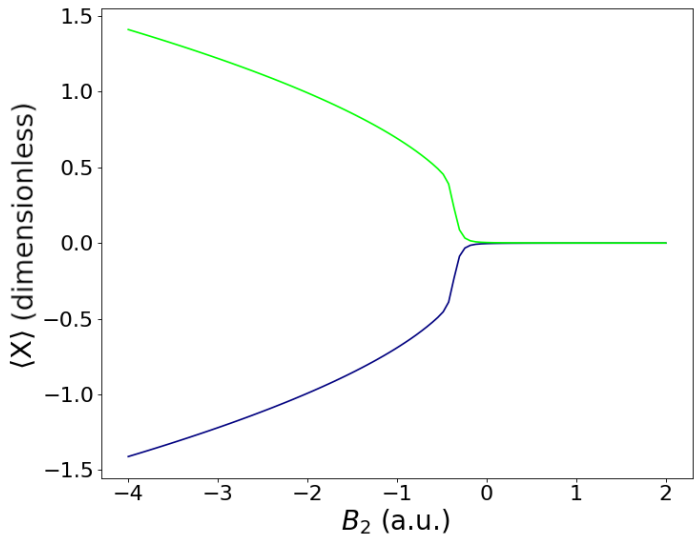

Figure 4.6: Expected value of the position $\langle X \rangle$ as the order parameter, illustrating its abrupt change at the critical point $B_2 = 0$ using $K = 6000$, $\xi = \sqrt{2}$ with a basis dimension $N = 2000$.

In order to characterize the second-order QPT, we plot quantum fidelity against B_2 (Figure 4.7, left panel), with a minimum near the critical point. When B_2 is negative and close to zero, the symmetric wells are so shallow that tunneling effects are very important or even the ground state is already above the potential barrier. In this scenario, the overlap between ground states suddenly decreases for values of B_2 where there is still a double well. This minimal overlap at the critical point reflects a significant change in the state of the system, indicating a transition from one quantum phase to another. When the parameter K is increased, the minimum at the critical point becomes deeper. This is due to the fact that increasing K reduces the energy separation between states, which enhances the tunneling effects. As K increases, the system becomes more sensitive to changes in B_2, which results in a sharper decline in quantum fidelity around the critical point. This deeper minimum signifies that the overlap between ground states is significantly reduced, indicating a stronger and more clearly defined quantum phase transition.

As expected, the QFS, S (See figure 4.7, right panel), exhibits a maximum near zero. This peak in the susceptibility is indicative of the system's heightened sensitivity to changes in B_2 at the transition, reinforcing the characterization of the origin as a critical point. Such maxima in susceptibility are key markers of second-order transitions, where the first-order

derivative of the order parameter changes discontinuously. As B_2 transitions from negative to positive, the system's behavior and its energy landscape undergo significant alterations. This dynamical change in the quantum states, particularly around $B_2 = 0$, is crucial for understanding the mechanisms driving quantum phase transitions.

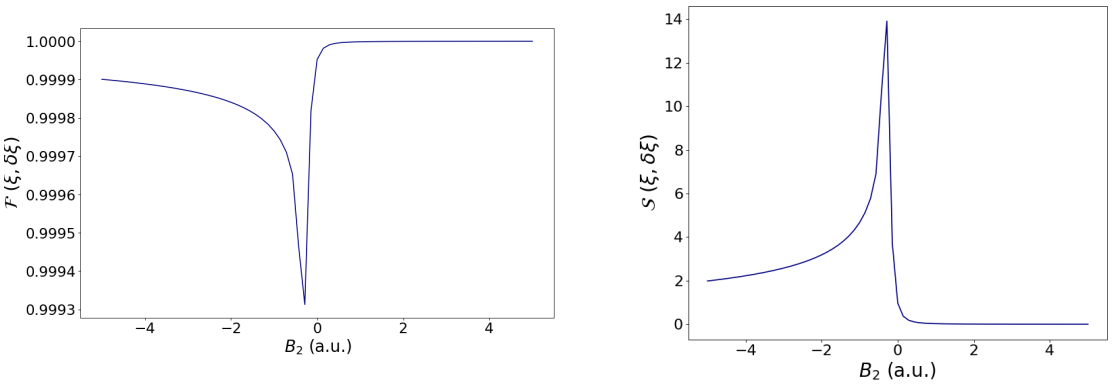

Figure 4.7: Left: QF as a function of B_2, highlighting the minimal overlap near the critical point where the phase transition occurs. Right: QFS, S, as a function of B_2, showing a peak near zero. The calculations were performed using $K = 6000$, $\xi = \sqrt{2}$, a basis dimension $N = 2000$, and with a perturbation $\delta B_2 = 0.001$.

4.2. EXCITED STATE QUANTUM PHASE TRANSITIONS

Excited State Quantum Phase Transitions (ESQPTs) are a remarkable phenomenon in quantum systems that were introduced in 2006 to extend the concept of ground state quantum phase transitions to the realm of excited states [5, 8, 36, 61, 53, 47, 37]. Recently, an excellent review article has been published on this subject [10]. These transitions reveal a critical behavior and structural changes in the excited states energy spectrum, providing deeper insights into the quantum dynamics of the system. ESQPTs are typically characterized by singularities or discontinuities in the density of states or in the level of localization of the eigenstates, such as the PR. Beyond the density of states, ESQPTs can also be probed using some of the quantities that have been employed to detect GSQPTs. The singularities occur at *critical energies*, marking the transition points where the nature of the quantum states changes abruptly.Unlike GSQPTs, ESQPTs can be accessed in two different ways: either by exciting the system at constant control parameters or by varying the control parameters while keeping the energy constant. This dual approach provides unique opportunities for probing the critical phenomena in excited states. ESQPTs and their associated nonanalyticities in the density of states are chiefly associated with the occurrence of critical points in the classical limit of the system [53].

The study of ESQPTs is crucial for understanding the full quantum phase diagram of a system, including the rich behavior that arises in its excited states. For our study of ESQPTs, given the parameters that govern the shape of the potential, three different cases within the phase space diagram are investigated. For all cases, the value of the parameter ξ is kept constant at 1, unless indicated otherwise. In the first case, the pure quartic potential is studied, with $B_1 = B_2 = 0$, resulting in a single minimum at 0. In the second case, the values $B_1 = 0$ and $B_2 = -5$ are examined, where the potential forms a double well with two symmetric minima and a potential barrier at $X = 0$. In the third and final case, $B_2 = -5$ is maintained and values of $B_1 = 1$ are assigned, resulting in an asymmetric double well. These cases are the same as those studied in the quantum potential section (3.3). Each case will be analyzed by representing and studying the level density, the energy difference between consecutive levels, and the participation ratio, as introduced in Section 4.1.1.

Additionally, the study of ESQPTs not only provides insights into the spectral properties of quantum systems but also reveals the interplay between classical and quantum dynamics. The observation of level clustering around the critical energy points underscores the critical nature of these transitions, akin to classical phase transitions, yet driven by quantum fluctuations. The intricate patterns in the participation ratio and level density elucidate how quantum states evolve and localize in the modified potential landscape, offering a profound understanding of the underlying quantum phase structure.

4.2.1. Pure Quartic Potential

As previously mentioned, in this potential, the values of B_1 and B_2 are kept at 0, resulting in the potential $V(X) = X^4$ (Figure 3.2). The shape of the pure quartic potential is similar to that of the harmonic oscillator but with a significantly flatter bottom. In this case, there is not a hint of an ESQPT, as expected due to the lack of critical points beyond the absolute minimum in the classical limit of the system. It can be observed that the anharmonicity of this potential is positive, meaning the distance between levels grows as the energy increases. This distance between levels is also represented in the left graph of Figure 4.8.

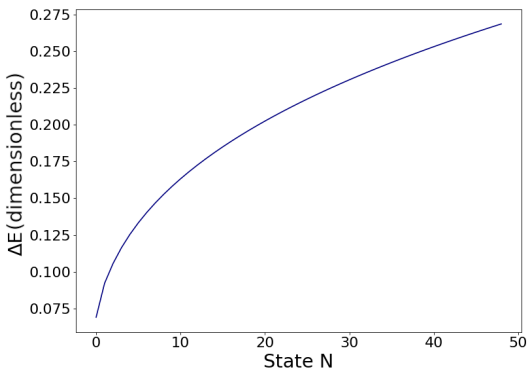

(a) Energy difference between consecutive levels for the pure quartic potential.

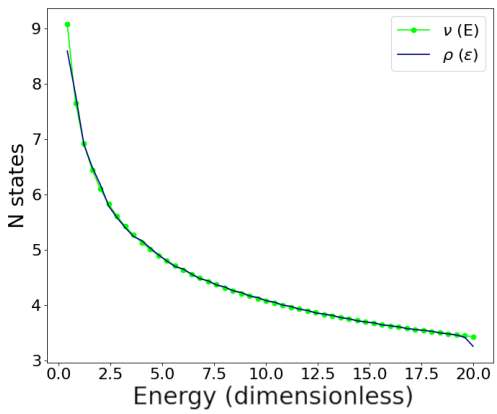

(b) Level density for the pure quartic potential.

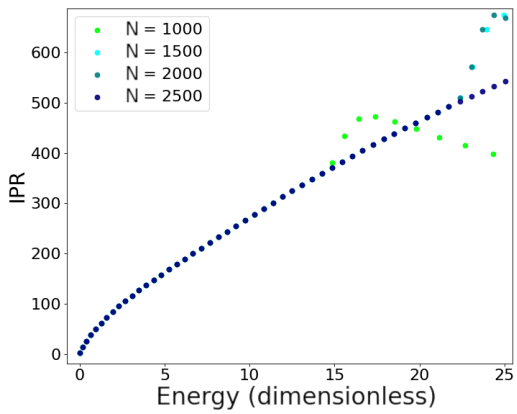

(c) IPR for different dimensions of the truncated harmonic oscillator basis.

Figure 4.8: Analysis of the pure quartic potential $V(X) = X^4$: (a) Energy difference between consecutive levels, (b) Level density estimated using Eq. (4.7) and calculated exactly via Eq. (4.6), and (c) IPR for different basis dimensions. The calculations were performed using $K = 1000$, $\xi = \sqrt{2}$, and a basis dimension $N = 2500$.

The level density, represented in the right graph of Figure 4.8, was estimated using the values obtained through Eq. (4.7) and was calculated exactly in the classical limit via Eq. (4.6). In the classical limit, with a high value of K, very good agreement between both cases is observed, as expected considering the value of K ($K = 1000$). In both representations, the level density decreases as the energy increases due to the increasing separation of the excited levels. The participation ratio is represented in Figure 4.8 (bottom graph) five different increasing dimensions of the truncated harmonic oscillator basis. In all cases, the PR increases with energy, indicating that the more excited levels involve a larger number of base states, as expected. Furthermore, as the matrix dimension increases, better convergence in the eigenfunctions is achieved, especially for higher energy levels. It is essential to note that while we previously analyzed convergence concerning the truncated basis size for energies, convergence in eigenvalues does not necessarily imply convergence in eigenvectors. By examining the PR, we gain insight into the convergence of the eigenvectors.

However, there are still some aspects to discuss regarding the behavior of the PR. At low energies, the PR value is small because the eigenstates are primarily localized around the potential minimum, where fewer harmonic oscillator basis states are required to represent the wavefunction. As energy increases, the states become more delocalized, spanning a broader region of the phase space and needing more basis states, which leads to an increase in the PR. Figure 3.2 provides a visual representation of how localized the first few states are and how they delocalize as energy increases.

It is important to highlight that, unlike in compact systems (such as the two following cases), where the PR typically reaches a maximum at intermediate energies and then decreases as energy grows further, the pure quartic potential's unbounded nature prevents such behavior. In compact systems, high-energy states often exhibit increased localization due to boundary effects or specific features of the potential, such as tunneling near the maximum in between the two wells, causing the PR to rise and then fall. In contrast, the anharmonicity of the pure quartic potential and the absence of confining boundaries allow the states to continuously spread out as energy increases, leading to a monotonic increase in the PR.

4.2.2. Symmetric Double-Well Potential

The potential used is $V(X) = X^4 - 5X^2$, with $B_1 = 0$. In Figure 4.9 (right panel), an increase in the density of levels around $E = 0$ is observed. This increase in the level density is a logarithmic divergence, as expected by analysing the integral of eq. (4.6) [53]. The left graph shows that the energy difference ΔE has a minimum near the state $n = 30$, where the ESQPT occurs ($E = 0$), allowing us to identify the critical point coinciding with the maximum of the potential [8, 53]. The participation ratio is also represented in this figure 4.9 (bottom graph) for different dimensions of the Hamiltonian matrix to analyze the convergence among eigenvectors. This participation ratio starts close to unity for the lower energy eigenstates, due to boundary effects typical for states that are localized at the edge of the Hilbert space. As energy increases, the participation ratio increases since a greater number of harmonic oscillator base states are required to describe the eigenstate. At the potential's maximum, for $E = 0$, the eigenstates closest to the critical energy of the ESQPT are very localized in the Fock basis, causing a minimum in the participation ratio at $E = 0$. This behavior can be understood by considering the classical phase space. Near the critical energy, the system's dynamics exhibit a transition between two qualitatively different behaviors. For $E < 0$, the system is classically trapped in one of the two wells, resulting in regular and periodic motion that is largely confined to the vicinity of the potential minima. These states correspond to the localized eigenstates in the quantum case, with each state requiring fewer harmonic oscillator basis elements, thus producing a low participation ratio.

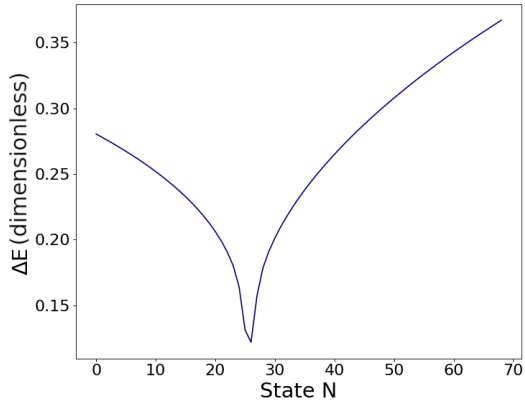

(a) Energy difference between consecutive levels for the symmetric double-well potential.

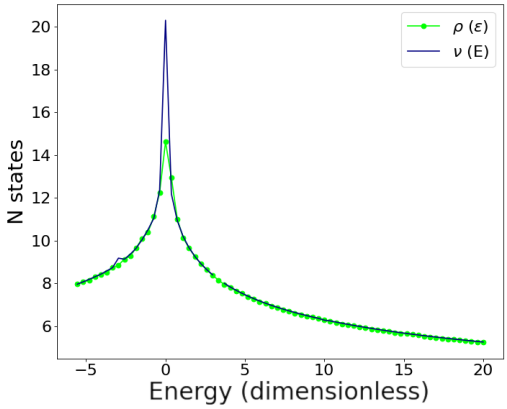

(b) Level density for the symmetric double-well potential.

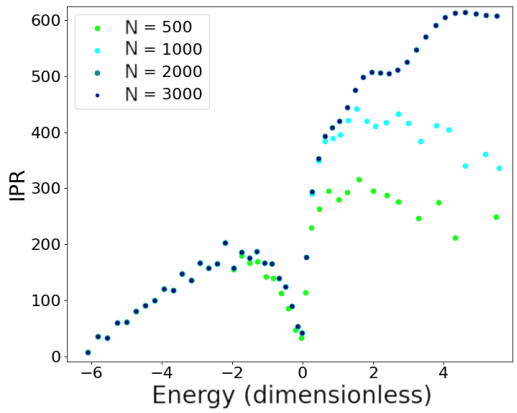

(c) Participation ratio for different dimensions of the Hamiltonian matrix.

Figure 4.9: Graphical analysis of the symmetric double-well potential $V(X) = X^4 - 5X^2$ (only parity even states are represented): (a) Energy difference ΔE between consecutive levels, identifying a minimum near the state $n = 30$ where the ESQPT occurs. (b) Level density, showing an increase around $E = 0$. (c) Participation ratio for different dimensions of the Hamiltonian matrix, highlighting a minimum in participation at $E = 0$ and an increase for $E > 0$, aiding in identifying the critical point of the ESQPT. The calculations were performed using $K = 2000$, $\xi = \sqrt{2}$, and a basis dimension $N = 3000$.

At $E = 0$, the system reaches the potential maximum, where the classical motion slows down near the separatrix that divides the two wells. This region of phase space is associated with a sharp change in the classical dynamics. Quantum mechanically, this corresponds to states becoming more localized near the barrier, as the quantum system can easily tunnel between the two wells close to this energy level. This localization is reflected in the minimum of the participation ratio at $E = 0$, as fewer Fock basis states are needed to describe the wavefunction that is confined around the separatrix.

For $E > 0$, the particle has enough energy to move over the potential barrier and explore both wells. The classical motion becomes less localized, spanning larger regions of phase space. In the quantum picture, this corresponds to more delocalized states, leading to the observed increase in the participation ratio, similar to the behavior seen in the pure quartic oscillator.

In this case, both the peak in the level density and the minimum in the energy difference between consecutive levels, as well as in the participation ratio, allow us to locate the critical point of the ESQPTs as in both cases the density of levels undergoes an abrupt change as the excitation energy increases [53].

To gain deeper insights into the behavior at the critical point of the Excited State Quantum Phase Transition (ESQPT), we have focused on analyzing the most localized state as indicated by the lowest Participation Ratio (IPR). This approach allows us to explore the Husimi and Wigner functions, which provide a visual representation of the quantum state in phase space. The most localized state identified is $n = 28$ with an energy $E = -0.017$. Figure 4.10 illustrates these functions for the specified state. As observed in this figure, the state is localized at the origin, directly at the saddle point (the maximum of the potential). Given the energy level at which it occurs, just below the potential maximum, this localization is likely attributed to quantum tunneling effects. The tunneling process facilitates the state's concentration at this critical juncture, reflecting significant alterations in the system's quantum dynamics at the transition threshold of the ESQPT.

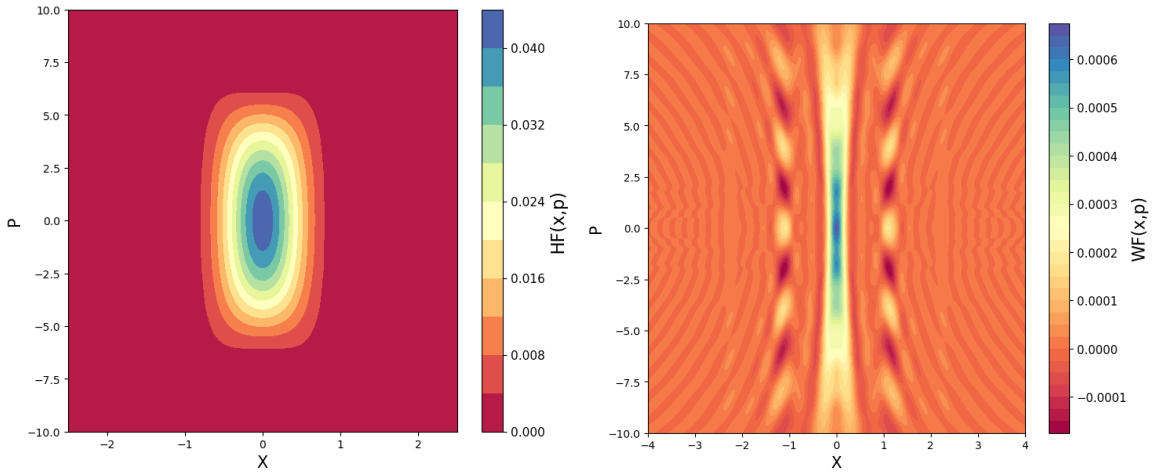

Figure 4.10: Quantum phase space analysis for the most localized state ($n = 28$, $E = -0.017$) in the symmetric double-well potential, shown using Husimi (left) and Wigner (right) functions. These visualizations illustrate the state's behavior at the critical point of the ESQPT. The calculations were performed using $K = 2000$, $\xi = \sqrt{2}$, and a basis dimension $N = 2500$.

4.2.3. Asymmetric Double-Well Potential

The potential used to analyze this case is $V(X) = X^4 - 5X^2 + X$, presented in Figure 3.4.

The level density, as shown in Figure 4.11 (right graph), increases dramatically at the height where the local minimum well appears and reaches a maximum at the potential barrier, $E = 0$, similar to the symmetric double-well case. This behavior indicates the presence of the critical point of the ESQPT. However, in this asymmetric case, two distinct types of ESQPTs occur, each of a different nature [53]. On the one hand, there is a stepwise increase in the density of states as the energy crosses the critical energy, leading to a sudden change in the spectral structure. On the other hand, we observe a logarithmic divergence at $E = 0$, corresponding to the critical point at the top of the potential barrier. This divergence is analogous to what we previously discussed in the symmetric double-well case. The distinction between these two behaviors can be explained by the presence of an asymmetric potential, which breaks the parity symmetry, resulting in two separate critical points for the ESQPTs [53]. The energy difference between levels, shown in Figure 4.11 (right graph), decreases initially as it approaches the height of the local minimum. Once this well appears, the energy

difference starts alternating as the differences are calculated between states from one well or the other. The amplitude of these oscillations increases as the value of B_1 decreases. A minimum in ΔE close to $n = 60$ and a peak in level density at $E = 0$ identifies the critical point of the ESQPT at the top of the potential barrier.

In Figure 4.11 (bottom), the participation ratio is also presented for different dimensions of the truncated Fock basis to analyze convergence among eigenfunctions. As in the previous cases, states at lower energies have a lower Participation Ratio (PR) due to a boundary effect, and the PR increases with excitation energy. As the second well appears, this trend is observed again. The states belonging to the deeper well follow the trend observed in the symmetric double-well case. Similarly, the states belonging to the second minimum follow a similar trend with lower PR values. Again, at the critical point at $E = 0$, both branches of points merge into a PR minimum, and the PR increases for positive energies with similar results to those of the pure quartic oscillator, increasing the participation ratio with the energy of the states.

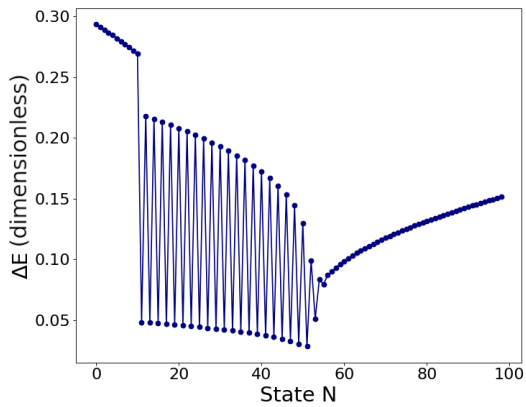

(a) Energy difference between levels

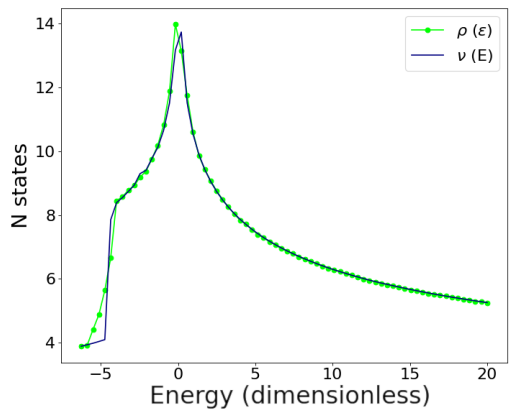

(b) Level density near the critical point

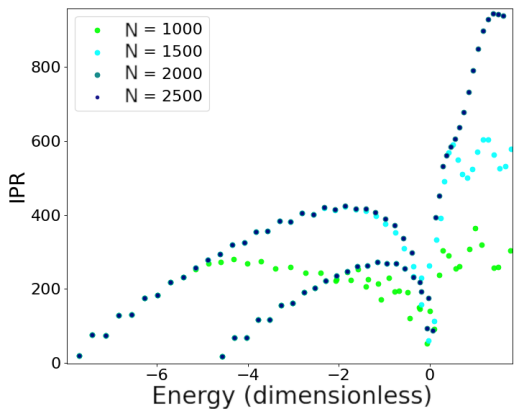

(c) Participation ratio showing trends in localization

Figure 4.11: Graphs showing the energy differences, level density, and participation ratio for the asymmetric double-well potential, highlighting critical behavior near the ESQPT. The calculations were performed using $K = 2000$, $\xi = \sqrt{2}$, and a basis dimension $N = 2500$.

For this asymmetric case, we have focused on the quantum phase space analysis for the most localized state at $n = 54$ with an energy $E = 0.054$, as well. The Husimi and Wigner functions provide insightful visualizations of how asymmetry in the potential influences

the quantum behavior near the critical point of an excited state quantum phase transition (ESQPT). Figure 4.12 illustrates these functions for the specified state. As shown in the figure, unlike in the symmetric case, the state here is not localized at the origin but is slightly shifted towards the right well, which in this scenario is the shallower one. Additionally, this state is positioned right at the potential's maximum. This localization pattern is also observed in Figure 3.4. Therefore, we can think that the state's distribution is influenced more by the potential landscape rather than tunneling dynamics.

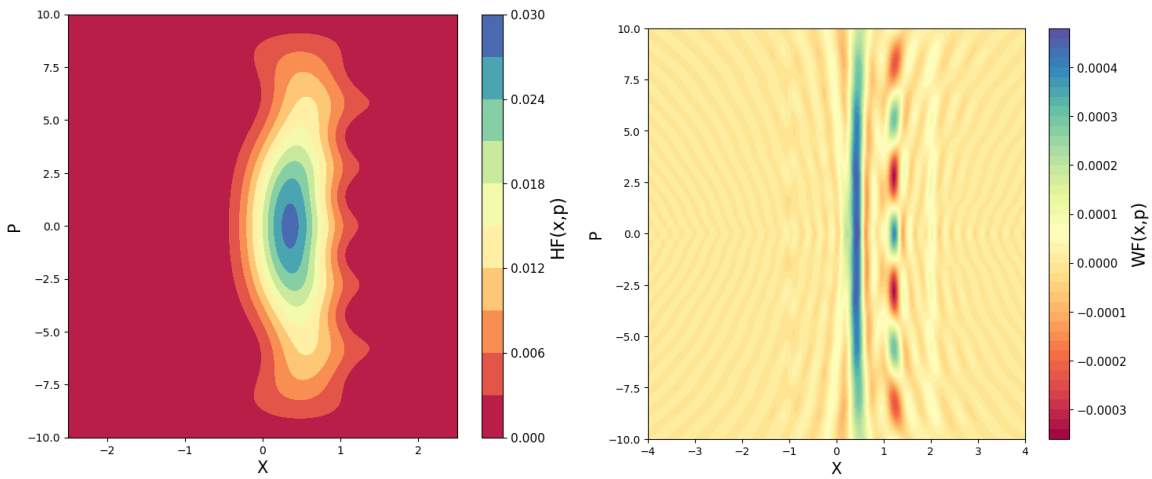

Figure 4.12: Quantum phase space analysis for the most localized state ($n = 54$, $E = 0.054$) in the asymmetric double-well potential. The left panel displays the Husimi function and the right panel shows the Wigner function, both highlighting the effects of the potential's asymmetry on the quantum phase space at the critical point of the ESQPT. The calculations were performed using $K = 2000$, $\xi = \sqrt{2}$, and a basis dimension $N = 2500$.

CHAPTER 5

Conclusions

The concluding chapter of this master's thesis, "Quantum Cusp Catastrophe in a Generalized Quartic Potential," encapsulates the core findings and the broader implications of the research conducted. In this work, we have conducted a comprehensive study of the Quantum Cusp Catastrophe (QCC) within the framework of a generalized quartic potential. Our investigation has bridged the gap between classical catastrophe theory and quantum mechanics, providing insights into the behavior of quantum systems near critical points.

We began by exploring the classical aspect of the Cusp Catastrophe (CCC), using the generalized quartic potential as our model. The classical analysis laid a solid foundation for understanding the underlying dynamics of the system, including the identification of critical points and their stability for the two studied cases (cubic and linear cases). We concluded that the behavior of the critical points and their stability is equivalent for both cases. Additionally, thanks to Catastrophe Theory and its mathematical formulation, we demonstrated that through change of variables and transformations, our generalized potential can be rewritten in the canonical form of the Cusp Catastrophe, which coincides with our studied linear case. For purely pedagogical reasons, this is significant because it means we could use the cubic case to study the critical points and their stability, as the equations for this case are simpler, and then transform the potential into the canonical form of the Cusp Catastrophe.

Transitioning to the quantum domain, we focused on the Quantum Cusp Catastrophe (QCC) and its relationship with Quantum Phase Transitions (QPTs). The study meticulously analyzed how small perturbations in the system's parameters could induce significant and sudden changes in its state configuration, a hallmark of quantum phase transitions. This investigation employed a combination of analytical techniques and numerical simulations to map out the quantum potential landscape, revealing the underlying structures that govern the behavior of quantum systems near cusp catastrophes. We discovered that the system exhibits both first-order and second-order QPTs by studying the system along two trajectories in the parameter space, each being a function of the corresponding control parameter. Furthermore, we delved into the phase space representations of the system using Wigner and Husimi functions. These quasi-probability distributions provided a deeper understanding of the quantum phase space and its correspondence with the classical phase space. The Wigner function, despite its potential negativity, offered valuable information about the localization of quantum states, while the Husimi function, being always positive, closely mirrored the classical phase space distribution.

One of the pivotal components of this thesis was the comprehensive analysis of the quartic oscillator, both classical and quantum. This anharmonic oscillator served as a versatile model to probe various physical phenomena, such as bifurcations and spontaneous symmetry breaking. The study demonstrated that the quartic potential, whether in its pure form or modified to include symmetric and asymmetric double wells, provides a robust framework for exploring the rich tapestry of quantum and classical dynamics. The research highlighted how

the anharmonic nature of the quartic potential influences the system's behavior, particularly in relation to energy levels and states. We investigated the pure quartic potential, the symmetric double-well potential, and the asymmetric double-well potential, each offering unique insights into the nature of Excited State Quantum Phase Transitions (ESQPTs). To achieve this, we brought our quantum system to the semiclassical limit. By examining the level density, energy differences, and participation ratios, we uncovered critical phenomena occurring in energy states with $E = 0$ for the symmetric and asymmetric cases, while the pure quartic potential did not exhibit critical behavior. These results extended the concept of phase transitions beyond the ground state.

In conclusion, this research has significantly advanced our understanding of the Quantum Cusp Catastrophe and its implications for quantum phase transitions. The insights gained from this study not only deepen our knowledge of fundamental quantum mechanics but also provide a platform for exploring more complex systems and phenomena. Future research could build on this foundation by exploring more complex potential forms and their implications for quantum dynamics, with potential applications in various fields such as quantum computing, nuclear physics, and quantum chemistry.

Bibliography

[1] Thomas Ayral, Pauline Besserve, Denis Lacroix, and Edgar Andres Ruiz Guzman. Quantum computing with and for many-body physics. *The European Physical Journal A*, 59, 10 2023.

[2] Ignacio Baena, Pedro Perez-Fernandez, Manuela Rodríguez-Gallardo, and J. Arias. Entropies and ipr as markers for a phase transition in a two-level model for atom–diatomic molecule coexistence. *Entropy*, 24:113, 01 2022.

[3] Aron J. Beekman, Louk Rademaker, and Jasper van Wezel. An introduction to spontaneous symmetry breaking. *SciPost Phys. Lect. Notes*, page 11, 2019.

[4] Giuliano Benenti, Giulio Casati, Davide Rossini, and Giuliano Strini. *Principles of Quantum Computation and Information*. WORLD SCIENTIFIC, 2018.

[5] M.A. Caprio, P. Cejnar, and F. Iachello. Excited state quantum phase transitions in many-body systems. *Ann. of Phys.*, 323(5):1106–1135, 2008.

[6] Angelo Carollo, Davide Valenti, and Bernardo Spagnolo. Geometry of quantum phase transitions. *Physics Reports*, 838:1–72, 2020. Geometry of quantum phase transitions.

[7] William Case. Wigner functions and weyl transforms for pedestrians. *American Journal of Physics - AMER J PHYS*, 76, 10 2008.

[8] P. Cejnar and P. Stransky. Impact of quantum phase transitions on excited-level dynamics. *Phys. Rev. E*, 78, 2008.

[9] Pavel Cejnar and Jan Jolie. Quantum phase transitions in the interacting boson model. *Prog. in Part. and Nucl. Phys.*, 62(1):210–256, 2009.

[10] Pavel Cejnar, Pavel Stránský, Michal Macek, and Michal Kloc. Excited-state quantum phase transitions. *Journal of Physics A: Mathematical and Theoretical*, 54(13):133001, mar 2021.

[11] Sunney I. Chan and David Stelman. Some energy levels and matrix elements of the quartic oscillator. *J. Molec. Spectrosc.*, 10(1):278 – 299, 1963.

[12] Ding-Geng Chen, Feng Lin, Xinguang Chen, Wan Tang, and Harriet Kitzman. Cusp catastrophe model a nonlinear model for health outcomes in nursing research. *Nursing research*, 63:211–220, 05 2014.

[13] Claude Cohen-Tannoudji, Bernard Diu, and Franck Laloë. *Quantum mechanics; 1st ed.* Wiley, New York, NY, 1977. Trans. of : Mécanique quantique. Paris : Hermann, 1973.

[14] Mucio A. Continentino. Quantum scaling in many-body systems. *Physics Reports*, 239(3):179–213, 1994.

[15] Avik Dutt, Trisha Nath, Sayan Kar, and Rajesh Parwani. Splitting of degenerate states in one-dimensional quantum mechanics. *European Physical Journal Plus*, 127:28, 03 2012.

[16] Rishab Dutta, Delmar G. A. Cabral, Ningyi Lyu, Nam P. Vu, Yuchen Wang, Brandon Allen, Xiaohan Dan, Rodrigo G. Cortiñas, Pouya Khazaei, Max Schäfer, Alejandro C.

C. d. Albornoz, Scott E. Smart, Scott Nie, Michel H. Devoret, David A. Mazziotti, Prineha Narang, Chen Wang, James D. Whitfield, Angela K. Wilson, Heidi P. Hendrickson, Daniel A. Lidar, Francisco Pérez-Bernal, Lea F. Santos, Sabre Kais, Eitan Geva, and Victor S. Batista. Simulating chemistry on bosonic quantum devices. *Journal of Chemical Theory and Computation*, 20(15):6426–6441, 2024. PMID: 39068594.

[17] Ferdinand Evers and Alexander D. Mirlin. Anderson transitions. *Rev. Mod. Phys.*, 80:1355–1417, Oct 2008.

[18] Da Hsuan Feng, Robert Gilmore, and S. R. Deans. Phase transitions and the geometric properties of the interacting boson model. *Phys. Rev. C*, 23:1254–1258, 1981.

[19] Richard P. Feynman. Simulating physics with computers. *Int. J. Theor. Phys.*, 21:467–488, 1982.

[20] R. Gilmore. *Catastrophe Theory for Scientists and Engineers*. Dover books on advanced mathematics. Dover Publications, 1993.

[21] R. Gilmore and D.H. Feng. Phase transitions in nuclear matter described by pseudospin hamiltonians. *Nuclear Physics A*, 301(2):189–204, 1978.

[22] R. Gilmore, S. Kais, and R.D. Levine. Quantum Cusp. *Phys. Rev. A*, 34:2442–2452, 1986.

[23] Robert Gilmore and Da Hsuan Feng. Ground state phase transitions in multilevel extensions of the lipkin-meshkov-glick model. *Physics Letters B*, 85(2):155–158, 1979.

[24] Vittorio Giovannetti, Seth Lloyd, and Lorenzo Maccone. Advances in quantum metrology. *Phys. Rev. Lett.*, 96, 02 2011.

[25] SHI-JIAN GU. Fidelity approach to quantum phase transitions. *International Journal of Modern Physics B*, 24, 09 2010.

[26] M. C. Gutzwiller. *Chaos in Classical and Quantum Mechanics*. Springer, New York, 1990.

[27] Fritz Haake. *Quantum Signatures of Chaos*. Springer-Verlag, Berlin, 1991.

[28] Jinyu Han, Xiangde Zhu, Jian-Feng Zhang, Shu Cai, Jing Guo, Yazhou Zhou, Jinyu Zhao, Pengyu Wang, Lihua Wang, Xiangjun Wei, Sheng Jiang, Ke Yang, Yu Gong, Yanchun Li, Xiaodong Li, Lixin Cao, Mingliang Tian, Qi Wu, Tao Xiang, and Liling Sun. Superconducting-insulating quantum phase transition associated with valence change in compressed perovskite bismuth-oxides. 05 2023.

[29] Charles R. Harris, K. Jarrod Millman, Stéfan J. van der Walt, Ralf Gommers, Pauli Virtanen, David Cournapeau, Eric Wieser, Julian Taylor, Sebastian Berg, Nathaniel J. Smith, Robert Kern, Matti Picus, Stephan Hoyer, Marten H. van Kerkwijk, Matthew Brett, Allan Haldane, Jaime Fernández del Río, Mark Wiebe, Pearu Peterson, Pierre Gérard-Marchant, Kevin Sheppard, Tyler Reddy, Warren Weckesser, Hameer Abbasi, Christoph Gohlke, and Travis E. Oliphant. Array programming with NumPy. *Nature*, 585(7825):357–362, September 2020.

[30] Song He, S. Das Sarma, and X. C. Xie. Quantized hall effect and quantum phase transitions in coupled two-layer electron systems. *Phys. Rev. B*, 47:4394–4412, Feb 1993.

[31] Yu He, Shiqi Xia, Dimitris G. Angelakis, Daohong Song, Zhigang Chen, and Daniel Leykam. Persistent homology analysis of a generalized aubry-andré-harper model. *Physical Review B*, 106(5), August 2022.

[32] F. Iachello and N. V. Zamfir. Quantum phase transitions in mesoscopic systems. *Phys. Rev. Lett.*, 92:212501, May 2004.

[33] E. M. Izhikevich. Equilibrium. *Scholarpedia*, 2(10):2014, 2007.

[34] Felix M. Izrailev. Simple models of quantum chaos: Spectrum and eigenfunctions. *Physics Reports*, 196(5):299–392, 1990.

[35] Gregg Jaeger. The ehrenfest classification of phase transitions: Introduction and evolution. *Archive for History of Exact Sciences*, 53:51–81, 05 1998.

[36] J. Khalouf-Rivera, J. Gamito, F. Pérez-Bernal, J. M. Arias, and P. Pérez-Fernández. Excited-state quantum phase transitions in the anharmonic lipkin-meshkov-glick model: Dynamical aspects. *Phys. Rev. E*, 107:064134, Jun 2023.

[37] Jamil Khalouf-Rivera, Miguel Carvajal, and Francisco Perez-Bernal. Quantum fidelity susceptibility in excited state quantum phase transitions: application to the bending spectra of nonrigid molecules. *SciPost Physics*, 12(1), January 2022.

[38] J. Kiss, L. Szarka, and E. Prácser. Second-order magnetic phase transition in the earth. *Geophysical Research Letters*, 32(24), 2005.

[39] Y. Kuznetsov. *Elements of Applied Bifurcation Theory*. Applied Mathematical Sciences. Springer New York, 2004.

[40] Jing Liu, Heng-Na Xiong, Fei Song, and Xiaoguang Wang. Fidelity susceptibility and quantum Fisher information for density operators with arbitrary ranks. *Physica A Statistical Mechanics and its Applications*, 410:167–173, September 2014.

[41] B. Mirbach and H.J. Korsch. A generalized entropy measuring quantum localization. *Annals of Physics*, 265(1):80–97, 1998.

[42] Michael A. Nielsen and Isaac L. Chuang. *Quantum Computation and Quantum Information: 10th Anniversary Edition*. Cambridge University Press, 2010.

[43] Marcel Novaes. Wigner and husimi functions in the double-well potential. *Journal of Optics B: Quantum and Semiclassical Optics*, 5:S342, 06 2003.

[44] Frank Olver, Daniel Lozier, Ronald Boisvert, and Charles Clark. *The NIST Handbook of Mathematical Functions*. Cambridge University Press, New York, NY, 2010.

[45] J. Barkley Rosser. The rise and fall of catastrophe theory applications in economics: Was the baby thrown out with the bathwater? *Journal of Economic Dynamics and Control*, 31(10):3255–3280, 2007.

[46] S. Sachdev. *Quantum phase transitions*. Cambridge University Press, Cambridge, second ed. edition, 2011.

[47] Lea F. Santos and Francisco Pérez-Bernal. Structure of eigenstates and quench dynamics at an excited-state quantum phase transition. *Physical Review A*, 92(5), November 2015.

[48] C. E. Shannon. A mathematical theory of communication. *The Bell System Technical Journal*, 27(3):379–423, 1948.

[49] Hans-J rgen Sommers and Karol Zyczkowski. Bures volume of the set of mixed quantum states. *Journal of Physics A: Mathematical and General*, 36(39):10083–10100, September 2003.

[50] T. Spencer, N. Alon, J. Bourgain, A. Connes, M. Gromov, and V. Milman. *Universality, Phase Transitions and Statistical Mechanics*, pages 839–858. Birkhäuser Basel, Basel, 2010.

[51] I. Stewart. Elementary catastrophe theory. *IEEE Transactions on Circuits and Systems*, 30(8):578–586, 1983.

[52] S.H. Strogatz. *Nonlinear Dynamics and Chaos: With Applications to Physics, Biology, Chemistry, and Engineering*. CRC Press, 2018.

[53] Pavel Stránský and Pavel Cejnar. Classification of excited-state quantum phase transitions for arbitrary number of degrees of freedom. *Physics Letters A*, 380(34):2637–2643, August 2016.

[54] René Thom. *Structural Stability and Morphogenesis: An Outline of a General Theory of Models*. Addison-Wesley, Reading, MA, 1989.

[55] Emanuele G. Dalla Torre. Scale invariant distribution functions in quantum systems with few degrees of freedom. *SciPost Phys.*, 5:023, 2018.

[56] Pauli Virtanen, Ralf Gommers, Travis E. Oliphant, Matt Haberland, Tyler Reddy, David Cournapeau, Evgeni Burovski, Pearu Peterson, Warren Weckesser, Jonathan Bright, Stéfan J. van der Walt, Matthew Brett, Joshua Wilson, K. Jarrod Millman, Nikolay Mayorov, Andrew R. J. Nelson, Eric Jones, Robert Kern, Eric Larson, C J Carey, İlhan Polat, Yu Feng, Eric W. Moore, Jake VanderPlas, Denis Laxalde, Josef Perktold, Robert Cimrman, Ian Henriksen, E. A. Quintero, Charles R. Harris, Anne M. Archibald, Antônio H. Ribeiro, Fabian Pedregosa, Paul van Mulbregt, and SciPy 1.0 Contributors. SciPy 1.0: Fundamental Algorithms for Scientific Computing in Python. *Nature Methods*, 17:261–272, 2020.

[57] Matthias Vojta. Quantum phase transitions. *Reports on Progress in Physics*, 66(12):2069, nov 2003.

[58] E. Wigner. On the quantum correction for thermodynamic equilibrium. *Phys. Rev.*, 40:749–759, 11 1931.

[59] Wen-Long You, Ying-Wai Li, and Shi-Jian Gu. Fidelity, dynamic structure factor, and susceptibility in critical phenomena. *Phys. Rev. E*, 76:022101, Aug 2007.

[60] E. C. Zeeman. Catastrophe theory. In Werner Güttinger and Horst Eikemeier, editors, *Structural Stability in Physics*, pages 12–22, Berlin, Heidelberg, 1979. Springer Berlin Heidelberg.

[61] Xin H. H. Zhang and Harold U. Baranger. Driven-dissipative phase transition in a kerr oscillator: From semiclassical $\mathcal{PT}$ symmetry to quantum fluctuations. *Phys. Rev. A*, 103:033711, Mar 2021.

[62] Y. M. Zhang, X. W. Li, W. Yang, and G. R. Jin. Quantum fisher information of entangled coherent states in the presence of photon loss. *Phys. Rev. A*, 88:043832, Oct 2013.

APPENDICES

APPENDIX A

Non-dimensionalization of the Classical Quartic Hamiltonian

To nondimensionalize the classical Hamiltonian

$$\mathbf{H}_i(x, P) = \frac{1}{2m}P^2 + A_4x^4 + A_ix^i + A_2x^2 \ . \tag{A.1}$$

where $i = 1, 3$, we introduce dimensionless variables q and p defined by

$$q = \frac{x}{x_0}, \quad p = \frac{P}{P_0},$$

where x_0 and P_0 are characteristic scales of position and momentum, respectively. Substituting $x = x_0q$ and $P = P_0p$ into the Hamiltonian (A.1), we have

$$\mathbf{H}_i(x, P) = \frac{1}{2m}(P_0p)^2 + A_4(x_0q)^4 + A_i(x_0q)^i + A_2(x_0q)^2 \ . \tag{A.2}$$

Expanding and simplifying each term, the Hamiltonian becomes

$$\mathbf{H}_i = \frac{P_0^2}{2m}p^2 + A_4x_0^4q^4 + A_ix_0^iq^i + A_2x_0^2q^2. \tag{A.3}$$

To proceed, we define an energy scale $E_0 = A_4x_0^4$ and factor out E_0 from the Hamiltonian,

$$\mathbf{H}_i = E_0\left(\frac{P_0^2}{2mE_0}p^2 + q^4 + \frac{A_ix_0^i}{E_0}q^i + \frac{A_2x_0^2}{E_0}q^2\right). \tag{A.4}$$

We aim for the coefficient of p^2 in the dimensionless Hamiltonian to be $\frac{1}{2}$. To achieve this, we set,

$$\frac{P_0^2}{2mH_0} = \frac{1}{2}, \tag{A.5}$$

and solving for P_0, we find the characteristic momentum scale:

$$P_0 = \sqrt{mH_0}. \tag{A.6}$$

The dimensionless constants a_j are determined by

$$a_j = \frac{A_j x_0^j}{E_0}.$$

for $j = 1, 2, 3$. Substituting these expressions back into the Hamiltonian and dividing by the energy scale, we get the dimensionless Hamiltonian

$$H_i(q, p) = \frac{\mathbf{H}_i}{E_0} = \frac{1}{2}p^2 + q^4 + a_i q^i + a_2 q^2 \,. \tag{A.7}$$

By choosing appropriate scaling factors x_0 and P_0, we have successfully nondimensionalized the original Hamiltonian. The scales are related by

$$x_0 = \left(\frac{E_0}{A_4}\right)^{1/4},$$

and:

$$P_0 = \sqrt{mE_0}.$$

APPENDIX B

Excited Level Density for Classical Quartic Oscillator

To demonstrate that the level density $\nu(E)$ for the Hamiltonian $H = \frac{\hat{H}}{\epsilon_0} = \frac{p^2}{2} + x^4 + ax^2 + bx$ is given by

$$\nu(E) \propto \int_{-\infty}^{\infty} \frac{dx}{\sqrt{E - x^4 - ax^2 - bx}},$$

we start from the definition of the level density:

$$\nu(E) = \frac{1}{2\pi} \int_{-\infty}^{\infty} dp \int_{-\infty}^{\infty} dx\, \delta(E - H(p, x)),$$

where $H(p, x)$ is the Hamiltonian of the system. The Hamiltonian for the quartic oscillator is

$$H(p, x) = \frac{p^2}{2} + x^4 + ax^2 + bx\ .$$

First, we note that the Dirac delta function $\delta(E - H(p, x))$ imposes the condition that $E = H(p, x)$

$$\delta(E - H(p, x)) = \delta\left(E - \left(\frac{p^2}{2} + x^4 + ax^2 + bx\right)\right)\ .$$

To proceed, we integrate over the momentum p. We solve the equation $E = \frac{p^2}{2} + x^4 + ax^2 + bx$ for p

$$\frac{p^2}{2} = E - (x^4 + ax^2 + bx)\ ,$$

$$p^2 = 2\left(E - (x^4 + ax^2 + bx)\right)\ ,$$

$$p = \pm\sqrt{2\left(E - (x^4 + ax^2 + bx)\right)}\ .$$

Using the composition property of the Dirac delta function $\delta(g(p)) = \sum_i \frac{\delta(p - p_i)}{|g'(p_i)|}$, where p_i are the roots of $g(p)$, the Dirac delta function can be expressed as

$$\delta\left(E-(\frac{p^2}{2}+x^4+ax^2+bx)\right)=\frac{\left[\delta\left(p-\sqrt{2(E-x^4-ax^2-bx)}\right)+\delta\left(p+\sqrt{2(E-x^4-ax^2-bx)}\right)\right]}{2\sqrt{2(E-x^4-ax^2-bx)}}\,,$$

where we have used that the derivative with respect to p is:

$$\frac{d}{dp}\left(p^2-2(E-x^4-ax^2-bx)\right)=2p\ ,$$

and the absolute value of the derivative, at the roots $p_\pm=\pm\sqrt{2(E-x^4-ax^2-bx)}$, is:

$$|2p_\pm|=2\sqrt{2(E-x^4-ax^2-bx)}.$$

Integrating over p, we get:

$$\int_{-\infty}^{\infty}dp\,\delta\left(E-(\frac{p^2}{2}+x^4+ax^2+bx)\right)=\frac{1}{\sqrt{2(E-x^4-ax^2-bx)}}.$$

Thus, the level density $\nu(E)$ becomes:

$$\nu(E)=\frac{1}{2\pi}\int_{-\infty}^{\infty}dx\,\frac{1}{\sqrt{2(E-x^4-ax^2-bx)}}.$$

Simplifying the constant factor $\frac{1}{\sqrt{2}}$ into the proportionality constant, we obtain:

$$\nu(E)\propto\int_{-\infty}^{\infty}\frac{dx}{\sqrt{E-x^4-ax^2-bx}}.$$

APPENDIX C

Second Quantization Transformation

The Hamiltonian $\hat{\mathcal{H}}$ is given by:

$$\hat{\mathcal{H}} = \frac{4P^2}{K} + X^4 + B_3X^3 + B_2X^2 + B_1X$$

We aim to rewrite this Hamiltonian using the second quantization formalism. To perform this transformation, we start by considering the dimensionless form of the Harmonic Oscillator Hamiltonian:

$$\hat{\mathcal{H}}_{HO} = \frac{\hat{H}_{HO}}{\hbar\omega} = -\frac{d^2}{2dy^2} + \frac{1}{2}y^2 \,, \tag{C.1}$$

where the unitless coordinate is $y = x/\lambda_0'$ and the natural length unit is $\lambda_0' = \left(\frac{\hbar}{m\omega}\right)^{\frac{1}{2}}$. The creation and annihilation operators, whose action on the HO basis elements is $a|n\rangle = \sqrt{n}|n-1\rangle$ and $a^\dagger|n\rangle = \sqrt{n+1}|n+1\rangle$, are defined as

$$a^\dagger = \frac{1}{\sqrt{2}}\left(y - \frac{d}{dy}\right) \,, \quad a = \frac{1}{\sqrt{2}}\left(y + \frac{d}{dy}\right) \,, \tag{C.2}$$

The introduction of these operators transforms the HO Hamiltonian to second quantization

$$\hat{\mathcal{H}}_{HO} = \frac{\hat{H}_{HO}}{\hbar\omega} = \hat{n} + \frac{1}{2} \tag{C.3}$$

To do the same with the quartic potential Hamiltonian, we know that $X = \frac{x}{\lambda_0}$ and $y = \frac{x}{\lambda_0'}$, thus, $X = \xi y$, with $\xi = \frac{\lambda_0'}{\lambda_0}$. Therefore, we can write the expressions for the coordinate and momentum, X and P, of our Hamiltonian $\hat{\mathcal{H}}$ as:

$$X = \frac{\xi}{\sqrt{2}}(a^\dagger + a) \tag{C.4}$$

$$P = \frac{-i}{\xi\sqrt{2}}(a - a^\dagger) \tag{C.5}$$

First, we substitute P into $\frac{4P^2}{K}$:

$$
\begin{aligned}
\frac{4P^2}{K} &= \frac{4}{K}\left(\frac{i}{\xi\sqrt{2}}(a-a^\dagger)\right)^2 \\
&= \frac{4}{K}\cdot\frac{-1}{2\xi^2}(a-a^\dagger)^2 \\
&= \frac{-2}{K\xi^2}(a-a^\dagger)^2
\end{aligned} \tag{C.6}
$$

Now, we calculate $(a-a^\dagger)^2$:

$$
\begin{aligned}
(a-a^\dagger)^2 &= a^2 - aa^\dagger - a^\dagger a + a^{\dagger 2} \\
&= a^2 - (a^\dagger a + 1) - a^\dagger a + a^{\dagger 2} \\
&= a^2 - 2a^\dagger a - 1 + a^{\dagger 2}
\end{aligned} \tag{C.7}
$$

where we have used the commutation relation $[a, a^\dagger] = aa^\dagger - a^\dagger a = 1$. Therefore:

$$
\frac{4P^2}{K} = \frac{-2}{K\xi^2}(a^2 + a^{\dagger 2} - 2a^\dagger a - 1) \tag{C.8}
$$

Next, we substitute X (eq (C.4)) into X^4, X^3, X^2. Starting with X^2:

$$
X^2 = \left(\frac{\xi}{\sqrt{2}}(a^\dagger + a)\right)^2 = \frac{\xi^2}{2}(a^\dagger + a)^2 \tag{C.9}
$$

Calculating $(a^\dagger + a)^2$ we have:

$$
\begin{aligned}
(a^\dagger + a)^2 &= a^{\dagger 2} + aa^\dagger + a^\dagger a + a^2 \\
&= a^{\dagger 2} + a^2 + 2a^\dagger a + 1
\end{aligned} \tag{C.10}
$$

where we have used the commutation relation. Substituting in the previous equation, we get:

$$
X^2 = \frac{\xi^2}{2}(a^{\dagger 2} + a^2 + 2a^\dagger a + 1) \tag{C.11}
$$

Continuing with X^3:

$$
X^3 = \frac{\xi^3}{2\sqrt{2}}(a^\dagger + a)^3 \tag{C.12}
$$

Calculating $(a^\dagger + a)^3$:

$$
\begin{aligned}
(a^\dagger + a)^3 &= (a^\dagger + a)(a^\dagger + a)^2 \\
&= (a^\dagger + a)(a^{\dagger 2} + a^2 + 2a^\dagger a + 1) \\
&= a^{\dagger 3} + a^\dagger a^2 + 2a^{\dagger 2} a + a^\dagger + a a^{\dagger 2} + a^3 + 2(a^\dagger a + 1)a + a \\
&= a^{\dagger 3} + 3a^{\dagger 2} a + 3a^\dagger + a^3 + 3a^\dagger a^2 + 3a
\end{aligned} \tag{C.13}
$$

where we have used the commutation relation to arrive at $aa^{\dagger 2} = a^{\dagger 2}a + 2a^\dagger$. Substituting:

$$
X^3 = \frac{\xi^3}{2\sqrt{2}}(a^{\dagger 3} + 3a^{\dagger 2} a + 3a^\dagger + a^3 + 3a^\dagger a^2 + 3a) \tag{C.14}
$$

Finally, for X^4:

$$
X^4 = \left(\frac{\xi}{\sqrt{2}}(a^\dagger + a)\right)^4 = \frac{\xi^4}{4}(a^\dagger + a)^4 \tag{C.15}
$$

Calculating $(a^\dagger + a)^4$:

$$
\begin{aligned}
(a^\dagger + a)^4 &= (a^\dagger + a)(a^\dagger + a)^3 \\
&= (a^\dagger + a)(a^{\dagger 3} + 3a^{\dagger 2} a + 3a^\dagger + a^3 + 3a^\dagger a^2 + 3a) \\
&= a^{\dagger 4} + 4a^{\dagger 3} a + 6a^{\dagger 2} + 4a^\dagger a^3 + 6a^{\dagger 2} a^2 + 12a^\dagger a + a^4 + 6a^2 + 3
\end{aligned} \tag{C.16}
$$

where we have again used the commutation relation. Substituting:

$$
X^4 = \frac{\xi^4}{4}(a^{\dagger 4} + 4a^{\dagger 3} a + 6a^{\dagger 2} + 4a^\dagger a^3 + 6a^{\dagger 2} a^2 + 12a^\dagger a + a^4 + 6a^2 + 3) \tag{C.17}
$$

Therefore, the transformed Hamiltonian is:

$$
\begin{aligned}
\hat{\mathcal{H}} = &\frac{-2}{K\xi^2}(a^2 + a^{\dagger 2} - 2a^\dagger a - 1) \\
&+ \frac{\xi^4}{4}(a^{\dagger 4} + 4a^{\dagger 3} a + 6a^{\dagger 2} + 4a^\dagger a^3 + 6a^{\dagger 2} a^2 + 12a^\dagger a + a^4 + 6a^2 + 3) \\
&+ B_3 \frac{\xi^3}{2\sqrt{2}}(a^{\dagger 3} + 3a^{\dagger 2} a + 3a^\dagger + a^3 + 3a^\dagger a^2 + 3a) \\
&+ B_2 \frac{\xi^2}{2}(a^{\dagger 2} + a^2 + 2a^\dagger a + 1) \\
&+ B_1 \frac{\xi}{\sqrt{2}}(a^\dagger + a)
\end{aligned} \tag{C.18}
$$

Defining $a^\dagger a = \hat{n}$ and reorganizing according to how the creation and annihilation operators act on the harmonic oscillator (HO) basis elements, we can write it as:

$$
\begin{aligned}
\hat{\mathcal{H}} = &\left(\frac{2}{K\xi^2} + \frac{3\xi^4}{4} + \frac{B_2\xi^2}{2}\right) + \left(\frac{4}{K\xi^2} + 3\xi^4 + B_2\xi^2\right)\hat{n} + \frac{3\xi^4}{2}a^{\dagger 2}a^2 \\
&+ \left(\frac{B_1\xi}{\sqrt{2}} + \frac{3B_3\xi^3}{2\sqrt{2}}\right)(a^\dagger + a) + \frac{B_3\xi^3}{2\sqrt{2}}(3a^{\dagger 2}a + 3a^\dagger a^2) \\
&+ \left(\frac{-4K^{-1}\xi^{-2} + 3\xi^4 + B_2\xi^2}{2}\right)(a^{\dagger 2} + a^2) + \xi^4(a^\dagger a^3 + a^{\dagger 3}a) \\
&+ \frac{B_3\xi^3}{2\sqrt{2}}(a^{\dagger 3} + a^3) \\
&+ \frac{\xi^4}{4}(a^{\dagger 4} + a^4)
\end{aligned}
\tag{C.19}
$$

where the zero-point energy is $E_0 = \frac{2}{K\xi^2} + \frac{3\xi^4}{4} + \frac{B_2\xi^2}{2}$.

APPENDIX D
Methodology

D.1. CONVERGENCE

In the computational approach to quantum mechanics, particularly in systems where the exact analytical solution is not feasible, numerical methods play a crucial role. One such method involves the iterative adjustment of the Hamiltonian's matrix dimension to ensure the accuracy and stability of the calculated eigenvalues and eigenvectors. The `convergence` function, delineated in Listing F.2, is pivotal in this process. The `convergence` function is designed to find the eigenvalues and eigenvectors of the Hamiltonian matrix for the quartic oscillator under study. The function parameters are as follows:

- **M**: Initial number of states considered in the truncated Harmonic Oscillator basis. This is also the desired number of state that we want to converge.
- **B1, B2, B3**: Coefficients that define the anharmonicity of the quartic oscillator potential. These coefficients adjust the shape of the potential in the Hamiltonian.
- **k**: The unitless parameter that scales the kinetic term in the Hamiltonian to allow recovery of the classical limit of the system for large values.
- **xi**: Unitless ratio of the length scale of the oscillators (HO and quartic).
- **deltaN**: Step size for increasing the basis dimension, which is crucial for refining the accuracy of the eigenvalues and eigenvectors.
- **deltaE**: Energy convergence threshold that determines when the iterative process can be stopped.

The function operates by initially setting the matrix dimension to M and iteratively diagonalizing the Hamiltonian matrix. After each diagonalization, it compares the eigenvalues obtained in the current iteration with those from the previous iteration. This comparison is based on the absolute differences between the eigenvalues, and if the maximum difference among them is less than the specified convergence threshold deltaE, the process is deemed to have converged. If the eigenvalues have not yet converged, indicated by a maximum difference exceeding deltaE, the matrix dimension is incremented by deltaN and the process repeats. This iterative adjustment and checking continue until convergence is achieved, ensuring that the eigenvalues and eigenvectors are computed with sufficient accuracy to be reliable for further physical interpretation or computational analysis.

The function finally returns the converged eigenvalues, eigenvectors, and the final number of basis states, which provides essential information for understanding the quantum properties of the system, such as the energy spectrum and the spatial characteristics of the quantum states.

The diagonalization of the Hamiltonian matrix is crucial for determining the eigenvalues and eigenvectors that describe the energy levels and state functions of the quantum system. This step is accomplished using the function `np.linalg.eigh` from NumPy's linear algebra

library [29]. This function is specifically designed to handle Hermitian or real symmetric matrices, which are typical of Hamiltonian matrices in quantum mechanics due to their inherent properties ensuring real eigenvalues and orthogonal eigenvectors. The `np.linalg.eigh` function computes all eigenvalues and, optionally, the eigenvectors of a Hermitian or real symmetric matrix. It is more efficient than the more general `np.linalg.eig` function because it leverages the properties of symmetric matrices to optimize computation [29]. This function returns two objects: an array of eigenvalues in ascending order and the matrix of eigenvectors. Each column of the output matrix represents an eigenvector corresponding to the eigenvalue at the same index.

D.2. WAVE FUNCTION CALCULATION

The wave functions of the harmonic oscillator are expressed as:

$$\langle y|n\rangle = \psi_n(y) = \frac{1}{\sqrt{2^n n!}}\pi^{-\frac{1}{4}}H_n(y)e^{-\frac{y^2}{2}}, \tag{D.1}$$

where $H_n(y)$ are the Hermite polynomials. Knowing that we can transform this to the coordinates of the quartic oscillator as $X = \xi y$, we express the wave functions of the states as:

$$\hat{\mathcal{H}}\Psi(X) = \epsilon\Psi(X), \quad \Psi(X) = \sum_{i=1}^{N} c_i\psi_i(X), \tag{D.2}$$

where ϵ and c_i are the eigenvalues and eigenvectors resulting form the diagonalization of the Hamiltonian matrix, respectively, and $\psi_i(X)$ are the wave functions in the harmonic oscillator basis. To calculate these wave functions, we prepared codes that compute the wave functions of the quartic oscillator based on the harmonic oscillator basis.

The wave functions of the harmonic oscillator were computed using two different methods: using the `scipy.special` Hermite polynomials [56], and using the recurrence form of the Hermite polynomials, which is:

$$H_n(x) = 2xH_{n-1}(x) - 2(n-1)H_{n-2}(x). \tag{D.3}$$

The `scipy.special` module calculates the Hermite polynomials as the physicist's Hermite polynomial, defined by:

$$H_n(x) = (-1)^n e^{x^2}\frac{d^n}{dx^n}e^{-x^2}. \tag{D.4}$$

This definition ensures that the polynomials are computed accurately and efficiently up to the desired order. In any case, using both methods, we obtained good results.

Once the wave functions in the harmonic oscillator basis were obtained, we calculated the wave functions of the quartic oscillator as the summation of the product between the eigenvectors and the harmonic oscillator wave functions, given by:

$$\Psi(X) = \sum_{i=1}^{N} c_i\psi_i(X). \tag{D.5}$$

This approach ensures accurate and efficient computation of the wave functions for the quartic oscillator system.

APPENDIX E

Comparison with other studies

E.1. RESULTS FOR PURE QUARTIC OSCILLATOR

In this appendix we compare the results obtained in our calculations with those published in [11] for a pure quartic potential with $K = 1$ and $\xi = \sqrt{2}$, achieving perfect agreement for eigenvalues and eigenvectors as well as for the matrix elements of X and X^2. For this potential, the values of B_1, B_2, and B_3 are kept at 0, resulting in the potential $V(X) = X^4$ (potential *a* from Figure 3.8).

E.1.1. Eigenvalues and Eigenvectors

Table E.1: Even eigenvalues and eigenvectors of the pure quartic oscillator with parameters $K = 1$ and $\xi = \sqrt{2}$.

n	0	2	4	6	8
ϵ	2.671945	18.787182	40.977234	95.559975	159.765668
c_0	-0.978561	-0.161188	0.103561	0.058251	0.036051
c_2	0.203003	-0.729475	0.431617	0.325739	0.240256
c_4	-0.027734	0.566372	0.158688	0.277124	0.326994
c_6	-0.011664	-0.314844	-0.483998	-0.287208	-0.136661
c_8	0.014161	0.139885	0.519217	0.000617	-0.175488
c_{10}	-0.009017	-0.045055	-0.411898	0.275841	0.274386
c_{12}	0.004312	0.002997	0.272512	-0.422875	-0.160624
c_{14}	-0.001475	0.010788	-0.154347	0.442384	-0.045904
c_{16}	0.000132	-0.011956	0.072669	-0.380891	0.237231
c_{18}	0.000335	0.008871	-0.024308	0.286208	-0.357736
c_{20}	-0.000389	-0.005309	0.000032	-0.191400	0.397970
c_{22}	0.000295	0.002588	0.009369	0.113441	-0.374840
c_{24}	-0.000179	-0.000902	-0.010870	-0.057460	0.313936
c_{26}	0.000089	0.000033	0.008964	0.021788	-0.238678
c_{28}	-0.000031	0.000313	-0.006158	-0.001875	0.165701
c_{30}	0.000001	-0.000374	0.003628	-0.007286	-0.104307
c_{32}	0.000011	0.000311	-0.001776	0.009951	0.057925
c_{34}	-0.000013	-0.000214	0.000607	-0.009234	-0.026140
c_{36}	0.000011	0.000125	0.000024	0.007153	0.006524
c_{38}	-0.000007	-0.000060	-0.000294	-0.004857	0.004027

Table E.2: Odd eigenvalues and eigenvectors of the pure quartic oscillator with $K = 1$ and $\xi = \sqrt{2}$.

n	1	3	5	7	9
ϵ	9.574576	29.342920	53.517346	80.883398	110.825574
c_1	0.894848	-0.334124	-0.219659	0.142581	0.096911
c_3	0.417611	-0.468103	-0.413279	0.372992	0.314181
c_5	-0.152170	0.596065	0.119513	0.067846	0.188929
c_7	0.036247	-0.458956	0.259727	-0.300794	-0.256828
c_9	0.004446	0.281161	-0.455418	0.202589	0.017260
c_{11}	-0.013241	-0.143071	0.473002	0.040692	0.201194
c_{13}	0.011116	0.057221	-0.390269	-0.263146	-0.250212
c_{15}	-0.006831	-0.012397	0.276068	0.390652	0.145237
c_{17}	0.003337	-0.006497	-0.170973	-0.419074	0.031999
c_{19}	-0.001180	0.011491	0.091439	0.377128	-0.203359
c_{21}	0.000097	-0.010329	-0.039217	-0.299647	0.322487
c_{23}	0.000316	0.007272	0.009297	0.214391	-0.375627
c_{25}	-0.000383	-0.004299	0.005100	-0.138381	0.371012
c_{27}	0.000309	0.002095	-0.010041	0.079189	-0.326922
c_{29}	-0.000203	-0.000719	0.010017	-0.037914	0.262827
c_{31}	0.000111	-0.000006	-0.007921	0.012120	-0.194514
c_{33}	-0.000048	0.000306	0.005386	0.001979	0.132401
c_{35}	0.000011	-0.000364	-0.003185	-0.008177	-0.081833
c_{37}	0.000007	0.000310	0.001575	0.009617	0.044294
c_{39}	-0.000013	-0.000222	-0.000546	-0.008593	-0.018819

E.1.2. Matrix Elements of $\langle X \rangle_{n,n'}$ and $\langle X^2 \rangle_{n,n'}$

Table E.3: Matrix elements of $\langle X \rangle_{n,n'}$ for the pure quartic oscillator with $K = 1$ and $\xi = \sqrt{2}$.

$n' \backslash n$	0	2	4	6	8
1	-0.756967	0.925211	-0.046804	0.002163	0.000098
3	-0.040899	1.056952	-1.162350	0.056062	0.002541
5	-0.001923	0.051879	-1.251621	1.329768	0.062890
7	0.000088	-0.002371	0.059678	-1.399705	-1.463294
9	0.000004	-0.000107	0.002689	-0.065798	-1.521802
11	0.000000	0.000005	-0.000120	0.002940	0.070935
13	0.000000	0.000000	-0.000005	0.000131	0.003152
15	0.000000	0.000000	0.000000	-0.000006	-0.000139
17	0.000000	0.000000	0.000000	0.000000	0.000006
19	0.000000	0.000000	0.000000	0.000000	0.000000

Table E.4: Matrix elements of $\langle X^2 \rangle_{n,n'}$ for the pure quartic oscillator with $K = 1$ and $\xi = \sqrt{2}$.

$n' \backslash n$	0	2	4	6	8
0	0.574675	-0.743682	-0.085380	-0.006611	-0.000434
2	-0.743682	1.975861	1.336926	0.133569	0.009672
4	-0.085380	1.336926	2.923372	1.813339	0.173101
6	-0.006611	0.133569	1.813339	3.734943	2.232293
8	-0.000434	0.009672	0.173101	2.232293	4.466116
10	0.000026	-0.000609	-0.012183	-0.208087	-2.614573
12	0.000001	-0.000035	-0.000753	-0.014405	-0.240168
14	0.000000	0.000002	0.000043	0.000879	0.016445
16	0.000000	0.000000	-0.000002	-0.000050	-0.000995
18	0.000000	0.000000	0.000000	0.000003	0.000057

APPENDIX F

Codes

This appendix contains selected snippets of the code used for the numerical calculations and simulations presented in this work. The codes are integral to demonstrating the practical application of the theoretical models discussed and provide a transparent view of the computational methods employed.

For comprehensive insights into the numerical methods and the complete set of codes used, the reader is encouraged to visit the GitHub repository dedicated to this project. The repository contains a Jupyter Notebook with all scripts and detailed documentation necessary to reproduce the results and to facilitate further exploration based on the work conducted in this thesis.

The repository can be accessed at:

https://github.com/campamarin/
Master-Thesis-The-Quantum-Cusp-Catastrophe-in-a-Generalized-Quartic-Potential.git

All codes are documented and organized to support future modifications and extensions by other researchers interested in advancing this area of study.

F.1. HAMILTONIAN

Listing F.1: Function to calculate the Hamiltonian

```
def hamiltonian_matrix(N, B1, B2, B3, k, xi):
    """
    Generates the Hamiltonian matrix for a given set of parameters.

    Inputs:
    N: number of energy levels
    B1: first-order anharmonicity coefficient
    B2: second-order anharmonicity coefficient
    B3: third-order anharmonicity coefficient
    k: unitless parameter in the kinetic term (default 1)
    xi: unitless oscillator length (default 1)

    Returns:
    Sub-diagonal Hamiltonian matrix of shape (N, N)
    """

    # Initialize the matrix with zeros
    H = np.zeros((N, N))

    n = np.arange(N)

    # Calculate the main diagonal
    cte1 = 4 / k  * xi ** -2 + 3 * xi ** 4 + B2 * xi ** 2
    cte2 = 1.5 * xi ** 4 * n * (n - 1)
```

```
    diag0 = cte1 * n + cte2 + (4 / k * xi ** -2 + 1.5 * xi ** 4 + B2 * xi ** 2) / 2

    # Calculate the first subdiagonal
    cte3 = B1 * xi + 1.5 * B3 * xi ** 3
    cte4 = 3 * xi ** 3 * B3 / np.sqrt(8)
    diag1 =  np.sqrt(2) * np.sqrt(n[1:]) * cte3 + cte4 * (n[1:] - 1) * np.sqrt(n[1:])

    # Calculate the second subdiagonal
    ct5 = -2 / k * xi ** -2 + 1.5 * xi ** 4 + B2 * xi ** 2 / 2
    ct6 = xi ** 4 * (n[2:] - 2) * np.sqrt(n[2:] * (n[2:] - 1))
    diag2 = np.sqrt(n[2:] * (n[2:] - 1)) * ct5 + ct6

    # Calculate the third subdiagona
    diag3 = (xi ** 3 * B3 * np.sqrt(n[3:] * (n[3:] - 1) * (n[3:] - 2))) / np.sqrt(8)

    # Calculate the fourth subdiagonal
    diag4 = 0.25 * xi ** 4 * np.sqrt(n[4:] * (n[4:] - 1) * (n[4:] - 2) * (n[4:] - 3))

    # Assign the calculated values to the matrix
    np.fill_diagonal(H, diag0)
    np.fill_diagonal(H[1:,:], diag1)
    np.fill_diagonal(H[2:,:], diag2)
    np.fill_diagonal(H[3:,:], diag3)
    np.fill_diagonal(H[4:,:], diag4)

    return H
```

F.2. CONVERGENCE

Listing F.2: Function for convergence of eigenvalues and eigenvectors

```

def convergence(M, B1, B2, B3, k, xi, deltaN, deltaE):
    '''
    Find the convergence of the eigenvalues and eigenvectors of the given Hamiltonian matrix.
    Inputs:
    M: number of states
    B1: first-order anharmonicity coefficient
    B2: second-order anharmonicity coefficient
    B3: third-order anharmonicity coefficient
    k: unitless parameter in the kinetic term (default 1)
    xi: unitless oscillator length (default 1)
    deltaN: step in the basis dimension
    deltaE: energy convergence threshold
    Outputs:
    eigvals: converged eigenvalues for the given threshold
    eigvecs: converged eigenvectors
    Nfin: total number of the basis dimension after the steps
    '''
    N0 = M # initial basis dimension
    converged = False # this works like a semaphore
    eigvals_prev = np.zeros(M) # stores eigenvalues from previous
                               # diagonalization

    while not converged:
        # diagonalize the Hamiltonian matrix
        eigvals, eigvecs = np.linalg.eigh(hamiltonian_matrix(N0,B1,B2,B3,k,xi))
```

```python

        # check convergence by comparing the first M eigenvalues from previous
        # and current diagonalizations
        diff = np.abs(eigvals[:M] - eigvals_prev)
        max_diff = np.max(diff)

        if max_diff < deltaE:
            converged = True
        else:
            N0 += deltaN
            eigvals_prev = eigvals[:M]
            Nfin = N0

    # return converged eigenvalues and eigenstates
    return eigvals[:M], eigvecs[:, :M], Nfin
```

F.3. WAVE FUNCTIONS

Listing F.3: Function that calculates the Wave Function of the HO

```python

def harmonic_oscillator_wf(x, n):
    """Calculate the nth energy level of the harmonic oscillator using scipy.special Hermite polynomials.
    Input:
    x: position grid where the wavefunction is computed
    n: number of energy states
    Return: Value of phiHO calculated as sqrt(1/(2**n * factorial(n))) * pi**(-1/4) * exp(-x**2/2) * H(x,n)

    """
    return np.sqrt(1/(2**n * np.math.factorial(n))) * np.pi**(-1/4) * np.exp(-x**2/2) * hermite(n)(x)
```

or recursively

Listing F.4: Function that calculates the Wave Function of the HO recursively

```python

def hermite_rec(x, n):
    """Calculate the nth Hermite polynomial for an array of x values using recurrence.
    Input:
    x: position grid where the wavefunction is computed
    n: number of energy states
    Return:
    H(n)(x) = 2*x * H(n-1)(x) - 2*(n-1) * H(n-2)(x)
    """
    if n == 0:
        return 1
    elif n == 1:
        return 2 * x
    else:
        return 2 * x * hermite_rec(x, n-1) - 2 * (n-1) * hermite_rec(x, n-2)




def HO_wf_rec(x, n):
    """Calculate the nth energy level of the harmonic oscillator but the hermite polynomials are calculated
    using recurrence.
    Input:
    x: position grid where the wavefunction is computed
    n: number of energy states
    Return:
    Value of phiHO calculated as sqrt(1/(2**n * factorial(n))) * pi**(-1/4) * exp(-x**2/2) * hermite_rec(x,n)
    """
    return np.sqrt(1/(2**n * np.math.factorial(n))) * np.pi**(-1/4) * np.exp(-x**2/2) * hermite_rec(x,n)
```

Listing F.5: Function that calculates the Wave Function of the Quartic Oscillator

```python

def calculate_psi(n, eigvecs, x):
    """
    Calculate the wave function Psi for the QO using the given eigenvectors and positions.

    Inputs:
    n: number of energy states or number of wave functions to calculate.
    eigvecs: array of eigenvectors (obtained from the convergence function).
    x: position grid where the wavefunction is computed

    Outputs:
    psi: array of wave function values.
    """
    psi_values = []

    for i in range(n):
        psi = np.zeros(len(x))

        for j in range(len(eigvecs[0,:])):
            psi += eigvecs[j][i] * harmonic_oscillator_wf(x, j)

        psi_values.append(psi)

    return psi_values
```